



Virginia Commonwealth University
VCU Scholars Compass

Theses and Dissertations

Graduate School

2024

SUPPORTED METAL NANOPARTICLE SYNTHESIS: PRECURSOR DEPOSITION AND AGGLOMERATION AT SUPPORT SURFACES

Edward H. Chandler Jr.
Virginia Commonwealth University

Follow this and additional works at: <https://scholarscompass.vcu.edu/etd>

 Part of the [Catalysis and Reaction Engineering Commons](#), and the [Thermodynamics Commons](#)

© The Author

Downloaded from

<https://scholarscompass.vcu.edu/etd/7833>

This Dissertation is brought to you for free and open access by the Graduate School at VCU Scholars Compass. It has been accepted for inclusion in Theses and Dissertations by an authorized administrator of VCU Scholars Compass. For more information, please contact libcompass@vcu.edu.

SUPPORTED METAL NANOPARTICLE SYNTHESIS

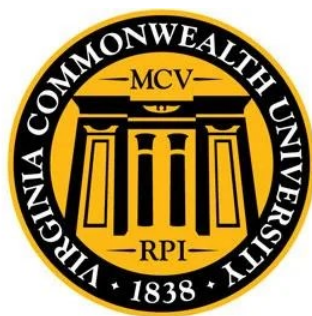
PRECURSOR DEPOSITION AND AGGLOMERATION AT SUPPORT SURFACES

By

Edward Hamer Chandler, Jr.

Bachelor of Arts
University of Richmond, 2016

A Dissertation Submitted in Partial Fulfillment of the Requirements for the Degree of Doctor of Philosophy in
Chemical Engineering at Virginia Commonwealth University



Director: B. Frank Gupton, Ph.D.

Floyd D. Gottwald Jr. Endowed Chair, Department of Chemical and Life Science Engineering

Virginia Commonwealth University

Richmond VA, USA

April 2024

Copyright © by Edward Hamer Chandler, Jr.

2024

Dissertation Committee Members

1. Professor B. Frank Gupton, Ph.D. (VCU CLSE)
2. Professor John R. Regalbuto, Ph.D. (USC CE)
3. Professor Everett Carpenter, Ph.D. (VCU Chem)
4. Professor James K. Ferri, Ph.D. (VCU CLSE)
5. Professor Michael H. Peters, Ph.D. (VCU CLSE)

Dedication

This work is dedicated first and foremost to my wife, Meghan, who through this process has endured much, yet loved much. To my son, Edward III (Teddy), whose recent birth has profoundly reordered my world. This work was envisioned as a steppingstone to the brighter future of my family, long before I had the fortune to meet either of you.

This is also dedicated to my parents, Edward and Victoria, who's full confidence, encouragement, support, and faith have been foundational and transformative.

Acknowledgements

I would first and foremost like to thank my advisor, Dr. Frank Gupton, for his support and guidance over the last 6 years; it has been invaluable. I would also like to thank Dr. John Regalbuto for his generosity in reaching out and mentoring me, teaching me, and even hosting me, a student not even in his University. In general, I would like to thank all of my committee members for their input and suggestions. Also, special thanks to the VCU College of Engineering, Medicines for All Institute, and the Center for Rational Catalyst Synthesis for funding me and providing me with a wealth of resources during my graduate career.

I would like to thank all of my lab mates for their assistance and suggestions in the lab, as well as their friendship out of it. I would especially like to thank Taylor Raine, Maddie Farina, and Simon Friedrich for their immense help and advice across multiple projects.

I would like to express my sincere thanks to my extended family, Carol, Kevin, Krystal, Sam, and Matthew for their sacrifice in hosting and supporting me during this process.

I would like to thank my immediate family, Edward, Victoria, Patrick, Eliot, and Lauren for nearly 30 years of encouragement, support, and non-stop faith through the good times and the bad, never wavering in trust, care, and “willing the good of the other as other.” It is my rock.

Again, I would like to thank my wife and son for enduring this hardship with me, and for coming through to the other side together.

Finally, as a work dedicated to the pursuit of truth, I would like to acknowledge the Pillar and Ground of Truth. In the silent orchestrations of the cosmos and the obscure laws that govern the elements, we find the profound fingerprints of the Divine Intellect, and order arising from what first seemed as chaos. To this Ultimate Reality, the True Object of all knowledge and inquiry, I owe the deepest gratitude.

Contents

DEDICATION	III
CONTENTS.....	V
CHAPTER ONE: INTRODUCTION TO HETEROGENEOUS CATALYST SYNTHESIS AND THE UNDERLYING PHYSICS	2
Part I: An Overview of Heterogeneous Catalyst Synthesis and Impregnation.....	2
Why Catalysis	2
Homogeneous Catalysis	3
Heterogeneous Catalysis	4
Heterogeneous Catalyst Synthesis	6
Impregnation	6
Concluding thoughts.....	11
Part II: Electric Multi-Layer Theory	12
The Theoretical Building Blocks.....	12
The Adsorption of Transition-Metal Complexes onto Surfaces	21
The Form of the Revised Physical Adsorption Model.....	30
Summary of Dissertation.....	38
Addendum.....	38
CHAPTER TWO: THERMODYNAMIC ANALYSIS OF STRONG ELECTROSTATIC ADSORPTION 40	
Background	40
Materials and methods.....	41
Adjustments to the RPA-model	41
An Additional Temperature Dependency	46
Objectives	47
Experimental	48
Results and Discussion.....	50
PZC Determination	50
Uptake Modelling.....	57
Isotherm Modelling.....	64
Synthesis of Pd- and Pt-catalysts at varying temperatures.....	66
Uptake and Isotherm of High PZC Materials	68

Conclusions and Future Work	70
CHAPTER THREE: INVESTIGATION OF PLATINUM AND PALLADIUM DEPOSITION USING STRONG ELECTROSTATIC ADSORPTION VARIABLES.....	72
Background	72
Experimental, Results, and Discussion	73
Conclusions.....	77
CHAPTER FOUR: EVALUATION OF SOLVENT EFFECTS ON PLATINUM DEPOSITION USING SWITCHED SOLVENT METHODOLOGY.....	79
Background	79
Experimental.....	81
Materials	81
Experimental Preparation	84
Procedure of mixing	85
Furnace Reduction	88
XRD Analysis.....	89
Results and Discussion.....	90
Tube Size and Mixing Parameters.....	91
Effect of Drying.....	94
The Effect of Drying Temperature and the Ratio of Acetone to Water	97
Effect of Solvents Other Than Acetone	104
STEM Determined Particle Size	110
Conclusions and recommendations	114
CHAPTER FIVE: CONCLUSIONS	116
REFERENCES.....	118
APPENDIX A: PTFE BOATS AND HOLDER DESIGNS FOR SWITCHED SOLVENT SYNTHESIS (SWISS).....	127
APPENDIX B: DECISION TREE FOR ONE-WAY ANALYSIS OF PARTICLE SIZE FROM STEM SAMPLES.	128
APPENDIX C: STATISTICAL ANALYSIS OF STEM PARTICLE SIZE DISTRIBUTIONS FOR SWITCHED SOLVENT SYNTHESIS	128

Show Distributions for each sample.....	128
Normality Check (Shapiro-wilk or Anderson-Dearing).....	132
Homoscedasticity Check (Levine and Brown-Forsyth)	132
Kruskal-Wallis Test	132

Abstract

Catalysis is a critical component of the chemical manufacturing industry. For example, it has been estimated to be essential to more than 90% of the major industrial processes developed during the middle years of the 20th century.¹ Heterogeneously supported transition metal catalysts in particular have many benefits such as easy separability from the reaction mixture and high thermal stability. One method of synthesizing these is wet impregnation, wherein a metal solution is brought into contact with an oxide- or carbon-based powder. Given optimal environmental conditions, a metal will adhere to the surface through electrostatic means in a process called Strong Electrostatic Adsorption (SEA), which can be described by the Revised Physical Adsorption (RPA) model.

In this work, the RPA model is first extended to accommodate a wide range of temperatures. A study is then conducted to investigate the effects of temperature variations on the adsorption of noble metals to various oxide surfaces, and the results are compared to theory. Then, a similar study is performed to understand the effect of both type and concentration of ions on not only the adsorption of metal, but also the final particle size, post-reductive treatment. Finally, Switched Solvent Synthesis, (SwiSS) a novel method to produce sub-nanometer particles by a two-step impregnation involving an organic solvent, is studied. Each step along the SwiSS synthesis process is tested for its magnitude of impact on final metal particle size, and recommendations regarding procedures in future investigations are made.

Chapter One: Introduction to Heterogeneous Catalyst Synthesis and the Underlying Physics

Part I: An Overview of Heterogeneous Catalyst Synthesis and Impregnation

Why Catalysis

In general, all reactions require energy to proceed, as seen in the red energy diagram in **Figure 1**, where the total energy required is E_a . This can involve the work to physically bring reactants together; to remove other molecules, such as solvents, that may block such a motion; to distort or ionize the electron clouds to allow bonding to occur; and to adjust the geometry of the molecules to facilitate bond reorganization. All materials have at least a quantum of energy, and this is stored in many ways, some of which include translational motion, the average kinetic energy $\langle KE \rangle$ of which manifests for a set of molecules as a temperature, $\langle KE \rangle = \frac{3}{2}k_B T$;² electron motion, where at any given moment there may be a non-uniform charge density across a molecule leading to attractive interactions other molecules; electronic changes, such as electrons shifting their quantum levels; and geometric perturbations, such as molecular rotations, vibrations, and various flexations of bonds. All these continual changes will mean at a given moment a set of reactants have some likelihood of achieving E_a . However, either because the rate at which reactants achieve the necessary energy to react is too slow, or because the benefit of energy input by the operator does not outweigh the cost, it is often the case that a given reaction may not be reasonable to run. It is in these cases that a catalyst will be useful if a suitable one exists.

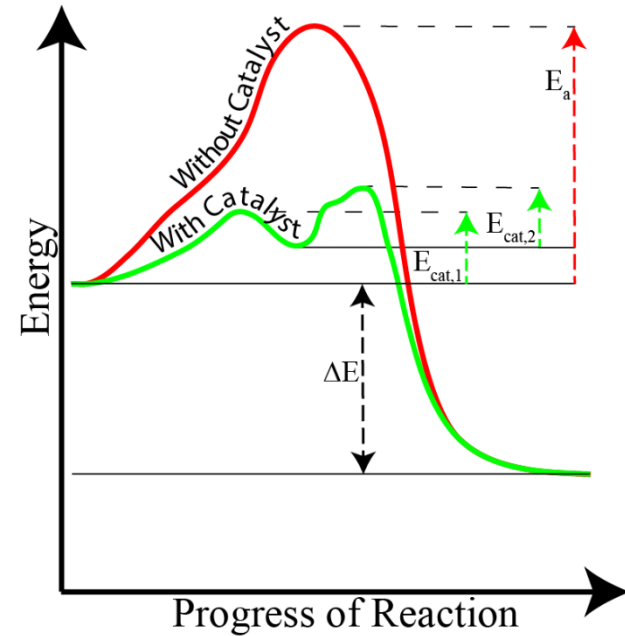


Figure 1. Generic reaction energy diagram. E_a is the typical energy requirement for the reaction, while the sum of $E_{cat,1}$ and $E_{cat,2}$ is the energy required if a suitable catalyst is present.

A catalyst is, in theory, a material that “increases the rate of a reaction without modifying the overall standard Gibbs energy change in the reaction, [a process] called catalysis,”³ the “Gibbs energy change” being represented by ΔE in **Figure 1**. Catalysts do this by modifying the various aspects mentioned above, such as by binding simultaneously to

two reactants and shifting their electron densities, thus bringing them physically close and optimizing their electronics for subsequent bonding. Another catalytic mechanism involves breaking bonds between atoms that are otherwise too stable, allowing subsequent reactions to take place. While these catalytic processes can be complex, they can lower the energy required for the reaction to take place. In **Figure 1**, this can be seen by the catalytic reaction diagram in green, and that the total catalytic activation energy is lower than the activation energy sans the catalyst, $\sum_n E_{cat,n} < E_a$.

Two important aspects of a strict catalyst are that it will not be consumed in the process of a reaction, and that the chemical system looks the same at the end of both the catalyzed and uncatalyzed reaction.³ In practice, these two often are not perfectly achieved, and if they are not mitigated, using the “catalyst” may not yield a net benefit for a process, especially in the context of manufacturing processes.

Homogeneous Catalysis

To see this, it is helpful to use the distinction between homogeneous and heterogeneous catalysis, which are distinguished by their phase relative to the reactants: the former exist in the same phase as the reactants, while the latter exist in a separate phase. An example of the former would be a liquid phase reaction yielding a pharmaceutical, catalyzed by a dissolved palladium catalyst., while an example of the latter would be the removal of sulfur from gas phase petroleum by a solid phase nickel catalyst. By tailoring the chemical makeup and organization of homogeneous catalysts, immensely precise chemical transformations can be attained. However, because of the structural complexity of some of these catalysts, their manufacturing cost can be extremely high, negating the benefit of their use. Homogeneous catalysts, being molecular sized, are usually unfilterable by standard physical means. Low concentrations of impurities such as catalysts in a final product are a common-sense necessity, and standards have even been written into law, such as those recommended for metal concentration in pharmaceuticals by the United States Pharmacopeia for pharmaceuticals.⁴ There are other possible separation processes, for example distillation. However, because of the high

(A)

(B)

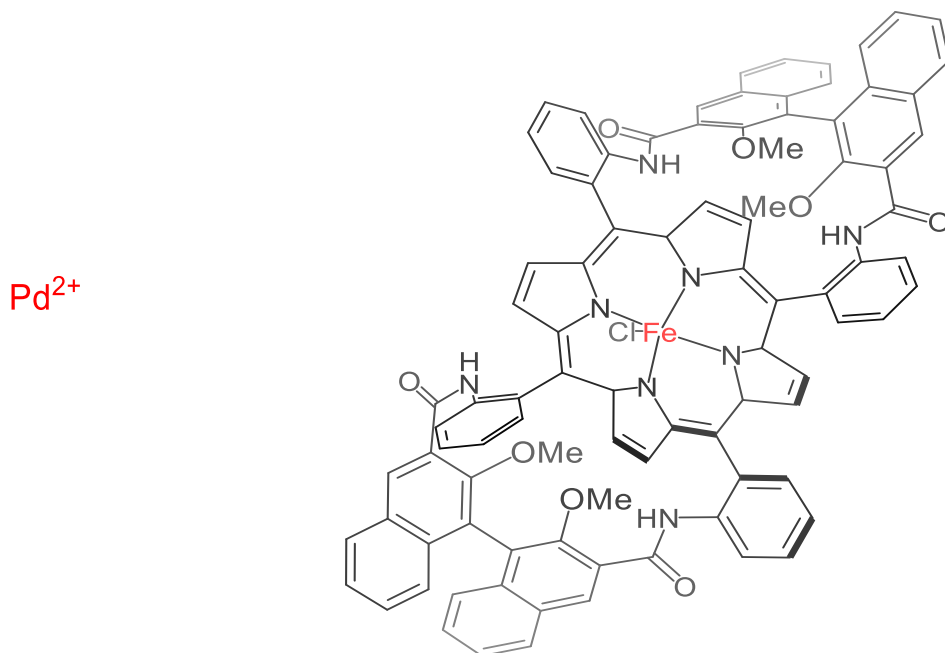


Figure 2. Two examples of homogeneous catalysts, with the metal center shown in red. A) Structurally simple catalyst: palladium cation. B) Structurally complex catalyst: bis-binaphthylporphyrin⁵

molecular weights of some of the products, the temperatures required for distillation can be in excess of the decomposition temperature of the catalyst. Even with processes like extraction or chromatography, the financial, time, and resource costs, as well as potential loss in catalyst, make these catalysts unviable except in select reactions, such as those with volatile products.⁶

Heterogeneous Catalysis

Heterogeneous catalysis is one route to solve the aforementioned problems. Often a solid, heterogeneous catalysis works at the interface between its phase, and that of the reactants. Because of this, the rate of mass transfer of the reactants to the surface of the catalyst becomes critical, and optimizing surface conditions of the catalyst are a critical part of heterogeneous catalysis. While there are numerous types of heterogeneous catalysts, this work will focus

exclusively on oxide- and carbon-supported transition metal heterogeneous catalysts (STMHC). These STMHCs are structured such that the metal is deposited on the surface of a porous oxide or carbon support, often in the form of a powder or pellet, in a way where the metal is bound to the surface. The use of a powder or pellet is of benefit because powders and pellets have a high surface area per unit mass, commonly called specific surface area. This can be achieved if the interior of the powder particle is highly porous, as the surface of the pores will contribute to specific surface area as well as the exterior surface. Figure 3 shows the dramatic difference in the volume of a single powder particle compared to its specific surface area, at correct relative resolutions. For space purposes, the particle here holds a relatively low specific surface area of $25\text{m}^2/\text{g}$. However, many oxides can be in the hundreds, while some carbons can be well over $1000\text{m}^2/\text{g}$.

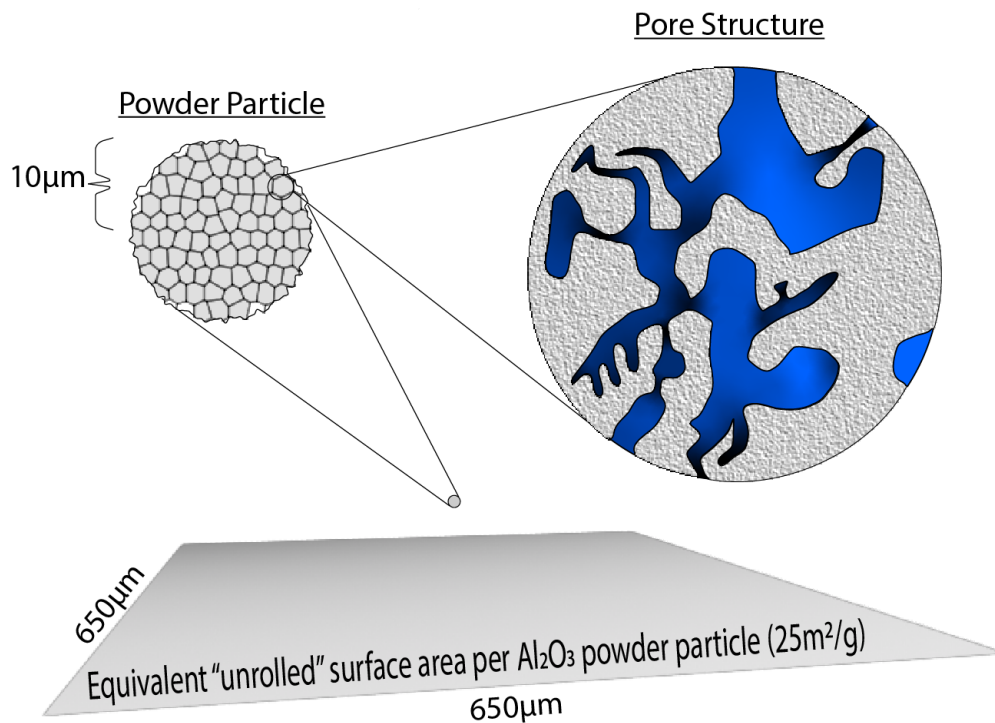


Figure 3. Example of a powder particle that might be used as a support, assuming an alumina density ($4\text{g}/\text{cm}^3$), particle radius of $10\mu\text{m}$, and specific surface area of $25\text{m}^2/\text{g}$. Pores are shown in blue. Note that the un-zoomed particle size is set to the correct relative scale in pixels to the "unrolled" surface area, for visual comparison.

Heterogeneous Catalyst Synthesis

When synthesizing these types of catalysts, two steps are usually necessary. 1) First, the metal must be brought to the surface of the oxide or carbon (commonly called supports) in a way that the metal will stay surface-bound. 2) Then, the metal must be brought into a state that will allow it to perform catalysis. This could involve such further steps as i) the removal of solvent or ligand molecules that are coordinated to the metal, thereby allowing access to the metal by reactants, ii) adjustment of the electronic nature of the metal by adding or removing electrons and bonding to other nearby metal atoms or the surface of the support itself.

Sometimes, these steps can be combined, such as in ball-milling. A ball mill is a simple device where ceramic balls are placed in ceramic containers along with a metal salt and support powder and, once sealed, the container is shaken, forcing instances of two balls colliding with metal and support both between them. Because the collision point is so small with the perfectly shaped balls, the high energy transfer quickly heats up the metal and support to the end that they might bind to each other, though this does not always happen.⁷

Other ways to do this include creating so-called sol-gels through a sequence of hydrolysis, dehydration, and aging solutions of dissolved metals, often in water. This yields metal oxide powders, where the metal is chemically apart of the material, as opposed to being bound to the surface of a separate phase.⁸

Impregnation

Often however, the two steps of bringing the metal to the surface and chemically treating the metal are two separate steps. A simple way to bring the metal to the surface of the support is to dissolve metal in water, often using a metal salt (e.g. PdCl_2); combine the metal solution with the powder; if necessary, separate the excess solution from the wet powder; and dry the now-metal-containing powder. The filling of the pores and interstitial spacing process is called “impregnation” of the support by the metal (and technically the rest of the solution).

Structure of Intragranular Solution

The initial addition step of the impregnation process will lead to a coating or “wetting” of the powder surface by the solution. At high levels of solution, called “surface loading” or “mass loading” of the support into the aqueous phase,

the powder surface is saturated, and the particles might disperse into the solution as a suspension, or collect at the bottom of the container. Impregnations at this level are called “wet impregnations.” Conversely, dry impregnation would refer to impregnations done at liquid levels below the volume required to fill the inter- and intra-granular pore volume, i.e. the space between the particles and in the interior pores, respectively.

At lower surface loadings, however, the powder particles might exhibit a few different states. When there are low liquid levels between particles, the liquid will preferentially collect near where the particles touch in what are called liquid bridges. These liquid bridges have an increased resistance to being stretched, called tensile strength, due to their increased surface tension. Above a certain level of liquid loading, particles will hold multiple liquid bridges, such that particles are held together in agglomerates, but air is still predominant and free to move. This is called a pendular state.^{9, 10} At higher liquid loadings, bridge contact points begin to overlap. This is called the funicular state.¹¹ Higher still, the air is significantly displaced between particles inter-particle spacing is filled. This is called the capillary state.⁹ Finally, a further increase leads to the entire inter-granular volume being filled. This state is called the slurry state.⁹

Pore Imbibition and Structure of Intergranular Solution

The impregnation mixtures are often shaken in order to distribute the solution around the surface of the powder. This will disrupt the liquid bridge structure to an extent that will be determined by a balance between the intensity of shaking and the collective tensile strength of the liquid bridges. As the network is disrupted, freer liquid is allowed to encounter the mouths of the intra-granular pore network within a given particle. This liquid may then be drawn into the interior pore network through a process called imbibition, which arises from a variety of forces. Attractive, capillary forces between the solution and the pore surface may lead to spreading to maximize interfacial area.¹² Often, especially on hydrophilic surfaces, there is a thin film of solution that spreads ahead of the capillary front, driven by disjoining pressure which arises from a collection of intermolecular interactions between the surface and the liquid molecules. For small pores and long imbibition times, the disjoining pressure driven fluid flow in pores dominates over the capillary driven flow, and the remaining flow is comparable to the rate of diffusion, even for large films.¹³

Ahead of even these thin films may be significant water due to humidity levels in the environment as well as hydrolytic reactions of surface functional groups. The pre-adsorbed water layers as well as the near-surface layers of

the disjoining pressure-driven films are strongly affected by the intermolecular interactions with the surface and can take on properties dramatically different from bulk water. One major difference is an increase in both density and viscosity. Adsorbed water layers will strongly hydrogen bond with surface functional groups, forming solid phase-like structures.¹³ Some have drawn comparison between these phases and a continuous ice phase,¹⁴ though others have rejected that description in favor of a strongly ordered surface bound phase, persisting as individual nanodroplets until high humidities, centered on each surface hydroxyl group.¹⁵ Either way, the surface water is significantly less mobile than the bulk phase. The densification of surface water will also increasingly lessen the expected penetration depth of the water with decreasing pore width, as the surface bound phase becomes dominant over the non-surface phase. At 5nm pores, this decrease was by half the expected penetration. Thus, for highly microporous and mesoporous materials (<2nm and between 2 and 50nm, respectively¹⁶), where much of the total surface area can be attributed to the interior pore surface, the interior solution distribution may be very different than expected.¹³

Metal Complex-Support Interactions and Adsorption

During the surface coverage and pore infiltration process, the dissolved metal in the solution may interact with the surface in a number of ways to cause it to bind. One possible surface-metal interaction that may occur is that the functional groups on the surface may directly react with the metal or its ligand structure, such as between Platinum-amines and certain carbon supports.¹⁷ On the other hand, the surface can also polarize the immediately surrounding solution, changing the material properties such as dielectric constant and random molecular orientation and leading to a lower overall solvation power over the near-surface ion. The metal will then experience increasing relative attraction to another phase, in this case the support surface, and deposit out of solution onto the support.¹⁸ Because of their high surface area to volume ratio, this effect can be extreme in pores.

While there are many other adsorption processes, one more will be mentioned here: electrostatic adsorption. As the metal ions in solution are charged, they experience a repulsive force from like-charged particles and surfaces, and an attractive force from oppositely charged of the same. This attraction primarily happens according to the coulombic law, where the attraction between charged particles is inversely proportional to the square of the distance between their centers. Thus, if the surface were to become like-charged to the metal, the metal would repulse from the

solution-water interface. Conversely, if the metal and surface were oppositely charged, they would feel an electrostatic attraction and bind together. This will be discussed extensively in this dissertation.

Drying

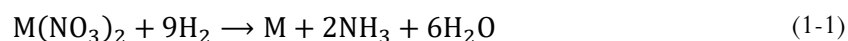
Once the metal containing solution has satisfactorily wet the surface of the support and the metal is bound, the powder is dried, often by vacuum, elevated temperature such as above the normal boiling point of water, or a combination of the two. This drying process involves a reversal of the processes discussed before: The pore water must flow out from the interior to the surface. If there is significant vapor pressure from heat or vacuum, evaporation may actually outpace the movement of the column of water through the pore network, and the water may exit as a gas.¹⁹ As this happens, intergranular water will also evaporate. The strongly adsorbed, solid-like layers of water can take much longer to evaporate and may never truly leave. It was found by Zhuravlev, for example, that amorphous silica still retains a partial monolayer of water until 190°C under vacuum, a temperature that is sure to increase at atmospheric conditions.²⁰ The adsorbed metal will also be a part of this adsorbed system in some way, coordinated to some amount of water after drying.

Pretreatment of the Catalyst – A Focus on H₂-Reduction

Finally, the adsorbed metal will then be treated to adjust its oxidation state. Commonly the metal is needed to be roughly in the M⁰ state, and because there is almost always a net electron deficiency in transition metal complexes, the metal needs to have electrons added to achieve this state and thus be “reduced.” One way this can be done is by exposure of the adsorbed metal complex to molecular hydrogen, H₂ (g), at elevated temperatures, typically in a controlled environment such as a tube furnace.

On a molecular level, the treatment of the metal by hydrogen can proceed in two primary ways: by homolytic or heterolytic cleavage, which tend to occur more for nucleophilic or electrophilic metal centers, respectively. During homolytic cleavage, the hydrogen atoms within H₂ will both attract to the nucleophilic metal center. This intermediate complex is stabilized by back-bonding by the metal to the H₂-σ* orbital. They will then cleanly split, and simultaneously oxidatively add as hydrides (H⁻) to the ligand system of the metal, thus increasing the oxidation state of the metal.²¹

However, when the hydrogen approaches the metal center, because of charge field influences from the partially positive metal center and the partially negative ligand superimposed upon random electron motion around the H₂ molecule, one proton can be partially negative and donate electrons to the electrophilic metal, while the other will be partially positive and associate with the Lewis basic ligand on the primary complex or those around it. Because of the electron deficiency of the metal in this case, the stabilizing force of the back-bonding is largely lost, and the basicity of the ligand becomes critical.²¹ When heterolytic cleavage happens, the protonated ligand will usually leave. For example, for nitrate ligands coordinated to noble metal ions, the reaction proceeds as²²



Metal halides and metal sulfates will proceed in a similar manner, yielding reduced metal and the acid of the ligand.²³

Nucleation and Growth of Nanoparticles

Once a neutral metal atom is formed, there are a few routes that particles could grow. First, it is possible that equation (1-1) can proceed where the heterolytic cleavage of the H₂ bond occurs between a metal center of one complex, and the ligand of another.²¹ Metal atoms that are this close during simultaneous chemical changes could conceivably bind, given the right conditions.

A more classical growth pattern is that proposed by LaMer, where a supersaturated atom in solution will spontaneously nucleate quickly by binding to n-nearby similar atoms to form an n-atom cluster. Further monomeric additions to this cluster will occur slowly by diffusion. Once enough monomers are removed from solution, the supersaturation driven nucleation will stop, and only the diffusion driven reaction persists. While LaMer growth has been studied in the context of many systems, its applicability is questionable for transition metal nucleation and growth.²⁴

Another mechanism is Ostwald Ripening, wherein nanoparticle size and solubility are inversely proportional. Thus, small particles are in an appreciable equilibrium with a dissolved, monomeric state, whereas the large particles are not. Overtime, all atoms are in attached to large particles effectively out of equilibrium with solution.²⁵

Another route for nucleation and growth of particles during reduction is the autocatalytic Finke-Watzky mechanism, wherein two steps exist: a slower H₂-catalyzed reduction step, $A \rightarrow B$, such as equation (1-1), and a faster $A + B \rightarrow 2B$ reaction. Because the second step is faster, the initial conversion to B stops, and all local A will join to already present B . This model has been shown to work well with transition metal particles.^{26, 27}

Particles that have already formed by the above mechanisms may also simply coalesce and form a united particle. This can happen randomly, forming visible defects in the crystal structure. However, in certain cases, the surface energy may be such that oriented attachment may spontaneously occur, where particles will not unite until their crystallographic planes align, and they are incorporated in a pristine structure. This is ideal of course, and a middle ground between perfect oriented attachment and simple random coalescence may also occur.²⁵

Concluding thoughts

The foregoing discussion covered many disparate aspects of impregnation as it relates to heterogeneous catalysis. Catalysis has historically been something of a middle ground between art and science because of its enormous complexity. During the process of investigation into literature, the author had to explore papers from fields as disparate as organic and inorganic chemistry, reaction engineering, experimental and computational fluid mechanics, powder technology, petroleum engineering, geological and environmental engineering, soil science, surface science, pharmaceutical granulation, mechanical and material strength, spectroscopy and more. All of these fields have their own jargon and methods of discussing complex phenomena, and a complete understanding of each field's contribution is a great challenge. While a book length treatment of this would barely suffice, the author hopes that the foregoing discussion and the references included will give the reader a starting point for investigating this complex and rich field of heterogeneous catalyst synthesis.

The first few investigations in this work focus heavily on the physics involved at the solution-support interface during adsorption. Primed with a detailed macroscopic understanding of heterogeneous catalyst synthesis, we now introduce and investigate the microscopic, molecular level and track the development of some of the models used later in this work.

Part II: Electric Multi-Layer Theory

The Theoretical Building Blocks

The following is an accounting of the historical development of the theory of the electric double layer. Not a little of what follows is implicit in many later papers and texts, including definitions, distinctions, and assumptions. While the author certainly does not claim a complete summary of the subject of theories of the double layer (such a treatment would require a book length text at minimum), nor are many derivations given, the author hopes that this *ad fontes* approach will fulfil a few requirements: First, that this gives a clear and concise accounting of each of the prominent theories of the electric double layer and the connecting threads between them. Thus, some of the symbols used in the original texts have been changed. Second, that this provides a fundamental groundwork for further investigation into this literature by the reader. There are many concepts that appear in later publications that are often not entirely explained fully except in literature decades earlier. Thirdly, and as an addendum to the prior reason, that this be a bibliographic resource to the reader, that they might not have to track down many of the basic texts. Finally, and foremost, that the reader may be more than a passive reader and engage as fully as possible with the rest of this work, conceptualizing the systems discussed in granular detail, and even anticipating some of the conclusions presented.

Capacitors and The Helmholtz model

Simple capacitors are constructed as two separate conductive plates with an insulating material, also known as a dielectric. When a current is supplied to one of the conductive plates, electrons accumulate. The resultant charge field will repel electrons on the opposite conductive plate, leading to a positive charge. If, as is usually the case, the capacitor is part of a circuit with a battery, the additional voltage across the circuit will also pull the electrons away from the positive conductive plate, leading to a significantly higher potential difference across the capacitor. If the supplied current is cut off, the stored electrons are then available to do work, such as by temporarily replacing the cut off current.²⁸ In the latter half of the 19th century, Hermann von Helmholtz was studying the effect of charging a pair of platinum electrodes that he had immersed in aqueous solutions. Careful experiments showed that upon charging, a spontaneous layer of positive ions formed on the negatively charged metal surface. While the charging never did reach equilibrium, indicating there was leakage of the current into solution, there was a discharge current measured

after the power supply was cut off. The parallel was clear: The electrode surface and layer of ions were analogous to the parallel plates of a capacitor, with an “insulating layer [of infinitesimally small thickness].”^{29, 30}

One effect of the Helmholtz model is that, since the charges on the two planes are assumed to be equal in magnitude but opposite in polarity,

$$\sigma_0 (\text{metal surface}) = -\sigma_{\text{solution surface}} \quad (1-2)$$

there is a near discontinuity or near infinite slope for the change in charge between the plates. Helmholtz himself measures this to be around 0.4nm.³⁰

The Gouy-Chapman Model

Later, Louis Georges Gouy noticed a discrepancy:

“En effet, les ions sont soumis, en outre des actions électriques qui tendent à les accumuler à la surface, à la diffusion qui tend à rétablir l’homogénéité qui existait avant la charge. Il en résulte un état d’équilibre . . .” [Indeed, the ions are subject, in addition to electrical actions which tend to accumulate them on the surface, to diffusion which tends to restore the homogeneity which existed before the charge. This results in a state of equilibrium. . . .]”³¹

In other words, there are at least two forces in equilibrium: 1) the electrostatic attraction to the charged plate by the oppositely charged aqueous ions, and 2) the diffusion of ions which acts as a restoring force for an even distribution of ions throughout the solution. Both Gouy (1910)³¹ and David Leonard Chapman (1913)³² addressed this issue by assuming a diffuse layer of ions behaving as a “perfect gas” with an elevated concentration at the surface that decays radially from the surface to zero excess at infinity. They formalized this using Poisson-Boltzmann statistics and allowing the solvent to enter the volume. This complexity leads to a new equation for the surface charge, and relates it to the potential difference between the charged electrode surface and the potential of the solution at infinity (Gouy, eq. 13),

$$\varphi_{\infty} - \varphi_0 = \frac{4\pi}{K} \varepsilon \sigma_0 \quad (1-3)$$

¹ Translated with Google Translate (8:32AM, 3/22/204)

where φ_0 is the potential at the surface ($_0$); φ_∞ is the potential approaching infinite distance from the surface ($_\infty$); K is a factor, constant for a given medium, describing the ability of the solution to separate in the presence of an electric field (akin to permittivity); and ε is the radial distance from the surface of the “center of gravity” of the charge, acts as if the entire charge originates from this plane, and is described by the equation,

$$\varepsilon = -\frac{1}{\sigma_0} \frac{KRT}{4\pi m \nu_a} \log|U_{a0}| \quad (1-4)$$

where R is the gas constant, T is the temperature, m is 1 mol, ν_a is the valence of the anion ($_a$), and U_{a0} is a scaling factor that, when multiplied by the molarity of anions ($_a$) in the bulk solution, return the molarity of the anions at the surface ($_0$). At small ion concentrations, Gouy shows how U_{a0} is analytically a function of both solute concentration (C) and σ_0 . Finally, at low to moderate surface charges, the Helmholtz equation (1-2) is replaced by an equation describing what has come to be known as the Gouy-Chapman theory,

$$\sigma_x = \sigma_0 e^{-\frac{x}{a}} \quad (1-5)$$

where x is the radial distance from the surface, and a is a characteristic length for the effect of charge that decreases with concentration and higher ion valences but increases with permittivity and temperature.

The Stern Model

As implied in the preceding paragraph, Gouy-Chapman theory fails to predict U_{a0} at high σ_0 . In 1924, Otto Stern addressed this, asserting that the failure of the Gouy-Chapman model is largely due to the assumption that the ions behave as a perfect gas, an assumption that he goes so far as to say makes “its practical usefulness almost illusory.”³³ He also indicates that the predicted capacitance of the double layer, inversely proportional to the distance between the planes, is far higher than the experimentally determined values, which he shows to be due to the predicted separation

between ϵ and the metal surface being $<1\text{\AA}$.² Obviously this distance is physically impossible, but even approaching this range would displace all of the solvent, necessitating the use of the dielectric constant pertaining to the ions instead of that for water, which would also lower the capacitance.

Stern's solution to the problem is to merge the Gouy-Chapman theory with the earlier theory of Helmholtz. He maintains the charge balance but splits the region of excess cations around the metal electrode into two. Directly adjacent to the electrode of charge σ_0 is a modified Helmholtz layer of ions without intervening solvent molecules of charge σ_1 . The change of charge radially outward is still modelled as linear. However, unlike Helmholtz theory, $\sigma_0 > \sigma_1$. The remainder of the charge is accounted for by the second region, a diffuse layer of cations of charge σ_2 following Boltzmann statistics in the way that Gouy and Chapman conceptualized. Thus, for Stern theory,

$$\sigma_0 = -(\sigma_1 + \sigma_2) \quad (1-6)$$

where σ_1 is driven by electrostatics, while σ_2 is driven by diffusion due to thermal motion. Interestingly Stern states that at the low temperature limit, his theory collapses into Helmholtz theory as thermal motion would cease to exist.³ Equation (1-6) is expanded to its full form:

$$K_0(\varphi_0 - \varphi_1) = FZ \left(\frac{1}{2 + \frac{1}{c} e^{\frac{\Phi_- - F\varphi_1}{RT}}} - \frac{1}{2 + \frac{1}{c} e^{\frac{\Phi_+ + F\varphi_1}{RT}}} \right) + \sqrt{\frac{\epsilon_{r,water} RT}{2\pi}} \frac{c}{18} \left(e^{\frac{F\varphi_1}{2RT}} - e^{-\frac{F\varphi_1}{2RT}} \right) \quad (1-7)$$

² For reference, the range of monocationic radii for the transition metals without hydration sheaths or ligands is between 1.73\AA (Cu^+) and 2.55\AA (Y^+). (34) Rahm, M.; Hoffman, R.; Ashcroft, N. W. Atomic and Ionic Radii of Elements 1-96. *Chemistry—A European Journal* **2016**, 22 (41), 14625-14632. DOI: 10.1002/chem.201602949 (accessed 11/18/2022). From VCU Library.

³ Of course, after the introduction of quantum mechanics, it is known that there still would be a quantum of kinetic energy remaining at 0K.

where the three terms equal σ_0 , σ_1 , and σ_2 , respectively; K_0 is a scaled capacitance of the double layer, such that: $K_0(\varphi_0 - \varphi_1) = \sigma_0 = -(\sigma_1 + \sigma_2)$; F is the faraday constant (the additive charge of a mole of electrons); Z is the number of moles of the ions in solution; c is a scaled mole fraction; Φ_- and Φ_+ are the adsorption potentials of the anions and cations, respectively; R is the gas constant; T is the absolute temperature; and ϵ_r is the dielectric constant of the medium. For the latter, Stern requires the dilute limit, and thus it is assumed that the dielectric constant roughly equals that of water. In addition to the dilute limit, Stern also notes other assumptions such as that only a single monovalent salt is present.

Finally, by appealing to the ζ -potential (φ_ζ), which Stern defines as the potential at the plane separating the immobile layers attached to the surface and the mobile diffuse layers, Stern gives a route to calculating the adsorption potentials for each ion:

$$\Phi_- + \Phi_+ = 2RT \ln |c_m| \quad (1-8)$$

$$\Phi_- - \Phi_+ = 2F \varphi_{1,m} \sim 2F \bar{\varphi}_1 \quad (1-9)$$

where c_m is the concentration where $\varphi_1 = f(c)$ is either at a minimum or a maximum.

A Digression into the Structure of Electrolyte Solutions

Before we continue, it should be noted that while we have been discussing the effect of charge fields in solution in the context of approximately flat surfaces, similar physics applies to charged particles in solution, including the ionic solutes themselves.

Extended Ionic Charge Fields

As with charged surfaces, the Poisson-Boltzmann equation for the spatial distribution of electrostatic potential can provide the basis of a description of the effect of charged particles on their surrounding environment:

$$\frac{d^2\psi}{dx^2} = -\frac{ze\rho}{\epsilon_r\epsilon_0} = -\frac{ze\rho_0}{\epsilon_r\epsilon_0} e^{-\frac{ze\psi}{k_B T}} \quad (1-10)$$

where Z is the valence on the ion; e is the elementary charge; ϵ_r is the reduced dielectric constant of the medium; ϵ_0 is the permittivity of free space; ρ and ρ_0 are the ion number densities at some point x and at $x = \infty$, respectively;

and k_B is the Boltzmann constant. This electrostatic potential extends significantly beyond the boundary of the ion electron cloud, affecting the surrounding molecules. While this function in theory extends *ad infinitum*, the presence of other charged particles and dipolar solvent molecules surrounding a given molecule form an “ionic cloud” which compensates for or “suppresses” that electric potential to where the mean potential at a certain distance is on the order of that of thermal motion, $k_B T$. Formulated by Peter Debye and Erich Hückel in 1923 in their seminal paper on electrolytic solutions, this distance, eponymously called the Debye Length (κ), is formulated as³⁵:

$$\kappa^2 = \frac{e^2}{\epsilon_r \epsilon_0 k_B T} \sum_i z_i^2 n_{i,\text{bulk}} \quad (1-11)$$

where $n_{i,\text{bulk}}$ is the number of ions per unit volume of the bulk solution.

The final terms in the denominator, $n_{i,\text{bulk}} z_i^2$ ($\frac{\text{ions}}{\text{volume}}$), are proportional to another important electrolytic parameter, ionic strength (I), introduced by Gilbert Lewis and Merle Randall in 1921, which takes the form:

$$I = \frac{1}{2} \sum_i^n m_i z_i^2 \quad (1-12)$$

where m_i is the molality of the i^{th} ion, and the $\frac{1}{2}$ arrives from the inclusion of both cations and anions (not from the inclusion of binary salts). The importance of the ionic strength arrives in the context of activity coefficients, which we will define in the next section, and is described by Lewis and Randall, “*In dilute solutions the activity coefficient of a given strong electrolyte is the same in all solutions of the same ionic strength,*” that is that the activity coefficient for completely dissociating salt in aqueous solution of molality $\lim_{n_{oi} \rightarrow 0} m$ is independent of “the number or nature of the ions of which the solution is composed,” and is solely dependent on valence and molality (viz. ionic strength) of the same.

The Activity Coefficient of Ions

As a final digression away from our discussion of the development of the double layer proper, we define the activity coefficient. The activity, a , of a salt can be thought of as the “effective” concentration of the salt in solution and given by the equation

$$a = \gamma m \quad (1-13)$$

where γ is the activity coefficient. For ideal solutions of strong electrolytes in water, the activity is equal to molality, and the activity coefficient is 1, while deviations from ideality will lead to an increase or decrease in γ . These deviations from ideality can be caused by a few things. First, the long-range electrostatic force generated by each ion in solution will exert an attractive force on those ions oppositely charged to it, thus increasing their local concentration above that of the bulk solution. This creates a local distortion in the solution that is homogenous on a macro scale, and the distance to which this distortion will have an effect is the Debye Length. Interestingly, Debye and Hückel suggest that the Debye length will shrink to the mono-molecular scale as γ approaches 1.³⁵

Another set of reasons for the deviation from ideality is due to the effect of a central charge on the surrounding solvent. Because of the charge emanating from the central ion, the surrounding dipolar solvent will orient itself with respect to that ion. This has a multiplicative effect. First, orienting water in this way lowers its dielectric constant. However, this also allows the electrostatic attraction between the central ions and counter ions to be more strongly felt, lowering their mean distance. Henry Frank calls this “ion association,” and any sort of association resulting in restriction of ion mobility should result in a lowering of activity and the activity coefficient. This can be compensated for however by a strongly bound water layer around the central ion that hinders counterion association.³⁶ The effect of hydration on activity and activity coefficient is such that Robin Stokes and Robert Robinson found that for solutions up to at least $I = 4 \frac{mol}{kg_{H_2O}}$, when combining the Debye-Hückel ion-ion interaction treatment with the ion-solvent expansions of Frank and others, an equation based on the effective hydration number of the cation, n , and the distance of closest approach of an unhydrated anion to an hydrated cation is a satisfactory model of the activity coefficient. This can even be reduced to an equation dependent only on n for many 1-1 salts.³⁷

The Grahame Model

In 1947, David Grahame significantly developed Stern's theories.³⁸ While Stern had mentioned the possibility of needing to account for ion hydration, Grahame specifically addressed this. In addition, it had been found that the potential used by Stern for the diffuse had a few faulty assumptions. The equations he questioned were:

- 1) the 1-dimensional Poisson Equation: $\frac{d^2\psi}{dx^2} = -4\pi\rho/\epsilon_r D_0$
- 2) the Boltzmann equation: $n_i = n_{0i} e^{-\frac{W_i}{k_B T}}$
- 3) the work, W_i , required to bring an ion i from $\lim_{x \rightarrow \infty} \psi \approx 0$ to a point in the double layer with potential ψ :

$$W_i = z_i e \psi$$

where D_0 is the permittivity of free space times 4π ; and n_{0i} and n_i are the number concentration of ions in the bulk solution and at the point in the double layer in question, respectively.

Some issues with these equations are that they do not include the work being done to 1) displace polar solvent molecules in the presence of an electric field, 2) compress and distort the hydration sheath of the ions due to increased solute crowding near the interface, and 3) distort or remove the solvent sheath around the metal surface. The first of these sources of error, Grahame states, is small under most electrode conditions, while the second is largely mitigated because near the interface, ion crowding only increases up to the equivalent of moderately concentrated solutions. The third, however, is where Stern's theory breaks down, as neglecting this will necessarily change the position of the ions relative to the surface.

Graham proposes to simplify the possibility of a hydration sheath by dividing Stern's Helmholtz plane in two, called the inner (IHP) and outer (OHP) Helmholtz planes. The former is equal to the radius of the solvent molecules and dehydrated ions, all of which are assumed to be the same size, that are held to the surface either by Van der Waals forces or covalent bonding. The outer Helmholtz plane is at the distance of the inner face of the diffuse double layer and is populated by those ions whose attraction to the electrode surface is dominated by electrostatic or Coulombic forces. Incidentally, this division requires the specification of the location of ζ -potential previously mentioned in the context of stern theory. Here, Grahame places it at the same point as the OHP.

Assuming a salt of z - z valence, the potential varies radially out from the surface past the Outer Helmholtz Plane (OHP) as

$$|\psi| = \frac{4k_B T}{ze} \tanh^{-1} e^{-\kappa x'} \quad (1-14)$$

Where $x' = x - \lim_{x \rightarrow \infty} x$; and κ a modified expression of the Debye Length. For the charge of the diffuse layer, σ^d ,

Grahame gives:

$$\sigma^d = \sigma_+^d + \sigma_-^d = - \left(\frac{\epsilon_r D_0 k_B T n_{0i}}{2\pi} \right) \left(e^{\frac{z\epsilon_r \psi}{2k_B T}} - e^{-\frac{z\epsilon_r \psi}{2k_B T}} \right) \quad (1-15)$$

Finally, for the adsorption of ions to the OHP, Γ_{\pm} , Grahame gives:

$$z_- F \Gamma_- = \sigma_-^i + \sigma_-^d \quad (1-16)$$

where Γ_- is determined experimentally, thus making the determination of σ_-^i a trivial task, while

$$\sigma_+^d = \left(\frac{D_r \epsilon_0 k_B T n_{0i}}{2\pi} \right) \left(e^{-\frac{z\epsilon_r \psi}{2k_B T}} - 1 \right) \quad (1-17)$$

However, when the ion breaks through its own hydration sheath, as well as that of the surface, an additional term is needed to account for the high degree of preference by the surface and ion for each other. This IHP specific adsorption potential, ϕ_{\pm} , will change the work involved to bring the ion to its equilibrium point, and its closer distance will change the total charge of the interior layer from the metal surface out to the OHP. This charge can then be represented as

$$\sigma^i = 2z_- \epsilon_r r n_{0i} e^{-\frac{z\epsilon_r (\psi^i - \phi_-^i)}{k_B T}} \quad (1-18)$$

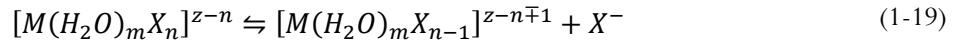
where r is the radius of an adsorbed anion, and cation adsorption is assumed negligible due to their hydration.

As an addendum, Grahame also discusses this theory in the context of non-metallic particles in salt solutions. These surfaces he assumes to be electrostatically neutral, viz. they don't hold a charge, and are thus similar surfaces to the metal electrode surface at its electrocapillary maximum, or point of zero charge. If these surfaces are electrostatically neutral, then the adsorption will be minimal. However, as we will see, this assumption very often does not hold, and spontaneous charging will happen on many particle surfaces leading to significant adsorption.

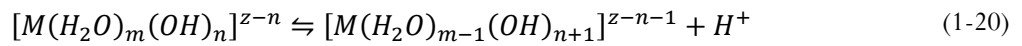
The Adsorption of Transition-Metal Complexes onto Surfaces

The Physical Adsorption Model of James and Healy

Much of the work discussed above used group 1 and 2 metal salts as ion sources because of their relatively simple ligand structure in aqueous solution. However, the situation becomes more complex when considering metals that have moderate and similar equilibrium constants for binding to different numbers of ligands. When an aqueous metal, M^{z+} , readily takes on ligands, L^{-1} , and exists in appreciable equilibrium between multiple states, $[ML_n]^{z-n}$, each of the possible states are called “species” and the state of equilibrium is called “speciation.” Assuming for simplicity the ligand is a monovalent halide X , speciation takes the form



where the proportion of species in solution is dependent on the equilibrium constants for each of the speciation steps. To be sure, all metals will exhibit at least some level of speciation, but this happens especially readily with many transition metal ions. Concurrently with the process in eq. (1-19), some metals spontaneously convert the water in their first hydration sheath into hydroxide and release a proton through a speciation process called hydrolysis. Hydrolysis can happen multiple times, and the various metal species that result



are called hydrolysis products. These hydrolysis products are often not completely soluble in water and simultaneously have an affinity for surfaces. Thus, they are prone to precipitation onto available surfaces.³⁹

Robert James and Thomas Healy published a series of papers that proposed a general model for the adsorption of hydrolysable metal ions onto oxide surfaces. At the time, a common model for this mode of adsorption was that the metal ions would indeed slowly hydrolyze, diffuse near the available surface, and either precipitate or experience adsorption of a specific dehydrated hydrolysis species, such as MOH^+ . On a formal level, this hydrolysis was thought by some to be the mechanism responsible for Grahame’s “chemical” adsorption term, φ^i , see (1-18). As the hydrolysis is an equilibrium reaction with the production of a proton and a hydroxide (viz. an acid and a base), the pH was thought to have a significant effect on ion hydrolysis and thus adsorption.⁴⁰

However, certain inconsistencies were present. For one, adsorption was in fact not dominated by one or another species, such as one of the hydrolysis products. For another, the models that assumed electrostatic adsorption of a specific hydrolysis product found the free energy associated with φ_-^i to be negative. In stark contrast to this theoretical prediction, many systems exhibited adsorption only within a small pH range, indicating that the electrostatic force between a negative surface and a positive ion (or vice versa), which will always be attractive, is counteracted by the chemical adsorption term if Graham's were the complete model. James and Healey assume then that the inhibiting force against uptake must be due to the work required to replace ionic hydration with the solvent sheath around the interface and proceed thusly.

Assuming a monolayer of coverage, they take the final uptake of metal species i to be

$$\Gamma_{tot} = \sum_{i=1}^n \Gamma_i = \sum_{i=1}^n 2r_h C_i e^{-\frac{\Delta G_{ads_i}^0}{RT}} \quad (1-21)$$

where

$$\Delta G_{ads_i}^0 = \Delta G_{coul_i}^0 + \Delta G_{solv_i}^0 + \Delta G_{chem_i}^0 \quad (1-22)$$

r_h is the radius of the hydrated ion; C_i is the concentration of the ion; and $\Delta G_{ads_i}^0$, $\Delta G_{coul_i}^0$, $\Delta G_{solv_i}^0$, and $\Delta G_{chem_i}^0$ are the free energies associated with total adsorption, and its contributions, coulombic adsorption, distortion and changing of the hydration structure, and chemical adsorption. To repeat, the calculation must be performed on each of the metal species, i , in accordance with their respective proportions in solution, per equations (1-19) and (1-20).

The adsorption type, the isotherm, is Langmuirian (e.g. a maximum uptake is a monolayer) with a fractional surface coverage of

$$\theta = \frac{\sum_i K_i M_i}{1 + \sum_i K_i M_i} \quad (1-23)$$

where M_i is the equilibrium bulk phase concentration for each species i ; and

$$K_i = e^{-\frac{\Delta G_{ads_i}^0}{RT}} \quad (1-24)$$

The Electrostatic Contribution to Adsorption

A simple coulombic formulation defines the electrostatic contribution,⁴¹

$$\Delta G_{coul_i}^0 = z_i F \Delta \psi_x \left[\frac{J}{mol} \right] \quad (1-25)$$

where $\Delta \psi_x$ is the change of potential with distance from the surface

$$\Delta \psi_x = \frac{2RT}{zF} \ln \left| \frac{(e^{zF\psi_0/2RT} + 1) + (e^{zF\psi_0/2RT} - 1)e^{-\kappa x}}{(e^{zF\psi_0/2RT} + 1) - (e^{zF\psi_0/2RT} - 1)e^{-\kappa x}} \right| [V] \quad (1-26)$$

where $\psi_0 = \frac{2.3RT}{zF} (pH_{PZC} - pH) [V]$; pH and pH_{PZC} equal the current pH of the bulk solution and the pH of the bulk solution at which the surface has equal molar loading of H^+ and OH^- , or an average electrokinetic potential equal to zero;⁴⁰ and x is equal to the radius of the ion with a primary hydration sheath.

The Solvation Contribution to Adsorption

When considering $\Delta G_{solv_i}^0$, one must understand the initial structure of the surface and the ion hydration. The ions have a single layered hydration sheath which, because of the charge emanating from the ion, has a highly oriented state and a minimal dielectric constant. Because of prior experimental data on water orientation in the secondary hydration layers,⁴² James and Healey assume that while secondary hydration contributes to the free energy change of adsorption, the orientation of secondary water is still on net random, and thus doesn't experience a depreciated dielectric constant.⁴¹ As for the surface, the water is polarized by the charge emanating from the surface, and its orientation is further influenced by repulsion and dispersion forces, though to a lesser degree. The result is a highly oriented layer of water. Because of this orientation, water density on the surface approaches 90% spatial coverage compared to bulk phase water, which is on the order of 70% coverage of an imaginary plane of arbitrary orientation passing through the liquid.⁴² This high degree of orientation also extends farther out from the surface than from the ion, and thus the dielectric constant must be a function of distance. They use a Gouy-Chapman model for the potential derivative, , though they suggest a Stern model for future work:

$$\varepsilon_x = \frac{\varepsilon_{r,bulk} - 6}{1 + (1.2 * 10^{-17}) * (d\psi/dx)_x^2} + 6 \quad (1-27)$$

where $d\psi/dx$ is the Gouy-Chapman model for the potential derivative

$$\frac{d\psi}{dx} = -2\kappa \frac{RT}{zF} \sin(h) \left(\frac{zF\Delta\psi_x}{2RT} \right) \left[\frac{V}{m} \right] \quad (1-28)$$

Because of the minimal dielectric constant of the primary hydration sheath of the ion, it is not disturbed by the adsorption process, and is considered to be part of the adsorbing ion. The free energy change is then due entirely to the removal of the second hydration sheath and replacing it with the hydration sheath sitting on the oxide surface. Rather than attempt to construct a complex continuous model of the dielectric constant that runs through all the parts of the double layer, James and Healy opt for a function for $\Delta G_{solv_i}^0$ that assumes boundary conditions at the interfacial water:

$$\begin{aligned} \Delta G_{solv_i}^0 = & \left(\frac{z_i^2 e^2 N}{16\pi\varepsilon_0} \right) \left(\frac{1}{r_e + 2r_w} - \frac{r_e}{2(r_e + 2r_w)^2} \right) \left(\frac{1}{\varepsilon_x} - \frac{1}{\varepsilon_{r,bulk}} \right) \\ & + \left(\frac{z_i^2 e^2 N}{32\pi\varepsilon_0} \right) \left(\frac{1}{r_e + 2r_w} \right) \left(\frac{1}{\varepsilon_{solid}} - \frac{1}{\varepsilon_x} \right) \end{aligned} \quad (1-29)$$

where r_e is the distance to the center of the ion past the first layer of interfacial water. However, it is assumed that the IHP is the equilibrium distance for the center of the ion with strongly bound primary hydration, and thus r_e is equal to the radius of the dehydrated ion, r_h . As an aside, they assume that the OHP is seen as the distance of the centers of cations with both primary and secondary hydration.⁴¹

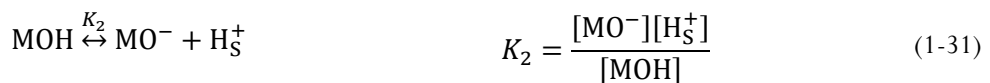
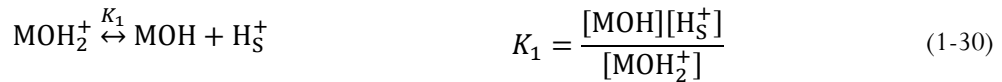
The “Chemical” Contribution to Adsorption

The authors discuss the Grahame “chemical adsorption” contribution with hesitation. While they acknowledge multiple present forces, such as inter-atomic Born repulsive forces, coordinative binding by hydroxyl groups between metal ions and the surface, and hydrogen bonding, they opt to not specify the form of the potential, and instead use prior determined potentials found in earlier works.^{40, 43} Thus, they determine the electrostatic and solvation contributions first, and add in the chemical adsorption potential as essentially a scaling factor at the end.⁴¹

The Revised Physical Adsorption Model

While the James and Healy model had success, it failed in a few areas. For one, it incorrectly predicted that the lower charged cations would preferentially adsorb over highly charged ions, as the high charge would increase the work required to remove the secondary solvation sheath for adsorption to the IHP. ⁴¹ Another issue was the Grahame chemical adsorption term that remained undefined. Later theories called triple layer models (TLMs) attempted to address this term, but these often led to an increase in adjustable parameters in the defining equations and thus a more unwieldy and hard-to-apply theory.

Moreover, James and Healy's work had started with a few incorrect assumptions about the system that were baked into their theory. First, they assumed that the surface of the oxide was amenable to a Nernstian model. This would require that the electrons have full mobility in the electrode, that there is no specific adsorption, and that the surface stay chemically uniform during the progression towards equilibrium. However, oxides are usually far from perfect conductors, the model assumes that there is adsorption at the IHP, and the surface functional groups will protonate and deprotonate to alter the charge of the surface. They may even bind with any counterion. ^{44, 45} For surface protonation, assuming a single metal atom M per surface oxygen the equilibrium will typically follow the form



where H_S^+ is the concentration of surface protons. Two common situations are where an oxide will exhibit one or both of these surface reactions. A common example of simply exhibiting only the behavior in equation (1-30) is $M = \text{Si}$ while both equations (1-30) and (1-31) occur in $M = \text{Al}$. ⁴⁶ The former model of a surface is called a 1-pK model, while the latter is called a 2-pK model.

A First Revision

It is these and a few others that led Krishna Agashe and John Regalbuto to revise the Physical Adsorption model into what they called the "Revised Physical Adsorption" (RPA) Model. ⁴⁶ One adjustment pertains to the coulombic term,

equation (1-25), in the free energy model of the double layer, equation (1-22). the incorporation of the non-Nernstian models of oxide surfaces. Using prior work by Healy and others,⁴⁷ they reintroduce the electroneutrality condition used through-out the double layer literature, (see equations (1-2) and (1-6)),

$$\sigma_0 + \sigma_d = 0 \quad (1-32)$$

where σ_d is the total charge of the double layer, which they assume accords with the original Gouy-Chapman model, and is defined as

$$\sigma_d = -\sqrt{\frac{2N_A \epsilon_r k_B T}{1000\pi}} \sinh\left(\frac{e\psi_d}{2k_B T}\right) \quad (1-33)$$

where N_A is Avagadro's constant, and ψ_d is the electrostatic potential at the OHP. For the surface charge,

$$\text{1-pK model} \quad \sigma_0 = -eN_s \frac{\frac{K_2}{[H^+]} e^{\frac{e\psi_0}{2k_B T}}}{1 + \frac{K_2}{[H^+]} e^{\frac{e\psi_0}{2k_B T}}} \quad (1-34)$$

$$\text{2-pK model} \quad \sigma_0 = -eN_s \frac{\frac{[H^+]}{K_1} e^{\frac{-e\psi_0}{2k_B T}} - \frac{K_2}{[H^+]} e^{\frac{e\psi_0}{2k_B T}}}{1 + \frac{[H^+]}{K_1} e^{\frac{-e\psi_0}{2k_B T}} + \frac{K_2}{[H^+]} e^{\frac{e\psi_0}{2k_B T}}} \quad (1-35)$$

where N_s is the number of surface oxygen groups capable of performing the transformations in equations (1-30) and (1-31), while K_1 and K_2 are the equilibrium constants from the same; $[H^+]$ is the free proton (or hydronium^{48,49}) concentration found in the bulk solution; and the surface potential ψ_0 is given by

$$\psi_0 = \frac{2.303RT}{ZF} [pH_{PZC} - pH] \quad (1-36)$$

where 2.303 is a change of base to convert from base-10 logarithm to the natural logarithm, $2.303 \approx \frac{\log_{10}|10|}{\log_{10}|e|}$,

pH_{PZC} is called the Point of Zero Charge, and is the pH value in the bulk solution that, when achieved, will protonate the surface such that it is uncharged, and thus no-double layer is present;⁵⁰ and pH is the $-\log|[H^+]|$.

The n-pK models are so named to describe the number of reactions present from equations (1-30) and (1-31), where

n is the number of reactions and $p\chi$ is the standard abbreviation $-\log|\chi|$. To be sure, the 1-pK model is simply a special case of the 2-pK model where $pK_1 = 0$, and beyond the study in question, the 2-pK model is used ubiquitously. Finally, the form of the free energy of adsorption due to coulombic forces remains the same as in equation (1-25), and the associated equations.

A second adjustment to James and Healy's original model involves the recognition of discreet ion effects. Recalling the discussion above on activity coefficients, the volume around a charged surface is permeated by not only the electrostatic surface potential, but also a coulombic and Van der Waals forces from the ion as well. In addition, when adsorbed the ionic cloud will interact with the surface electrostatic field as well as other laterally placed ions, if the adsorption is high enough. This complex network of interactions leads to a very different ionic environment for the compact region interior to the OHP compared to the Gouy-Chapman diffuse layer. Some of these effects include non-spherical hydration sheaths, altered dielectric constants, and elevated densities.⁵¹

In order to account for these discreet ion effects, the solvation energy term was adjusted using a geometry that assumes a single plane of adsorption⁵² rather than a split between the IHP and the OHP

$$\Delta G_{solv,i} = \frac{1}{2} z_i e \Phi_i + \frac{(z_i e)^2}{8\pi \epsilon_0 \chi_i} \left(\frac{1}{\epsilon_x} - \frac{1}{\epsilon} \right) \quad (1-37)$$

where the potential, Φ_i , is taken to exist at a distance from the surface equal to the radius of the ion with a single, primary hydration sheath and takes the form

$$\Phi_i = \frac{z_i e}{8\pi \epsilon_x \epsilon_0 \chi_i} \left[\frac{f_1 + f_2}{\sqrt{f_1 f_2}} \tan^{-1} \left(\sqrt{|f_1 f_2|} \right) - \ln(1 + |f_1 f_2|) \right] \quad (1-38)$$

$$f_1 = \frac{\epsilon_x - \epsilon_{ox}}{\epsilon_x + \epsilon_{ox}} \quad f_2 = \frac{\epsilon_x - \epsilon}{\epsilon_x + \epsilon}$$

where χ_i is evaluated for the ion with a primary hydration at $r_{ion} + 2r_{water}$; and χ in the dielectric constant evaluation is r_{water} . One consequence of this theory that will culminate in the next section and provide the basis for 0 and Chapter Three: is that this lowers the James and Healey solvation term, equation (1-29), by about half, which leads to the dominance of the coulombic term.

The difference between initial, C_{i0} , and final, C_i , equilibrium bulk phase metal concentration for a given species i is given as

$$C_{i,ads} = \frac{m_s SSA}{V} \left(\frac{\Gamma_{mi} K_i C_i}{1 + \sum_i K_i C_i} \right) \quad (1-39)$$

where m_s is the mass of support; SSA is the specific surface area (area per unit mass) of the support, determined through methods such as BET analysis of physisorption data; V is the volume of the metal-containing-solution mixed with the surface; Γ_{mi} is the theoretical maximum uptake, which is assumed to be a monolayer and is approximated using the hexagonal close packing fraction of circles, 90.7%,⁵³ of radius equal to the hydrated ion. In order to minimize the use of the ill-defined chemical adsorption term, Agashe and Regalbuto fit experimental uptake curves by setting the chemical adsorption energy to zero, and if the fit was poor, $\Delta G_{solv,i}$ was then reintroduced. With the above revisions, however, it was found that, because of the low value of the solvation term, the need for the chemical adsorption term was often lessened, and altogether non-existent for some systems. Again, these adjustments, along with the retention of only primary hydration, lead to an adsorption to the IHP as defined by James and Healy⁴¹ that is predominantly electrostatic in nature.⁵⁴

A Second Revision

Many explanations had arisen about the nature of the chemical adsorption term in the James and Healy model. In an important work by Regalbuto et. al.,⁵⁵ it was found that many of these explanations did not apply, at least during the adsorption of platinum onto aluminas. These invalidated explanations included competitive adsorption between platinum and the counterion, such as chlorine and possible coordination and redeposition between platinum and dissolved support. In fact, various aluminas were used, and all could be modeled by the same parameters. Because the solubility varied between the various supports, this indicated that some intrinsic property of alumina was causing adsorption, such as the surface charging parameters and acidity constants.

The conclusion to be had from the foregoing research is that there are systems where the chemical adsorption term is not needed. In fact, in systems such as those using noble metals, it was found by Regalbuto that for an RPA-model with a value of zero assigned to the chemical adsorption term, the inclusion of the solvation term often yielded

drastically underestimated uptake results when compared to experimental results: in other words, the coulombic term alone correctly explained the data.⁵⁴

This exclusion fits well with data from Park et. al., who confirmed that $(NH_3)_4Pt^{2+}$ complexes adsorb to quartz (100)-water interfaces at least twice the distance of water⁵⁶, indicating that little work was being done to displace the surface or ionic hydration sheath. A similar effect was found by Noble et al. with adsorption of $Au(C_2H_8N_2)_2$ onto carbon and silica.⁵⁷ However, dried yet otherwise untreated $PtCl_6^{-2}$ complexes adsorbed onto alumina are shown by EXAFS to be on the surface with a single hydration sheath simplicity adsorption.^{58, 59} James and Healy themselves had assumed as a fundamental system state for their model that the primary hydration sheaths would be retained.⁴⁰ This holds not only for certain noble metal-support systems, but for some base metal-support systems as well, such as $(NH_3)_6Co^{3+}$ adsorption onto silica.⁶⁰ Because of the complex-to-complex and support-to-support variation in the number of hydration sheaths retained, in practice between 1 and 2 are tested when fitting the RPA-model to experimental data.

The dispensing of the solvation term in the fully revised model may still be valid for adsorption of ions with only primary hydration as the updated solvation calculation in the previous section led to a significant decrease in its value compared to the coulombic term. However, one wonders whether the Grahame model holds substantially more than conceptual power at this point. Grahame conceptualized the OHP as housing all of the coulombically adsorbed ions that retain their primary hydration sheaths, while the IHP was reserved for chemically bound ions or those that broke through the solvation sheath, a qualitatively different type of surface interaction.³⁸ With the allowance for 2 or more hydration sheaths to be retained in the presence of predominantly coulombic forces, the original distinction between the IHP and the OHP somewhat lose their meaning in the context of a pure, reduced RPA-model, leaving a simple, slightly “smeared” adsorption layer.

In addition, by calculating a quantitative test of the accuracy of Stern’s model of the diffuse layer, one finds that the half-thickness of a double layer of a 1M 1-1 salt solution rests closer to the electrode surface than the radius of the adsorbed ions, a [...missing information...]. Another issue rests in the fact that in electric fields, dipoles such as water

will polarize, and thus the dielectric constant of the medium may change. However, this concern comes from a similar issue that the entire method of Grahame rests on the notion that the system behaves as a continuum, which may not happen at high surface charges anyway.

The Form of the Revised Physical Adsorption Model

The final form of the Revised Physical Adsorption (RPA) model has two sets of solvable equations. In general, a Gouy-Chapman model is assumed for the ion distribution near the surface. As stated in the previous section, the Helmholtz plane of adsorption is distant enough from the surface to assume minimal distortion of the surface or ion hydration, allowing the neglect of both the Grahame chemical adsorption term and the James and Healy solvation term. Thus, all that remains is the coulombic attraction between surface and hydrated ion. Finally, a Langmuir type isotherm, or a maximum of one layer of hydrated ions with n_h hydration sheaths, is assumed. The general model for a single class of adsorbing ion is as follows⁶¹:

RPA Langmuir Isotherm	$\Gamma_{Lang}\left(\frac{mol}{area}\right) = \Gamma_{max} \frac{K_L C_f}{1 + K_L C_f}$	(1-40)
-----------------------	---	--------

Double Layer Adsorption Equations

Maximum Possible Adsorption Density	$\Gamma_{max} = \Gamma_{monolayer} = \left[\frac{1}{N_A \pi x^2} \right]$	(1-41)
-------------------------------------	--	--------

Langmuir Equilibrium Constant	$K_L = e^{\frac{-\Delta G_{ads}}{RT}}$	(1-42)
-------------------------------	--	--------

RPA Coulombic Adsorption Assumption	$\Delta G_{ads} = \Delta G_{coulombic} = zF\psi_{x=r_{hydrated\ ion}}$	(1-43)
-------------------------------------	--	--------

Gouy-Chapman Potential Function	$\psi_x = \left[\frac{2RT}{ZF} \right] \ln \left \frac{(Y + 1) + (Y - 1)e^{-\kappa x}}{(Y + 1) - (Y - 1)e^{-\kappa x}} \right $	(1-44)
---------------------------------	---	--------

Equilibrium Bulk Phase Metal Concentration $C_f = C_0 - C_{ads} = C_0 - SL \cdot \Gamma_{max} \left(\frac{K_L C_f}{1 + K_L C_f} \right)$ (1-45)

Ancillary Equations:

Boltzmann Factor for the Surface Potential $Y = e^{\frac{zF\psi_0}{2RT}}$ (1-46)

Approximate Debye Length $\kappa = 3.31 \cdot 10^9 \sqrt{I}$ (1-47)

Ionic strength $I = 0.5 \sum_i z_i^2 C_{i,f}$ (1-48)

Assumed (i) Radius and (ii) Distance of
Closest Approach to Surface of Hydrated Ion $x = r_{ion} + 2n_h r_{H_2O}$ (1-49)

Most of the above variables are immediately known upon taking account of system conditions such as temperature and composition or calculated from the same. However, two remain, the number of hydration sheaths to retain on the metal ion, n_h , and the charge at the adsorption surface, ψ_0 , which the model assumes is at the distant equivalent to the radius of the hydrated ion, per Equation (1-49). n_h is usually found by computing the model at both 1 and 2 hydration sheaths. However, ψ_0 must be calculated.

Because of the relationship between the electric potential and the ion concentration at the surface and the bulk phase is assumed to follow a Boltzmann distribution, the two regimes can be explicitly described. The involves 4 simultaneous non-linear equations describing the intersection of solution chemistry and electrostatics at the support surface, adopting an explicitly Gouy-Chapman model of the double layer, and assuming a non-Nernstian surface with a 2-pK model.

Surface Charge-Acidity Relation $\sigma_0 = -FN_s \frac{\frac{[H_s^+]}{K_1} - \frac{K_2}{[H_s^+]}}{1 + \frac{[H_s^+]}{K_1} + \frac{K_2}{[H_s^+]}}$ (1-50)

Surface Charge-Potential Relation (Gouy-Chapman)	$\sigma_0 = -\sigma_d = \sqrt{8\varepsilon_r\varepsilon_0RTI} \cdot 10^3 \sinh\left(\frac{e\psi_0}{2k_B T}\right)$	(1-51)
Bulk Phase Proton Mass Balance	$\sigma_0 = \frac{F}{SL} \left[\{10^{pH_0} - 10^{-(14-pH_0)}\} + \{10^{-(14-pH_f)} - 10^{pH_f}\} \right] \frac{c^0 = 1 \frac{mol}{L}}{\gamma}$	(1-52)
CO ₂ fugacity - Liquid-Vapor Equilibrium	$f_{vap,CO_2} = x_{CO_2} P_{sat} \gamma$	(1-53)

with the ancillary equations

Surface Loading	$SL \left(\frac{m^2}{L}\right) = \frac{\text{Specific Surface Area} \cdot \text{Support Mass}}{\text{Solution Volume}}$	(1-54)
$K_1 = \frac{[SOH][H_s^+]}{[SOH_2^+]}$	$K_1 = 10^{-PZC+0.5\Delta pK}$	(1-55)
$K_2 = \frac{[SO^-][H_s^+]}{[SOH]}$	$K_1 = 10^{-PZC-0.5\Delta pK}$	(1-56)
Bulk Phase-Surface Proton Boltzmann Relation	$[H_s^+] = [H^+] e^{-\frac{e\psi_0}{2k_B T}}$	(1-57)
Activity Coefficient – Extended Debye-Hückel	$\gamma = 10^{-0.510 \frac{\sqrt{I}}{1+\sqrt{I}}}$	(1-58)
Ionic Strength (molal)	$I = \frac{1}{2} \sum_i z_i^2 m_i$	(1-59)
Convenient Ionic Strength Approximation	$I = \frac{1}{2} (10^{-pH_0} + 10^{pH_0-14} + 10^{-pH_f} + 10^{pH_f-14} + C_{CO_2})$	(1-60)
CO ₂ Ionic strength contribution	$C_{CO_2(aq)} = \sqrt{0.01 x_{CO_2} C_{CO_2(g)} K_{H_2CO_3}}$	(1-61)

where n_0 is the number of the pH_0 terms in the ionic strength approximation refer to the counterions of the acid or base used to adjust the pH, assuming a 1-1 acid or base, while the pH_f terms refer to the actual equilibrium proton and hydroxide concentrations. $C_{CO_2(g)} \left(\frac{mol}{L}\right)$ is the concentration of CO_2 in air, x_{CO_2} is the fraction of $C_{CO_2(g)}$ that dissolves into the metal solution, 0.01 is an estimate of $\frac{[H_2CO_3(aq)]}{[CO_2(aq)]}$, while $K_{H_2CO_3}$ is the equilibrium constant of the carbonate formation reaction $H_2CO_3 \rightarrow HCO_3^- + H^+$, and the square root performs the following:

$$\sqrt{[HCO_3^-][H^+]} = [HCO_3^-]. \text{ Bicarbonate formation is thus assumed to be minimal. Finally, } \Delta pK = pK_1 - pK_2 = \log \left| \frac{[SO^-][SOH_2^+]}{[SOH]^2} \right|, \text{ comparing the number of charged sites to uncharged sites at the surface.}$$

There are a couple of use cases for the RPA-model. First, the intrinsic support surface properties, PZC , ΔpK , N_s , must be determined. These can be determined by applying RPA-model to experimental data computationally, through experimental methods, or a combination of the two. Experimentally, N_s can be determined from spectroscopy and ΔpK from mass or potentiometric titration.⁵⁰ The PZC can be found from the plateau of the pH-shift curve of an experiment involving the titration of a series of solutions at different pHs by the support at high surface loadings (e.g. $50,000 \text{ m}^2/L$), as shown in Figure 4. However, because of product-to-product and batch-to-batch variation across samples, in practice it can be helpful to calculate some of these parameters using the RPA-model.

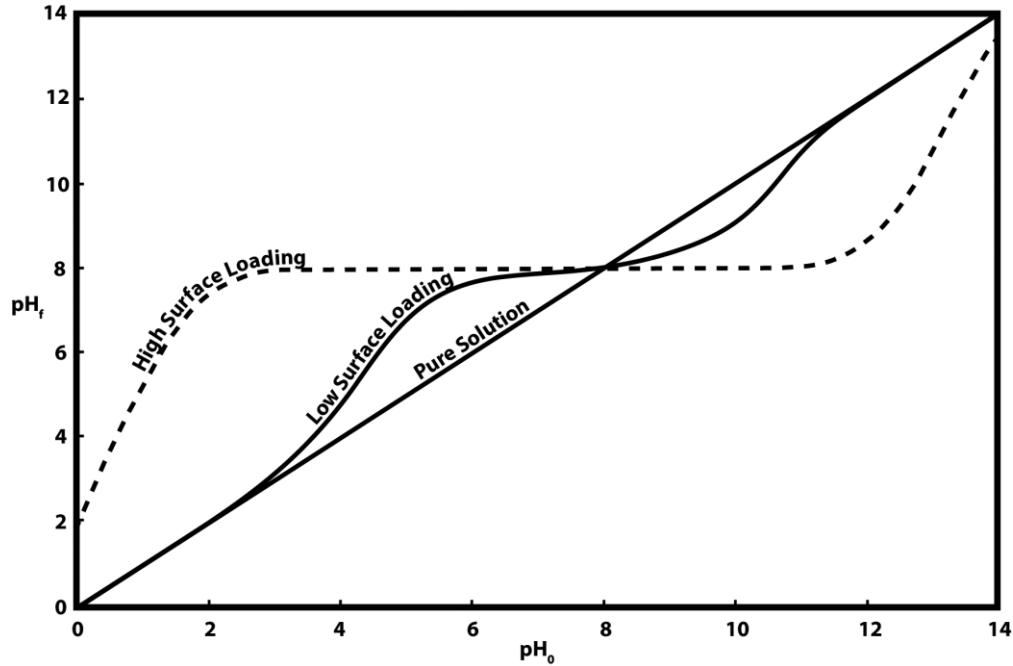


Figure 4. Hypothetical pH-shift curves at high loading and low loading of support surface. Inspired by Park, et al.⁵⁰

When calculating the RPA-model for determination of support properties, the four surface charging equations (1-50) - (1-53) will typically be fit against an experimental pH-shift dataset using a Newton-Raphson algorithm by adjusting σ_0 , ψ_0 , pH_f , and x_{CO_2} for a given set of PZC , ΔpK , N_s values. The three surface parameters will be adjusted until their change from one iteration to the next is negligible. While any of the three surface parameters can be restricted to literature or experimental values, in practice either 1) all three are optimized, or 2) N_s is taken from literature, the PZC is taken from the plateau of the pH-shift curve, and only the ΔpK is kept as an adjustable parameter.^{50, 62} Two adjustable parameter fits, assuming a literature value for N_s , tend to lead to unstable minimizations and poor fits.⁴

Once the surface constants are determined, metal adsorption experiments can be conducted and modeled. The general procedure of fitting is similar. However, in this case, the equivalent concentration of adsorbed metal becomes the parameter that is held constant during each step in the optimization. This term will impact the ionic strength, and thus much of the surface charging phenomena. This will lead to a guess of C_f using equation (1-40). If this value is

⁴ Private communication with John R. Regalbuto

different than the guessed, then the loop will begin again, starting with this calculated value, and continue to loop until the trial value and calculated values are equivalent.⁶² The final model for various ions will look similar to that in

Figure 5.

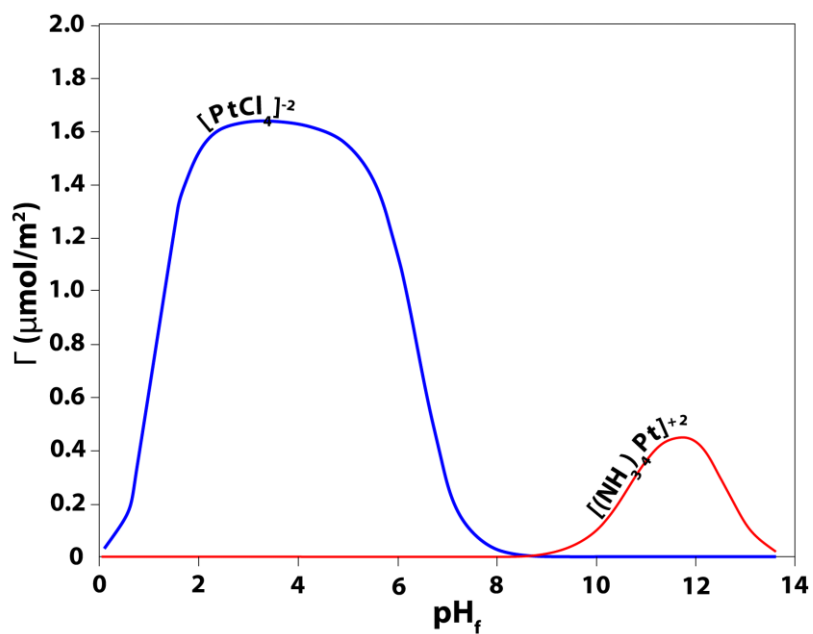


Figure 5. RPA-predicted uptake curves for representative metal ions. Ions like $[\text{PtCl}_4]^{2-}$ retain fewer hydration sheaths than $[(\text{NH}_3)_4\text{Pt}]^{2+}$, leading to the dramatic difference in maximum uptake between different complexes of the same metal. Inspired by Hao, et al.¹⁷

Finally, a summary is given of the literature explicitly using the second revision of the RPA-model in Table 1.

Table 1. Summary of the literature that has been published regarding the 2nd revision of the Revised Physical Adsorption Model

Year	Metal	Salt (ion if not specified)	Support	Notes	Refs.
2003	Pt, Co	H_2PtCl_6	Al_2O_3 (α , γ , η , θ)		41, 54
		$[(NH_3)_4Pt]^{+2}$	Al_2O_3 (γ) SiO_2 (α)		
		Co^{+2}	SiO_2 (α)		
2004	Pt	H_2PtCl_6	Al_2O_3 (γ) SiO_2 (α) Activated Carbon Carbon Black	PZC altered and unaltered	63
		$[(NH_3)_4Pt]^{+2}$	Al_2O_3 (γ) SiO_2 (α) Activated Carbon Graphite		
2004	Pt	$[(NH_3)_4Pt]^{+2}$	SiO_2 (α)	Multiple silicas	61
2005	Pt, Cu	$[(NH_3)_4M]^{+2}$	SiO_2 (α)	Regions of ion-exchange present in H-ZSM5	64
			H-ZSM5		
2008	Pd, Cu, Co, Ru, Ni	$[(NH_3)_{4/6}M]^{+2/3}$	SiO_2 (α)		65
2010	Pt	H_2PtCl_6	Al_2O_3 (γ)		66

		$[(\text{NH}_3)_4\text{Pt}]^{+2}$	$\text{SiO}_2 (\alpha)$		
2013	Pt	Na_2PtCl_6 $[(\text{NH}_3)_4\text{Pt}]\text{Cl}_2$	$\text{Al}_2\text{O}_3 (\gamma)$ $\text{SiO}_2 (\alpha)$ Activated Charcoal	Incipient Wetness Conditions	67
2013	Pt	PtCl_6^{2-} $[(\text{NH}_3)_4\text{Pt}]^{+2}$	$\text{Al}_2\text{O}_3 (\gamma)$ $\text{SiO}_2 (\alpha)$ $\text{Al}_2\text{O}_3 (\gamma)$ $\text{SiO}_2 (\alpha)$		68
2015	Pt	H_2PtCl_6 $[(\text{NH}_3)_4\text{Pt}]^{+2}$	$\text{Al}_2\text{O}_3 (\gamma)$ TiO_2 $\text{SiO}_2 (\alpha)$	High Surface Loading	
2015	Ni	$\text{Ni}(\text{NO}_3)_2$	$\text{Al}_2\text{O}_3 (\gamma)$	Some non-electrostatic adsorption	69
2021	Au	$[\text{Au}(\text{en})_2]^{+2}$	$\text{SiO}_2 (\alpha)$ $\text{Al}_2\text{O}_3 (\gamma)$ TiO_2 ZrO_2 CeO_2 Nb_2O_5 Graphitic carbon Carbon Black	Some non-electrostatic adsorption	57

			Activated Carbon		
2022	Rh	RhCl ₃	Al ₂ O ₃ (γ) CeO ₂	Attribute lack of agreement to inhomogenous surface	70

Summary of Dissertation

This work will be devoted to the mechanisms underlying catalyst synthesis. Chapter One: gave a lengthy introduction to the basic concepts underlying heterogeneous catalyst synthesis, especially with regards to the electric double layer, Revised Physical Adsorption (RPA) model, and Strong Electrostatic Adsorption (SEA). 0 details an investigation into the thermodynamics of SEA, and how truly they manifest with regards to SEA at various temperatures. Multiple systems are studied, some of which have not been investigated yet with regard to SEA, and some of which are fundamentally incompatible with SEA. Chapter Three: continues the investigation into the lesser studied parameters involved in SEA by changing the ionic strength of the solution to decrease binding and increase final metal particle size. Chapter Four: shifts gears and demonstrates the dramatic effect on particle size of adding an organic solvent to an impregnating solution, rather than controlling the pH. is a shift in perspective of catalyst synthesis, viewing catalysis (and chemistry in general) as an *a posteriori* function of the elemental property space. The nature of the “periodic law” is called into question on both practical and theoretical grounds, and a comprehensive database and corresponding Principal Component Analysis model is developed, and some potential applications are shown. It is hoped that this will aide in experimentation when there is no theoretical or intuitional recourse available. Finally, Chapter Five: summarizes the conclusions of the dissertation and suggests future work.

Addendum

In order to assist the reader, a process map will be used at the outset of each chapter. It represents an extremely simplified view of the beginnings of the catalyst synthesis process and will hopefully help the reader understand quickly the focus of each chapter.

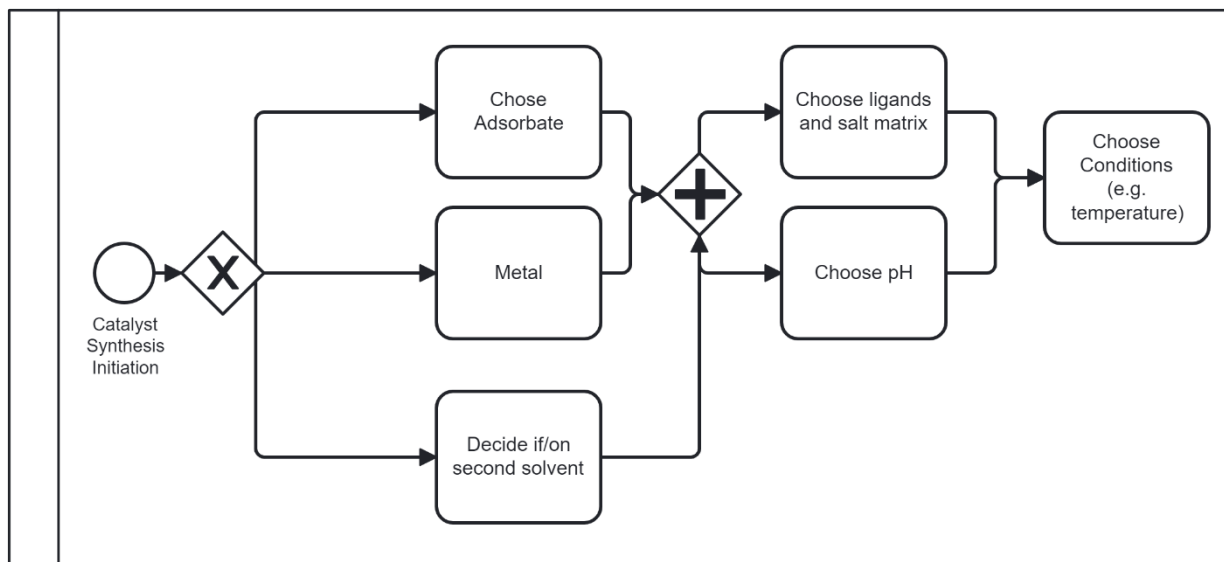
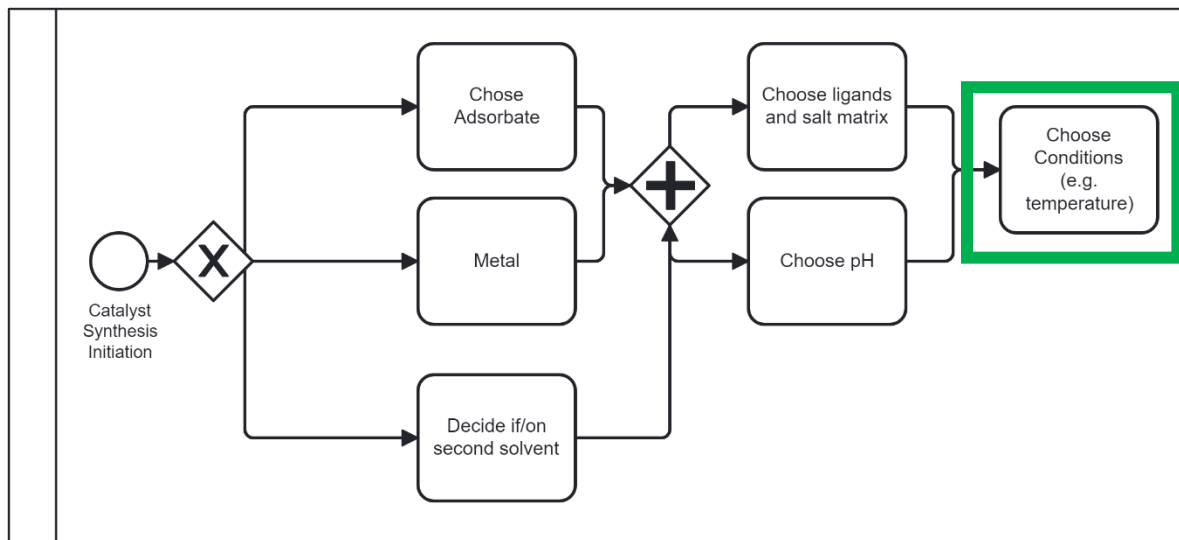


Figure 6. Process map of beginning of catalyst synthesis

Chapter Two: Thermodynamic Analysis of Strong Electrostatic Adsorption



Background

The Revised Physical Adsorption (RPA) model has enjoyed great success for a wide range of metal-support combinations, and Strong Electrostatic Adsorption (SEA) has been demonstrated to be dominant or even exclusive in many more.^{17, 60, 71-81} However, aside from the materials used (metal salt and support), the model has comfortably been used to predict uptake and the other system conditions solely as a strong isothermal function of pH. However, less attention has been given to other system parameters, such as temperature.

Temperature has been widely studied in the context of adsorption. Srivastava et. al. tested the adsorption of tungsten by mixed hydrated oxide cake of iron and manganese at different temperature and reported an increase in adsorption up to 50°C. Thermodynamic analysis to confirm the spontaneity of adsorption and physisorption was also done.⁸²

Adsorption of methylene blue dye in aqueous solutions by rectorite showed gradual increase with increasing temperature between 288K to 308K.⁸³ It has been shown, especially in water treatment literature, that in addition to bulk solution pH, temperature can have a profound effect on some adsorption systems. This has been done using isotherm equations fitted to adsorption data at different temperatures and bulk solution metal concentrations.⁸³⁻⁸⁵

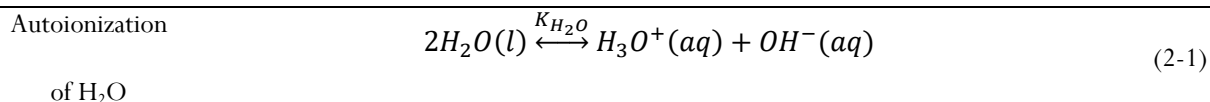
While many of the studies on the effect of temperature on uptake show an often strong, nonlinear effect, there is often little comparison to theory. The RPA-model is a thermodynamic model, and as such, is dependent upon temperature. This can be seen throughout the governing and ancillary equations (1-40) - (1-61), primarily in the pervasive use of the Boltzmann factor. However, there are other implicit places where the temperature could play a roll.

This chapter will focus on teasing out the effect of temperature on adsorption of systems that show predominantly electrostatic attraction, commensurate with the RPA-model predictions. This was done by 1) altering the RPA model by substituting terms to more fully account for temperature, 2) performing a standard SEA series of experiments at constant metal concentration while varying pH_0 , including PZC determination and uptake experiments, and 3) performing uptake experiments at constant pH but different metal concentrations. Steps 2) and 3) were then modeled with the RPA model, and the RPA modelling of step 3) was compared with a least squares direct fit of the Langmuir isotherm equation to the data (see equations (1-40) and (2-18)). The PZC is also analyzed from a thermodynamic point of view.

Materials and methods

Adjustments to the RPA-model

Before any experiments could be modeled, the RPA-model needed to be adjusted to fully vary with temperature. A natural place to start with this endeavor is by adjusting the functions for the properties of water. To do this, the formulations by the International Association for the Properties of Water and Steam (IAPWS) were used for their robustness and generally accepted high level of accuracy.^{86, 87} First, the calculation of the pH and pOH implicitly assumes that the pK_w for the auto-ionization of water is equal to 14.



However, pK_w is a function of temperature. The IAPWS shows that can be calculated as an adjustment to the ideal gas approximation for water⁸⁸:

H ₂ O ionization constant – Ideal Gas ⁸⁸	$pK_{H_2O}^{IG} = \sum_{i=0}^3 \gamma_i T^{-i} \quad (2-2)$
H ₂ O ionization constant – Real Fluid ⁸⁸	$pK_{H_2O} = -2n \left[\log_{10} 1 + Q - \frac{Q}{1 - Q} \rho(\beta_0 + \beta_1 T^{-1} + \beta_2 \rho) \right] + pK_{H_2O}^{IG} + 2 \log_{10} \left \frac{m^0 M_{H_2O}}{10^3} \right \quad (2-3)$
Scaling Factor for Solvation Dynamics ^{88, 89}	$Q = \left(\frac{\rho}{\rho^0} \right) e^{(\alpha_0 + \alpha_1 T^{-1} + \alpha_2 T^{-2} \rho^{2/3})} \quad (2-4)$
Liquid Water Density ⁸⁶	$\rho^L = \rho_c \left(1 + b_1 \vartheta^{\frac{1}{3}} + b_2 \vartheta^{\frac{2}{3}} + b_3 \vartheta^{\frac{5}{3}} + b_4 \vartheta^{\frac{16}{3}} + b_5 \vartheta^{\frac{43}{3}} + b_6 \vartheta^{\frac{110}{3}} \right) \quad (2-5)$
Compliment of the Reduced Temperature ⁸⁶	$\vartheta = 1 - \frac{T}{T_c} \quad (2-6)$

where n is the ion coordination number; Q is a scaling factor for the inter-molecular distance due to solvation, cavity formation, and electrostatic effects; ρ , ρ^0 , and ρ_c are the density, standard density ($(\frac{1g}{mL})$), and the critical density of water, respectively; m^0 is the standard molality ($(\frac{1mol}{kg})$); M_{H_2O} is the molecular weight of water; T and T_c are the absolute system temperature and the absolute critical temperature of water, respectively; and α_i , β_i , γ_i are empirically determined constants. For brevity, the reader is referred to the freely available online references for exact values for these constants.

The IAPWS has also suggested a formulation of the relative permittivity of water as a function of temperature and pressure. The Harris and Alder⁹⁰ formulation of the dielectric constant is

Harris-Alder Dielectric Constant Model	$\frac{(\epsilon_r - 1)}{(\epsilon_r + 2)} = \frac{N_A \rho}{3} \left[\frac{\alpha}{\epsilon_0} + \left(\frac{g \mu^2}{3k_B T \epsilon_0} \right) \left(\frac{\epsilon_r}{(2\epsilon_r + 1)(\epsilon_r + 2)} \right) \right] \quad (2-7)$
---	--

where ϵ_r and ϵ_0 are the relative permittivity of H_2O and the absolute permittivity of free space, respectively; N_A is Avogadro's number; α is the mean molecular polarizability; and μ is the dipole moment of water. g is a factor that accounts for the complex interdependency of the molecular orientations, positions, and both polar and non-polar contributions to their interactions. These features can lead to significant induced polarization, further complicating

the matter.⁹¹ Related concepts were discussed in Chapter One; specifically the sections on ionic strength, activity coefficient, and discussions of water molecules near a charged surface. Because of these complexities, the complete analytic form of g has not been generally derived aside from rearrangement of equations involving dielectric constant. However, the dielectric constant can be presented as the root of equation (2-7), along with an empirical formulation of the Harris-Alder g -factor by the IAPWS^{91, 92}:

Harris-Alder Dielectric Constant	$\varepsilon_r = \frac{1 + A + 5B + \sqrt{9 + 2A + 18B + A^2 + 10AB + 9B^2}}{4 - 4B} \quad (2-8)$
----------------------------------	---

Auxiliary Variable - A	$A = \frac{N_A \mu^2 \rho g}{\varepsilon_0 k_B T} \quad (2-9)$
------------------------	--

Auxiliary Variable - B	$B = \frac{N_A \alpha}{3 \varepsilon_0} \rho \quad (2-10)$
------------------------	--

Harris-Alder g -factor – Empirical Function	$g = 1 + \sum_{h=1}^{11} N_h \left(\frac{\rho}{\rho_0}\right)^{i_h} \left(\frac{T_c}{T}\right)^{j_h} + N_{12} \left(\frac{\rho}{\rho_c}\right) \left(\frac{T}{228K} - 1\right)^{-1.2} \quad (2-11)$
---	---

where N_h , i_h , j_h are empirically determined constants, and again, the reader is referred to the freely available references, should they need the specific values for these terms.

The Debye Length (κ^{-1}) in the Gouy-Chapman form of the double layer (Equation (1-44)) also should be used in its general form, given in terms of the less rigorous, but more convenient molar-ionic strength ($\frac{mol}{L}$).⁹³ The activity coefficient should as well be generalized, replacing the extended Debye-Huckel form with the Davies form, which is applicable to higher concentrations⁹⁴. Finally, two adjustments are made to the CO₂ equilibrium. First, for simplicity the original model only included an approximation of the dissociation of one of the ionization products of aqueous CO₂. However, because a model was available, and because the influence of temperature on the system is less known, an analytical model for the equilibrium constants to produce hydrocarbonate and bicarbonate were included as well.⁹⁵ Second, the saturation pressure for CO₂ was made to be a function of temperature of the Antoine form up to 31°C, and set to be 0 above that.

Approximate Debye Length⁹³ $\kappa^{-1} = \sqrt{\frac{1000\varepsilon_r\varepsilon_0N_Ak_B T}{2e^2I}}$ (2-12)

Mean Activity Coefficient –
Davies⁹⁴ $\log_{10}|\gamma_i| = -\frac{A|z_1z_2|\sqrt{I}}{1+\sqrt{I}} + 0.15|z_1z_2|I$ (2-13)

Activity Coefficient Ancillary
Equation - A⁹⁴ $A = \left(\frac{\log_{10}|2|}{\ln 2}\right) \left(\frac{e^2B}{8\pi\varepsilon_r\varepsilon_0k_B T}\right)$ (2-14)

Activity Coefficient Ancillary
Equation - B⁹⁴ $B = \sqrt{\frac{2e^2N_A}{\varepsilon_r\varepsilon_0k_B T}}$ (2-15)

$$K_1 = \frac{a_{H^+} \cdot a_{HCO_3^-}}{a_{CO_2} \cdot a_{H_2O}} \quad \ln|K_j| = a_{j1} + a_{j2}T + a_{j3}T^{-1} + a_{j4}T^{-2} + a_{j5} \ln|T|$$

$$K_2 = \frac{a_{H^+} \cdot a_{CO_3^{2-}}}{a_{HCO_3^-}} \quad + (a_{j6}T^{-1} + a_{j7}T^{-2} + a_{j8}T^{-1})(P - P_s)$$

$$+ (a_{j9}T^{-1} + a_{j10}T^{-2} + a_{j11}T^{-1})(P - P_s)^2$$

(2-16)

CO₂ Saturation Pressure –
Antoine Equation (T<31°C)⁹⁶ $P_{sat} = 10^{A - \frac{B}{C+T}}$ (2-17)

where P and P_s are the system pressure and standard pressure (1bar), respectively; and a_{ji} , A , B , and C are adjustable parameters.

The final adjustment to the model involves the adjustment of the equilibrium constant. The RPA-model assumes a Langmuir isotherm, which has the form:

RPA Langmuir Isotherm $\Gamma_{Lang} \left(\frac{mol}{area}\right) = \Gamma_{max} \frac{K_L C_f}{1 + K_L C_f}$ (2-18)

Langmuir Equilibrium Constant $K_L = e^{\frac{-\Delta G_{ads}}{RT}}$ (2-19)

RPA Coulombic Adsorption Assumption $\Delta G_{ads} = \Delta G_{coulombic} = zF\psi_{x=r_{hydrated\ ion}}$ (2-20)

Standard Thermodynamic Equality $\Delta G_{ads} = \Delta H_{ads} - T\Delta S_{ads}$ (2-21)

following equations (1-40), (1-42), and (1-43). However, by dimensional analysis, the Langmuir equilibrium

constant, K_L has units of L/mol (or some similar unit), which is incommensurate with equations (2-19) and (1-42),

as an exponential is unitless. In other words, $K_L \neq K_{ads}$. There is significant discussion in the literature surrounding this issue.⁹⁷⁻⁹⁹ Here, we assume Liu's solution.¹⁰⁰ The activity of an adsorbing ion is:

Activity of an adsorbing ion	$a_i = \frac{\gamma_i C_i}{1 \left(\frac{mol}{L} \right)}$	(2-22)
------------------------------	---	--------

Taking the Langmuir adsorption equation for adsorbate A adsorbing onto surface B to be $A + B \rightleftharpoons AB$, and assuming the activity coefficients of the surface sites to be similar regardless of if they are bound to an adsorbate or not, the Thermodynamic and Langmuir isotherms are:

Thermodynamic Equilibrium Constant of Adsorption	$K_{ads} = \frac{\theta_i}{(1 - \theta_i)\gamma_i C_i} \left(1 \frac{mol}{L} \right)$	(2-23)
---	--	--------

Langmuir Equilibrium Constant of Adsorption	$K_L = \frac{\theta_i}{(1 - \theta_i)C_i}$	(2-24)
--	--	--------

Surface Coverage	$\theta_i = \frac{\Gamma_i}{\Gamma_{i,max}}$	(2-25)
------------------	--	--------

This leads to the final conversion between the two equilibrium constants to be:

Thermodynamic-Langmuir Equilibrium Constant Conversion	$K_{ads} = \frac{K_L}{\gamma_i} \left(1 \frac{mol}{L} \right)$	(2-26)
--	---	--------

As shown in the use of the Davies equation for the activity coefficient (equations (2-12) - (2-15)), this leads to a further temperature dependency on the equilibrium constant used to calculate the uptake from the solution to the RPA-model.

It can be seen from the foregoing equations and associated discussion that the temperature dependency of the RPA-model is not simply found in the terms already present. Indeed, those terms contribute, but to account for the full temperature effect requires significant expansion of the RPA-model.

An Additional Temperature Dependency

As discussed in Chapter One, a typical manner of calculating the intrinsic support parameters is to either fit the RPA-model to data describing the pH-shift of an acidic metal free solution before and after mass titration with the support at high surface loadings (see “The Form of the Revised Physical Adsorption Model”). However, as also stated in that section, another method is glean the number of hydroxyl sites per unit area (N_s) from literature or spectroscopic methods, determine the *PZC* by examining the plateau of a pH-shift experiment at high surface loading, and then fitting the RPA-model by only adjusting the ΔpK . The inclusion of temperature makes this procedure slightly more complex.

N_s should stay the same, barring any surface reaction. However, the equilibrium constants associated with the protonation and deprotonation of those surface sites will be temperature dependent. This is the ΔpK , and if the RPA-model is correct, the temperature dependency should be accounted for and calculatable, given the above adjustments (Chapter Two: Adjustments to the RPA-model). The temperature dependance of the *PZC* however, must be experimentally determined. This is simple enough with careful experimentation. However, the theoretical cause of its temperature dependance may source from different causes. As the *PZC* is the pH_{bulk} whereat the potential determining ions, H^+ and OH^- , equally populate the surface, the *PZC* is both dependent on the surface-ion affinity, and the relative presence of the potential determining ions themselves. In other words, the temperature dependance of the *PZC*, instead of being an intrinsic property of the support, may simply be a function of the auto-ionization constant of bulk water, the temperature dependent form of which has already been given (see equations (2-1) - (2-6)).¹⁰¹ However, this may not always work. Tewari and McLean show that neither alumina nor magnetite follow this trend closely.¹⁰² The equation testing this relation is given by Bérubé and de Bruyn:^{101, 103}

Temperature Dependence of

the *PZC*

$$4.6R \left[\frac{1}{2} pK_w - PZC \right] = \frac{\Delta H^*}{T} - \Delta S^* \quad (2-27)$$

where R is the gas constant, ΔH^* is the enthalpy of moving H^+ or OH^- from the bulk solution to the interface, and ΔS^* is the entropy difference in between H^+ or OH^- in a free solution and at the surface at the *PZC*.¹⁰³

Objectives

The materials used and their properties are shown in Table 2. Materials used, and their properties., and the sequence of work that was done is shown in Table 3. Summary of tasks performed..

Table 2. Materials used, and their properties.

Commercial Name	Formula /Characteristic Property	Purpose	Supplier, Assay
<u>Metal Salts</u>			
Chloroplatinic acid hexahydrate	H ₂ PtCl ₆ .6H ₂ O	Metal Precursor	Sigma-Aldrich, 99.9%
Palladium(II) chloride	PdCl ₂	Metal Precursor	Sigma-Aldrich, 99%
<u>Supports</u>			
α-Al₂O₃	PZC 8.1	Support	SASOL, 40 m ² /gm
CeO₂	PZC 5.9	Support	40 m ² /gm
ZrO₂	PZC 5.7	Support	40 m ² /gm
SiO₂	PZC 3.5	Support	42 m ² /gm
TiO₂	PZC 4.9	Support	102 m ² /gm
BaTiO₃	PZC 8.3	Support	15 m ² /gm
<u>Acid/Base</u>			
Ammonium Hydroxide	NH ₄ OH	Adjust pH (base)	BDH, 5N
Hydrochloric Acid	HCl	Adjust pH (acid)	Sigma Aldrich

Table 3. Summary of tasks performed.

Work Plan				
Task			Primary Objective	
1. Check PZC of			Observe the effect of temperature on PZC.	
Supports	Temperatures			
α -Al ₂ O ₃ , CeO ₂ , ZrO ₂ , SiO ₂ , TiO ₂ , BaTiO ₃	At 0°C, 25°C, 50°C and 75°C			
2. Carry out Uptake survey of			Find the optimum pH for maximum adsorption by SEA at each temperature. Metal concentration kept constant.	
Metal		Supports		Temperatures
Pd	+	α -Al ₂ O ₃ , CeO ₂ , ZrO ₂ , SiO ₂ , TiO ₂ , BaTiO ₃		At 0°C, 25°C, 50°C and 75°C
Pt	+	α -Al ₂ O ₃ , CeO ₂ , ZrO ₂ , SiO ₂ , TiO ₂ , BaTiO ₃	At 0°C, 25°C, 50°C and 75°C	
3. Carry out Isotherm survey of			Measure metal uptake versus metal concentration at constant (optimal) pH. Calculate the thermodynamic parameters.	
Metal		Supports		Temperatures
Pd	+	α -Al ₂ O ₃ , CeO ₂ , ZrO ₂ , SiO ₂ , TiO ₂ , BaTiO ₃		At 0°C, 25°C, 50°C and 75°C
Pt	+	α -Al ₂ O ₃ , CeO ₂ , ZrO ₂ , SiO ₂ , TiO ₂ , BaTiO ₃	At 0°C, 25°C, 50°C and 75°C	
4. Perform RPA modeling			Observe how model predicts the experimental outcome	
5. Correlate thermodynamic parameters to experimental variables and catalyst particle size.			Optimize uptake and the catalytic activity	

Experimental

PZC Determination

For measurement of the *PZC*, high surface loading was used. For all experiments, the *pH* of the starting solution, *pH*₀, was adjusted by *HCl* or *NH₄OH*. However, for some *PZC* measurements *NaOH* was also used to adjust *pH*₀ and investigate the effect. A series of metal-free solutions, each at a different *pH*₀ were made, ranging in value from 1 to 14. The solutions were buffered by their addition to batches of support at very high surface loading in 15mL polypropylene centrifuge tubes. The additions were performed in steps, adding a few dozen microliters at a time, then manually impacting the tubes into the lab bench with full force until visual inspection yielded satisfactory mixing, at which point the cycle of addition and impact was continued. As the powder became more wet, and the pores filled, liquid bridges formed (see Chapter One: Impregnation) and the powder began to ball up. As each liquid

addition led to consolidation of the balls, the amount added was lessened with each step. After achieving a single ball of wetted support (with residue on the wall), the ball was pressed against the membrane of a pH-probe intended for soils and semi-solids, placed down on the bench to minimize movement-caused instability in the measurement, and the pH reading was recorded. This was performed at the temperatures (0-75°C) indicated in Table 3. Summary of tasks performed., achieved by allowing the solution to reach the correct temperature before addition, and subsequent heating after the ball had formed. The slurry tended to slowly lose fluidity, especially at elevated temperatures, so often the reading had to be taken before full stability was confirmed.

Uptake Surveys

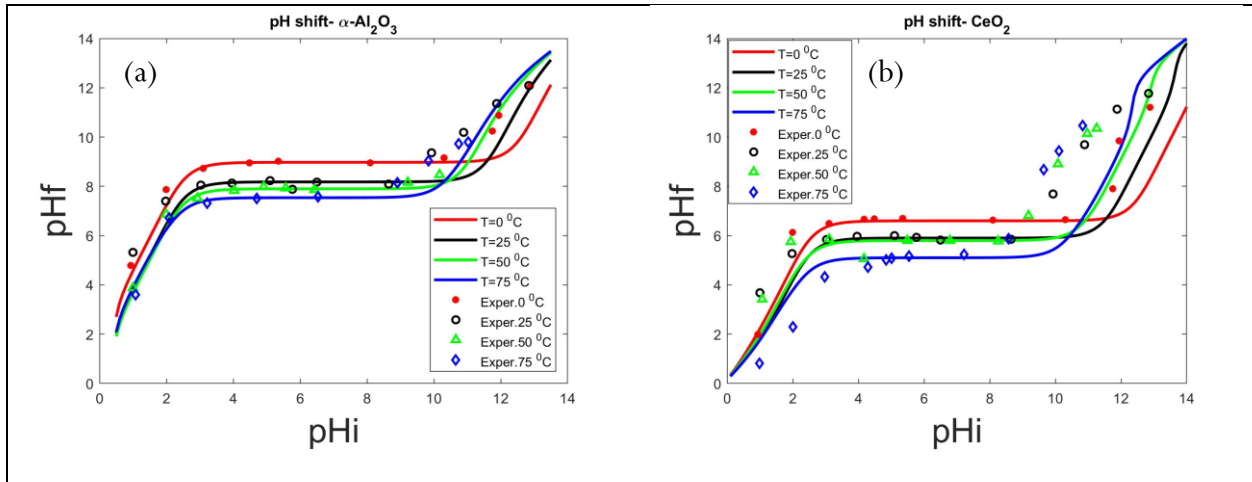
As with PZC determination, the metal solutions were cooled or heated prior to addition of support material for uptake surveys at different temperatures. A 200 ppm (1.0mM) Pt or 100 ppm (0.93mM) Pd solution (metal basis) was used as 1) those have roughly the same molarity and 2) they are slightly higher than the concentrations that would produce a complete monolayer if all metal was adsorbed, assuming similar size and hydration.⁶⁵ The amount of the support in the solution was controlled to give a surface loading (SL) of 1000 m²/L, which for many supports has the consistency of a solution with a lightly suspended powder and may even be transparent. The pH adjusted solutions were mixed with the support in polypropylene centrifuge tubes and placed on an orbital shaker with water bath that was pre-adjusted to temperature for 1 hour at 200 rpm speed. Samples were then one-by-one briefly removed from heating or cooling, quickly filtered, and returned to the heating or cooling container in order to have minimal effect of being removed from elevated or depressed temperature. The filtering was done by 1) removing the plunger from a small syringe (e.g. 5mL), 2) fitting the syringe tip with either a 0.22µm or 0.4µm PTFE disc filter, 3) filling the suspension into the back of the syringe, and 4) reinstalling the plunger to filter the solution into a new polypropylene tube. Finally, pH_f of the filtrate was measured with a probe calibrated to the correct temperature. The samples were then run through an ICP-OES to determine metal adsorption at various temperatures, and pH_0 vs. pH_f and pH_f vs. Γ_L ($\frac{\mu mol}{m^2}$) plots were generated, and the RPA model was fit to the data.

For traditional isothermal analysis (Γ vs C_{metal}), multiple metal solutions were made at various concentrations between 5ppm and 500ppm, metals basis. The pH was then adjusted to achieve maximum uptake, based on the

previously performed uptake surveys (Γ vs pH). These solutions were then added to enough support to achieve a surface loading of $1000\text{m}^2/\text{L}$. The same procedure of addition, shaking, filtering, and measuring as described above for the uptake survey was performed. In excel, the equilibrium concentration (C_{eq}) of each sample was plotted against the uptake (Γ) observed at each temperature. The solver addon to excel was then used to fit the Langmuir isotherm equation (see equations (1-40) and (2-18)), using Γ_{max} ($\frac{\mu\text{mol}}{\text{m}^2}$) and K_L ($\frac{\text{L}}{\text{mol}}$) as adjustable parameters. Using the standard thermodynamic relations (see equations (2-19), (2-21), and (2-26), from K_L was derived the free energy of adsorption, ΔG_{ads} ($\frac{\text{kJ}}{\text{mol}}$), at each temperature, and from these the enthalpy and entropy of adsorption, ΔH_{ads} ($\frac{\text{kJ}}{\text{mol}}$) and ΔS_{ads} ($\frac{\text{J}}{\text{mol}\cdot\text{K}}$), respectively.

Results and Discussion

PZC Determination



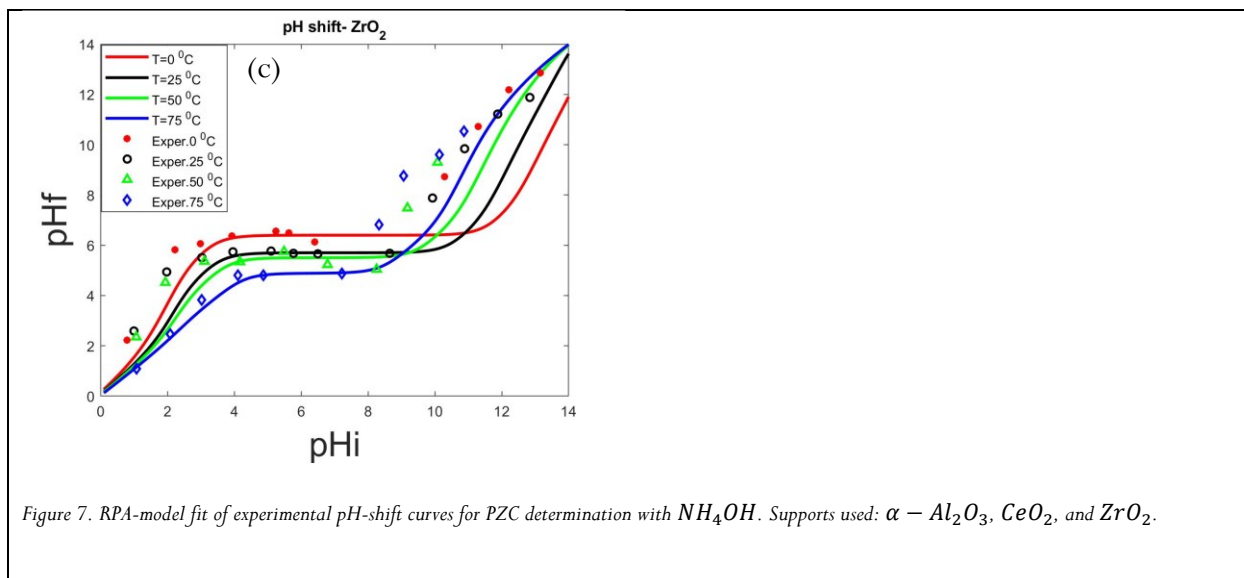
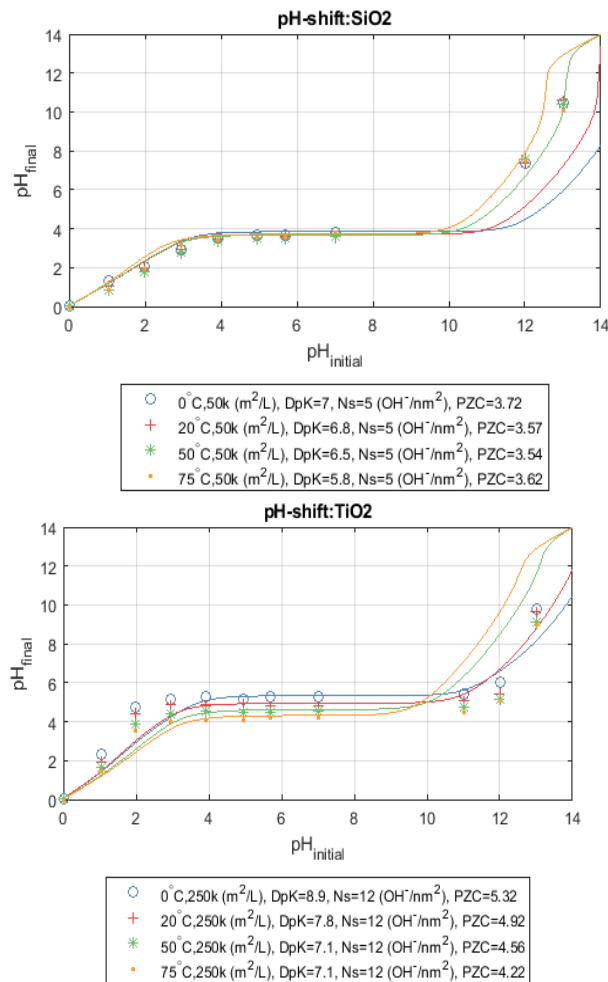


Figure 7 shows the *pH*-shift curves of the high-*PZC* materials used, namely $\alpha - Al_2O_3$, CeO_2 , and ZrO_2 , using *HCl* and NH_4OH to adjust the starting solutions. Temperature (0-75°C) has a moderate inverse effect on the *PZC* when measured by inspection of the plateau and averaging of the values therein. All high-*PZC* materials showed a relatively similar *PZC* for the middle temperatures, while the extreme temperatures showed more deviant behavior, which may be explained by differences in transport of the protons and hydroxides to the surface, especially at low temperatures, or by the fact that these temperatures were nearing the manufacturer specified limits of the pH-probe. Regardless, the RPA model with the previously described temperature adjustments performed admirably in the low and middle regions, capturing the shape, vertical order of the temperatures, and for the most part following very closely to the experimental data. At high *pH*s however, the RPA model was not able to capture well the experimental data, sometimes even mis-ordering the temperatures.

We attempted to include a set of equations modeling both the chemical and phase equilibria phenomena for ammonium, namely is deprotonation into ammonia, and the subsequent equilibrium between dissolved and gas phase ammonia. However, the RPA model became unstable and consistently generated extremely noisy data, with results similar to those from attempts to calculate the RPA model with 2 adjustable parameters (see Chapter One: The Form of the Revised Physical Adsorption Model).

However, this in principle should not cause the behavior seen in Figure 7. If $NH_4(aq)$ protonates, leaves the solution into the gas phase and escapes through the space between the threads in the cap and into the hood vacuum, a proton will permanently remain, and the pH_f should be lower than predicted (as the RPA model doesn't account for these equilibria) for a given pH_0 . This is expressly the opposite effect that happens, as the increase in pH_f with increasing pH_0 happens at a dramatically lower pH than that predicted by the RPA-model. Another possibility is the formation of NH_3 micro-bubbles at the probe-solution interface. These bubbles would 1) disrupt and slow the flow of protons into the junction, 2) possibly perform chemistry with the protons at the bubble solution interface, and 3) create a gas-solid interface at the junction. The combination of these effects could significantly influence both the proton concentration and overall conductivity at the membrane.



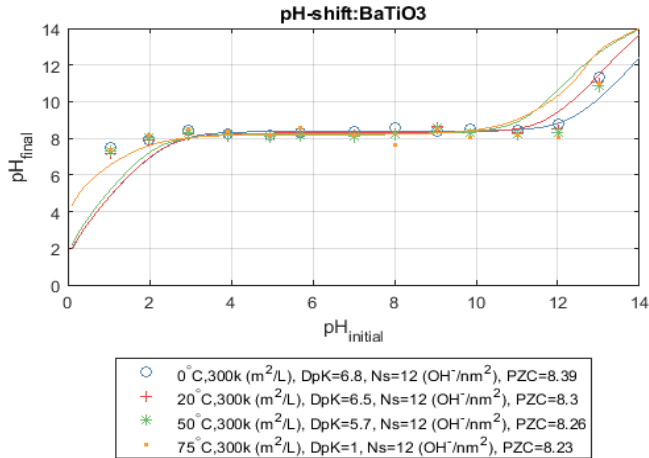


Figure 8. RPA-model fit of experimental pH-shift curves for PZC determination with NH₄OH. Supports used: SiO₂, [TiO]₂, and BaTiO₃.

For the low-*PZC* materials, a similar trend with temperature was followed as with high-*PZC* materials. SiO₂ and TiO₂ had lower *PZC*'s with increasing temperatures. However, while the change for TiO₂ was noticeable, that for SiO₂ was negligible. As before, the low-*PZC* materials were closely modeled at low *pH*, but high *pH* was difficult to model. Unlike before, however, while the *pH_f* as various temperatures converged, the mean value was not entirely distinct from the model-predicted *pH_f*. It is unknown why these materials are present slightly different behavior.

Barium titanate presented a challenge for modeling using the RPA model because there is no reference in literature to the N_s value. We assumed 12 OH/nm^2 because that was the value used for titania. Barium titanate performed similarly to silica and titania in that 1) the spread between pH-shifts at high pH's was overestimated by the RPA model when compared to the experimental data and 2) the middle starting pH region was well described by the model. Like titania, there is also significant underestimation of the final pH value, but unlike silica and titania, there is predicted deviation across temperatures at low pH's. This is likely due to the near 5 point drop in predicted DpK from 50°C to 75°C . Also, interesting to note is that the pH-shift of barium titanate is flat for almost the entire initial pH range. There is some indication that barium titanate slowly leaches barium to form free Ba^{2+} ions and a pure titania surface at pH's below 7. This trend continues until around a pH value of 10.5.¹⁰⁴ In addition, barium carbonate is a known surface contaminant, and will dissolve at low pHs into the bulk phase.¹⁰⁵ These two effects could explain

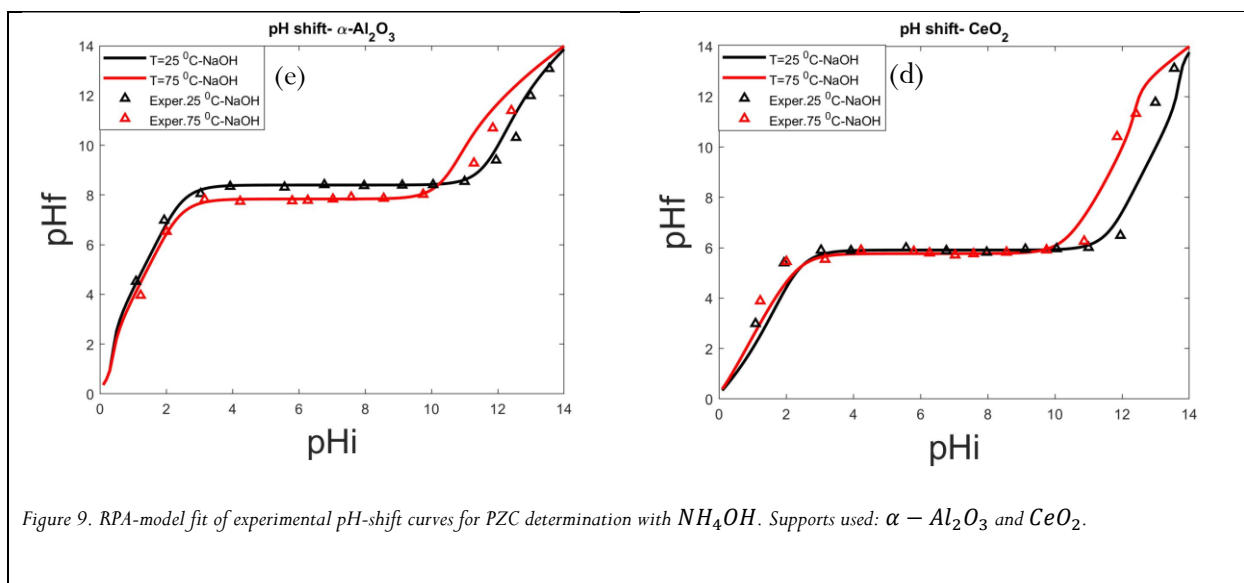


Figure 9. RPA-model fit of experimental pH-shift curves for PZC determination with NaOH . Supports used: $\alpha - \text{Al}_2\text{O}_3$ and CeO_2 .

the comparatively extreme pH-shift, especially at low starting pH's.

To test the “bubble hypothesis,” the same pH -shift experiment was performed at room temperature and 75°C with NaOH . As seen in Figure 9, the data for Al_2O_3 and CeO_2 follow a similar trend to that of the samples made with NH_4OH . The elevated temperature series produces a negative or zero ΔpH at low pH_0 and a positive ΔpH at high pH_0 . $|\Delta pH|$ is certainly lower in the NaOH series, but the RPA model is able to reproduce it well. As far as the comparison to NH_4OH goes, the RPA-model fit is far better, indicating that there are some physical phenomena,

either with the actual double layer, or due to instrumental difficulties, such as the adherence of $NH_3(aq)$ bubbles to the pH probe membrane, that are forcing the deviation of experiment from the RPA-model predicted pH -shift.

Table 4 shows the parameters that were used in or determined by the pH -shift experiment and subsequent RPA-model fit

Table 4. Table of RPA-model determined parameters. N_s was taken from literature, PZC was taken as the arithmetic mean of the pH_f along the plateau of the pH -shift experiment, and ΔpK was fit as the single adjustable parameter in the RPA model. The main set in the upper portion of the table corresponds to experiments done with NH_4OH while the lower set was done with $NaOH$ as the base.

	$T(^{\circ}C)$	$SL \left(\frac{m^2}{L} \right)$	$N_s \left(\frac{OH^-}{nm^2} \right)$	ΔpK	PZC
NH_4OH					
$\alpha - Al_2O_3$	0 20 50 75	36,000	8	4.6 4.5 4.2 4.0	9.0 8.2 7.9 7.5
CeO_2		36,000	11	4.8 4.5 3.8 3.0	6.6 5.9 5.8 5.1
ZrO_2		36,000	11	7.2 7.5 8.0 9.0	6.4 5.7 5.5 4.8
SiO_2		50,000	5	7.0 6.8 6.5 5.8	3.7 3.6 3.5 3.6
TiO_2		250,000	12	8.9 7.8 7.1 7.1	5.3 4.9 4.6 4.2
$BaTiO_3$		300,000	12	6.8 6.5 5.7 1.0	8.4 8.3 8.3 8.2
$NaOH$					
$\alpha - Al_2O_3$	0 20 50 75	45,000	8	4.5 4.0	8.4 7.8
CeO_2		45,000	11	4.5 3.0	5.9 5.8

The results from the equation by Bérubé and de Bruyn^{101, 103} (see equation (2-27)) are shown in Figure 10, and the Enthalpy and Entropy of transport of H^+ and OH^- to the surface are shown in Table 5. Bérubé and de Bruyn were surprised at the low value for ΔS for rutile- TiO_2 . The entropy of our TiO_2 was not only lower, but achieved a negative change in entropy. P90 TiO_2 , in contrast to theirs, is anatase phase. Using molecular dynamics simulations, Zhou et al.¹⁰⁶ showed that the most stable rutile face (100), is known to predominately accept protons directly, while the anatase phase prefers the indirect acceptance of a proton via already adsorbed aqua species. Hypothetically, this could increase the order of the proton placement compared to the rutile phase, and thus decrease entropy.

However, in congruence with the results already mentioned by Tewari and McLean¹⁰², the temperature dependance of the Al_2O_3 PZC is not well modeled by equation (2-27). This could be due to a variety of causes, such as strong coordination to the surface by water (some have called this an ice-like phase¹⁴ (see Introduction to Heterogeneous Catalyst Synthesis and the Underlying Physics Chapter One: Pore Imbibition and Structure of Intergranular Solution), hindering an approach by H^+ , or simply that the PZC of Al_2O_3 is intrinsically a function of temperature, aside from

the temperature dependency of the pK_w . In addition, ZrO_2 and CeO_2 follow equation (2-27) only sub-optimally. Because of these failures, equation (2-27) is not recommended by the author until these difficulties can be resolved. The thermodynamic values are given in Table 5 for completeness and to add to the published data in the literature. However, it can be concluded that the temperature dependence of the PZC of oxides is much better modeled by the Gouy-Chapman treatment of the electric double layer coupled with the non-Nernstian amphoteric surface model found in the RPA model.

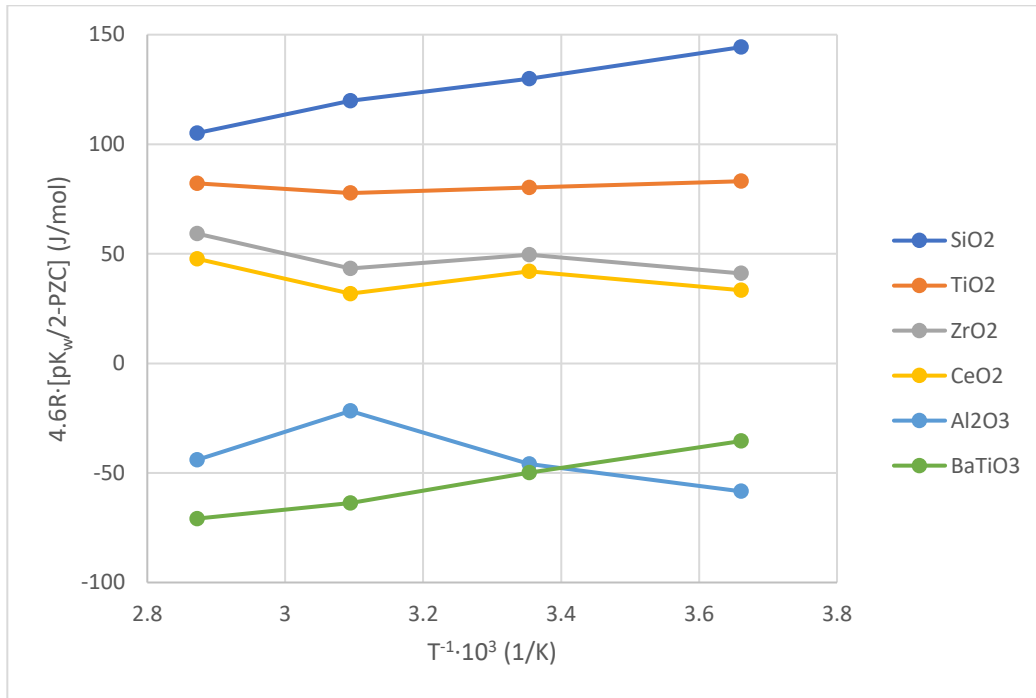


Figure 10. Fit of temperature dependent equation (2-27) to PZC data for supports studied

Table 5. Theoretical Enthalpy and Entropy of transport of H^+ and OH^- to the surface.

	SiO ₂	TiO ₂	ZrO ₂	CeO ₂	Al ₂ O ₃	BaTiO ₃
$\Delta H \left(\frac{kcal}{mol} \right)$	11.57	0.59	-4.27	-2.89	-6.58	10.99
$\Delta S \left(\frac{kcal}{mol \cdot K} \right)$	7.72	-17.40	-25.41	-18.63	-11.20	48.80

Uptake Modelling

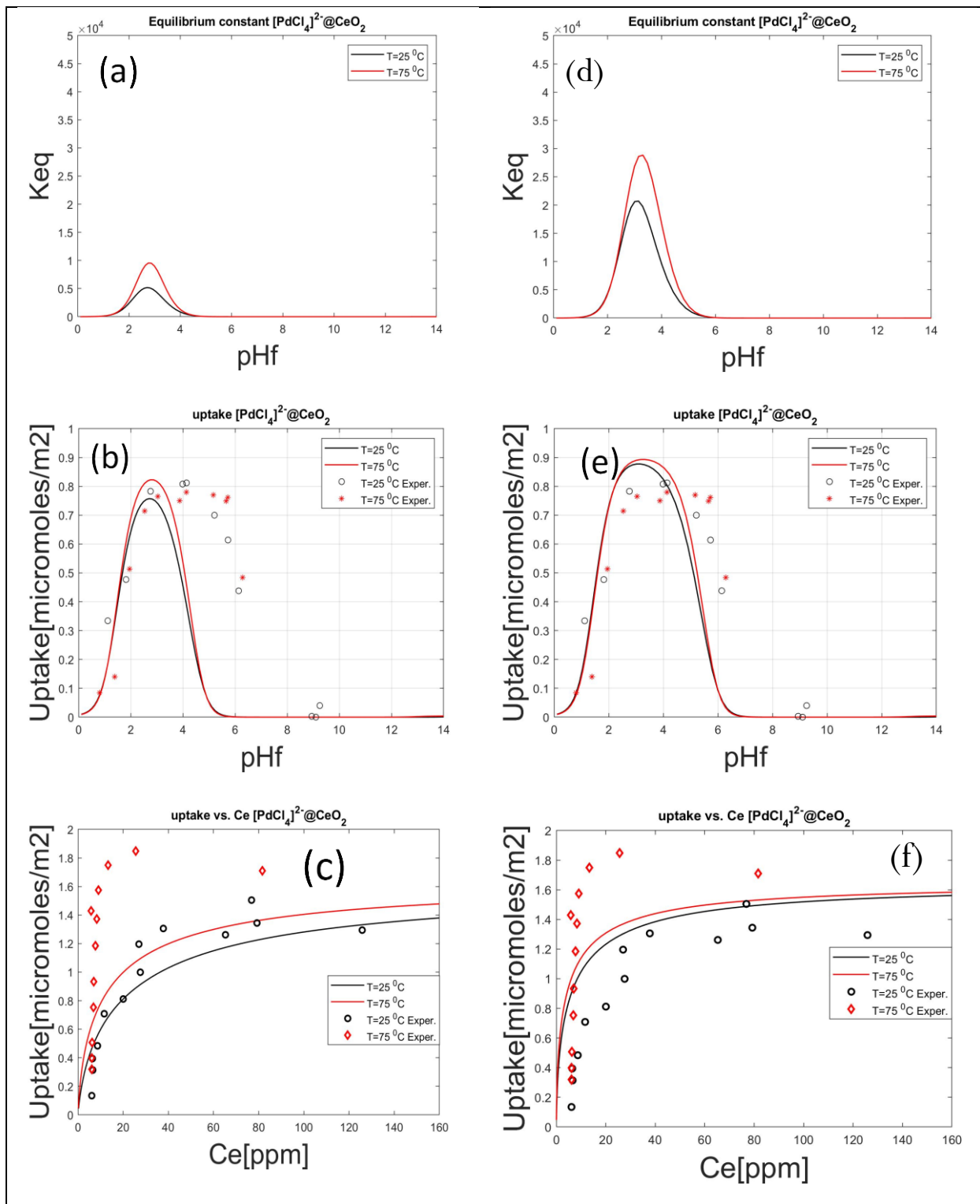


Figure 11. $[PdCl_4]^{2-}@CeO_2$: RPA-modeled adsorption equilibrium constant, experimental and RPA-modeled Uptake vs. pH, and experimental and RPA-modeled Langmuir Isotherm. Temperature shown is at room temperature and 75 °C. The left column uses the experimental PZC (5.9, 5.1), while the right uses literature values for the PZC (7.1, 7.0). See text for details

The effect of temperature on the adsorption of Pd-complexes onto CeO_2 from 100ppm solutions using uptake and isotherm surveys, which were then simulated using the RPA-model. Figure 11 shows experimental data and RPA-modelling of the adsorption of $[PdCl_4]^{-2}$ onto CeO_2 at different temperatures. On the left, the *PZC* values determined in the previous section were used. However, the higher-*pH* side of the uptake volcano curve did not compare well to the RPA model. Korah et al.¹⁰⁷ have shown that while impurities of oxides can contribute to shift in the measured *PZC*, the uptake of the metal trends as if the *PZC* was that of the pure support. They suggest that this is because once wetted, the dopant dissolves into the interfacial water, freeing the support to operate with a clean surface. For this reason, Figure 11 shows on the right a similar series as on the left, but with literature values of *PZC*, which are significantly different from those determined in the previous section. Indeed, while not perfect, the fit with the literature values for *PZC* is much better than with those values determined in this study. This gives strong indication that the CeO_2 used in this study was not fully pure.

The monolayer condition to adsorption (equation (2-18)) also is shown to be in full effect as the increase in equilibrium constant from the left to the right widens the uptake curve yet does little to the maximum uptake. Finally, the literature *PZC*-derived RPA model not only fits the whole of the dataset better, it also follows the experimental data better in that there is little difference in the adsorption between temperatures. However, looking at the isotherms at the bottom, this is clarified. The experimental isotherms show a large difference in rate of increase in uptake with temperature, which fits well with the equilibrium constant plot. As the equilibrium constant is on the order of 10^4 , and the max uptake is around 0.8, the metal should be almost entirely adsorbed. Comparing with an uptake of around 0.8 on the isotherm, both temperatures are at about the same position. Thus, no difference in uptake values would be expected. If higher uptake experiments are done in the future, then a dramatic difference may be seen between the two temperatures.

It is also of note that an uptake of more than 0.8 is seen in the isotherms, which is about the amount a noble metal complex with two hydration sheaths with adsorb. Chloride precursors tend to adsorb with just one hydration sheath, and palladium chloride in particular does not adsorb highly.¹⁰⁸ Cho and Regalbuto instead suggested that metals may in-fact share hydration sheaths in some cases.¹⁰⁸ This is a possibility here.

As shown in Figure 11, adsorption of $[PdCl_4]^{-2}$ onto CeO_2 and the equilibrium constant increased when the temperature increased. The equilibrium constant as a function of pH at the two adsorption temperatures is shown in Figure 2a and 2d, the uptake versus pH at constant metal concentration in Figures 2b and e, and the uptake versus metal concentration at constant pH in Figure 11c and f. Figure 11 (a-c) were simulated with the measured PZCs = [5.9, 5.8], but the RPA model does not fit the experimental data very well. In a previous investigation it was shown that ionic impurities at the surface of the support could alter the PZC value, but not affect the adsorption of the metal.⁸⁴ However, the RPA model can fit the experimental data much better with the reported PZC of ceria, as depicted in Figure 12(d-f). The used ceria needs to be verified for impurities by washing it with both basic and acid solutions and DI water and measuring the resultant PZC.

The effects of temperature on the adsorption of Pt on ceria were shown in Figure 12. Similarly, the equilibrium constant and the adsorption of CPA on ceria increased as the temperature increased. Moreover, with the modified PZC = [7.1, 7.0], the RPA model can obtain a better simulation with a slightly higher adsorption and broader volcanic plots in the uptake survey due to the increase of equilibrium constant.

Experimental and modeling data for Pt hexachloride on alumina are shown in Figure 13. To improve simulation by the RPA model, the effects of the support protonation and deprotonation constants (pK1 and pK2) were explored. These constants are equidistant from the support PZC, that is, $PZC = (pK1 - pK2)/2$, and the difference $pK1 - pK2$ is termed DpK. The effect of changing DpK on the simulation of Pt hexachloride on α -alumina was investigated, as shown in Figure 13. Different DpKs displayed varied trends in the equilibrium constants and adsorption of Pt hexachloride on α -alumina. In Figure 13 (a-c), with a lower DpK, equilibrium constant and adsorption of Pt hexachloride declined with increasing temperature, while they increased with higher DpKs as temperature increased, shown in (d-i). With a higher DpK, RPA model showed a lower equilibrium constant and adsorption of Pt hexachloride on α -alumina as well as a narrower volcanic plot in the uptake survey. With DpK = [8.0, 5.0], the RPA model gives the optimal simulation for Pt hexachloride on α -alumina.

The same phenomena were observed on the effects of DpK on equilibrium and adsorption of $[\text{PdCl}_4]^{2-}$ on α -alumina, displayed in Figure 14. For Pt, anionic metal complexes are thought to retain one hydration sheaths (number of hydration sheath “nh”) and cationic ones two. And, while the RPA model can fit the experimental data of $[\text{PdCl}_4]^{2-}$ on ceria with nh=1 (Figure 14), for $[\text{PdCl}_4]^{2-}$ on α -alumina, RPA simulation with nh=1 showed a much higher adsorption of Pd than the experimental data. Hence, RPA model simulation with nh=2 was carried out on $[\text{PdCl}_4]^{2-}$ on α -alumina and the simulations are shown in Figure 15.

Compared with the RPA simulation with nh=1, a much better fit can be obtained by using nh=2 as 2 hydration sheaths outside of the metal complex resulted in a lower maximum adsorption of metal. And with the adjusted parameters of nh=2 and $\text{DpK} = [8.0, 5.0]$, RPA model can simulate the uptake and isotherm of $[\text{PdCl}_4]^{2-}$ on α -alumina well.

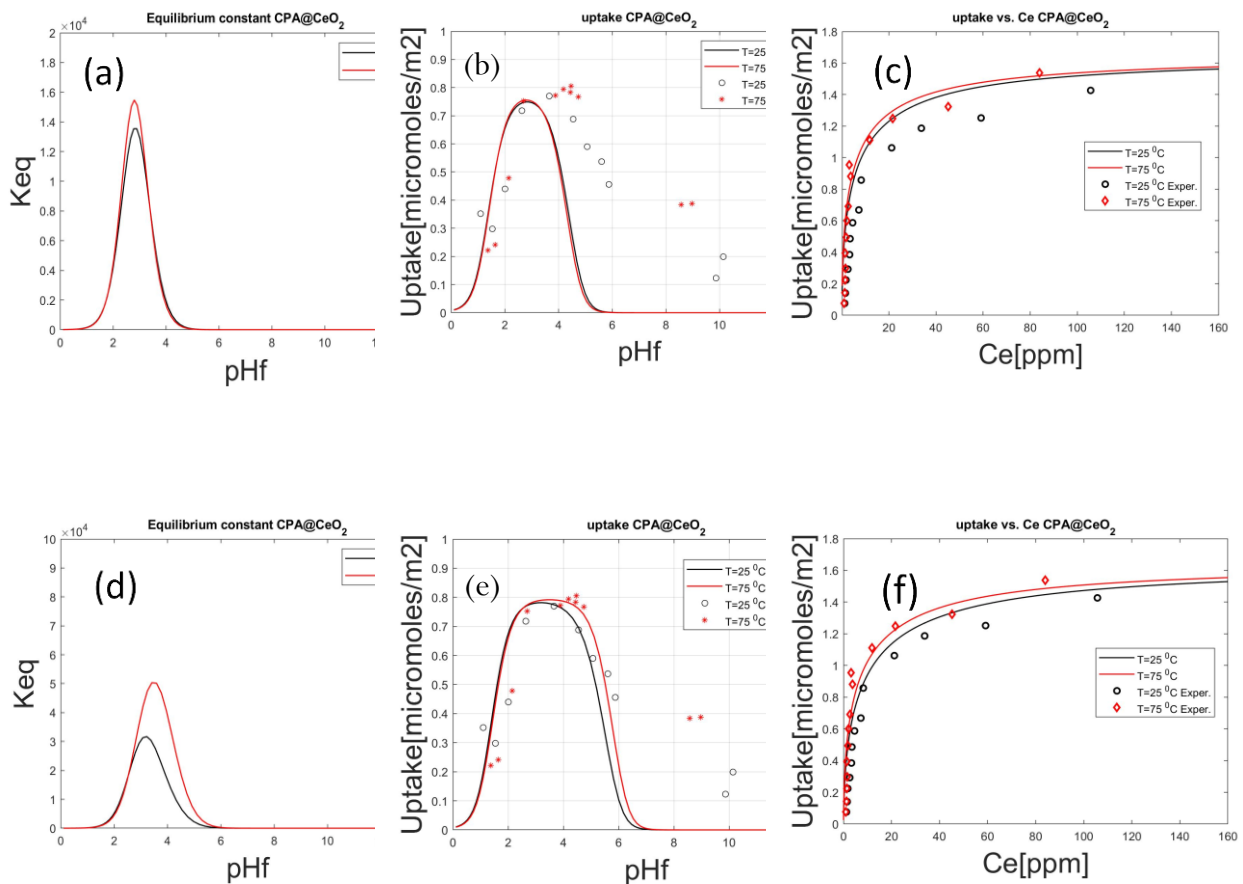


Figure 12. Uptake survey and isotherm of Pt on CeO₂ by RPA model with PZC= [5.9, 5.8] (a-c) and [7.1, 7.0] (d-f) at T= [25 OC, 75 OC].

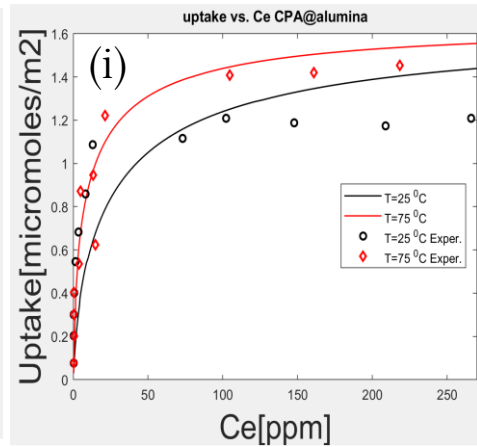
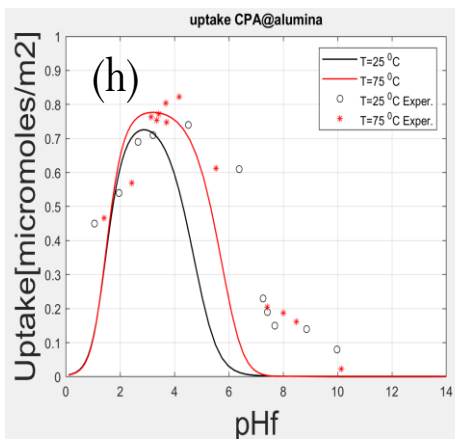
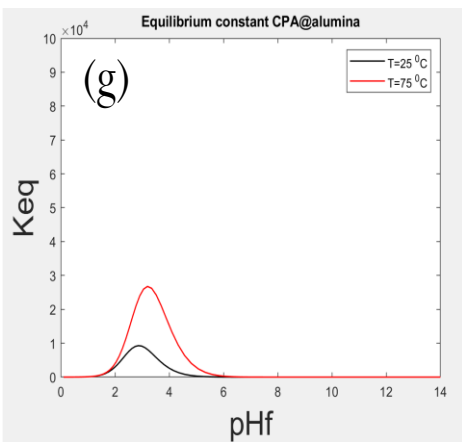
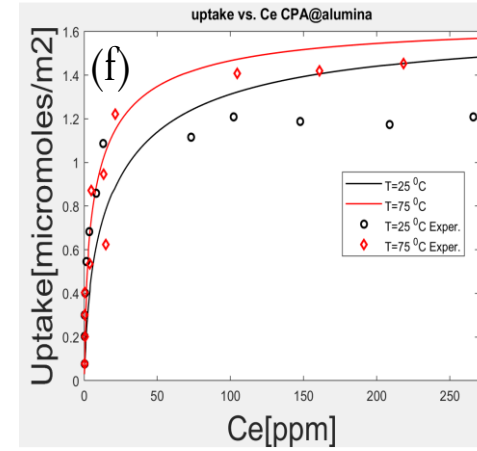
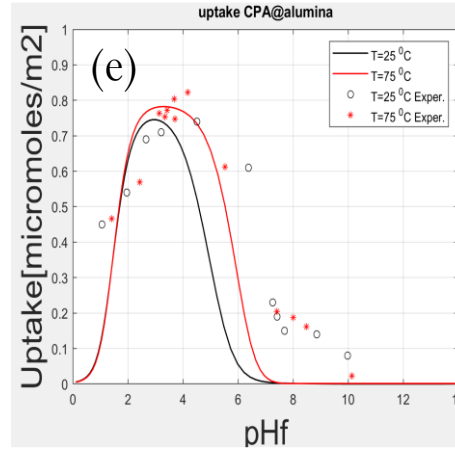
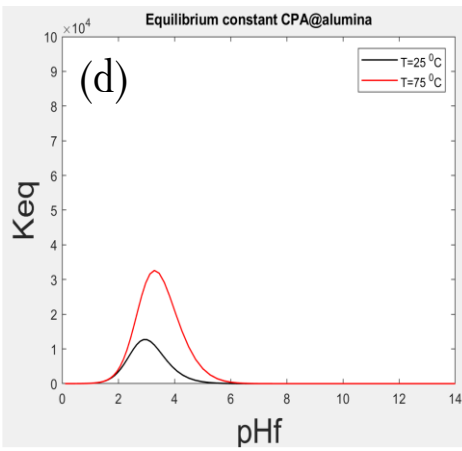
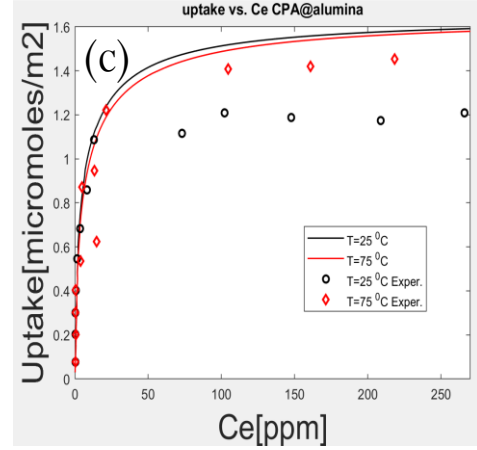
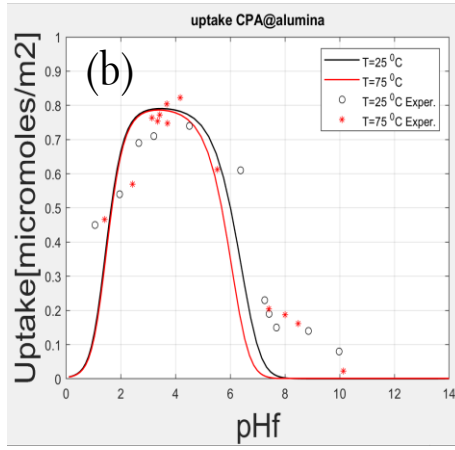
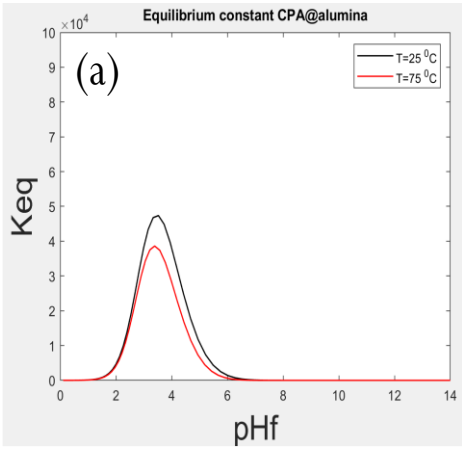
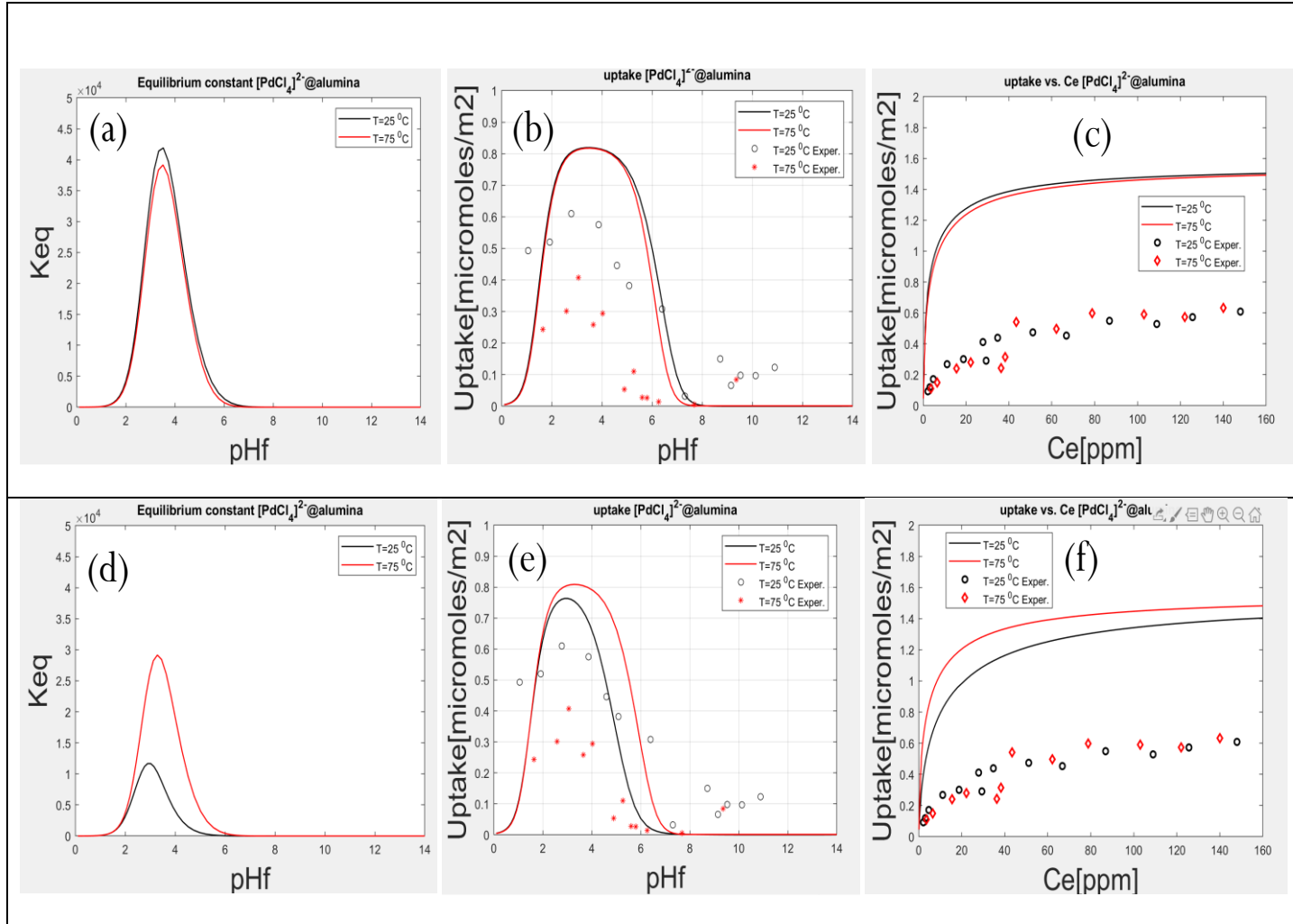


Figure 13. Uptake survey and isotherm of Pt on α -alumina by RPA model with $DpK = [4.5, 4.0]$ (a-c), $[7.5, 4.5]$ (d-f) and $8.0, 5.0]$ at $T = [25\text{ }^{\circ}\text{C}, 75\text{ }^{\circ}\text{C}]$.



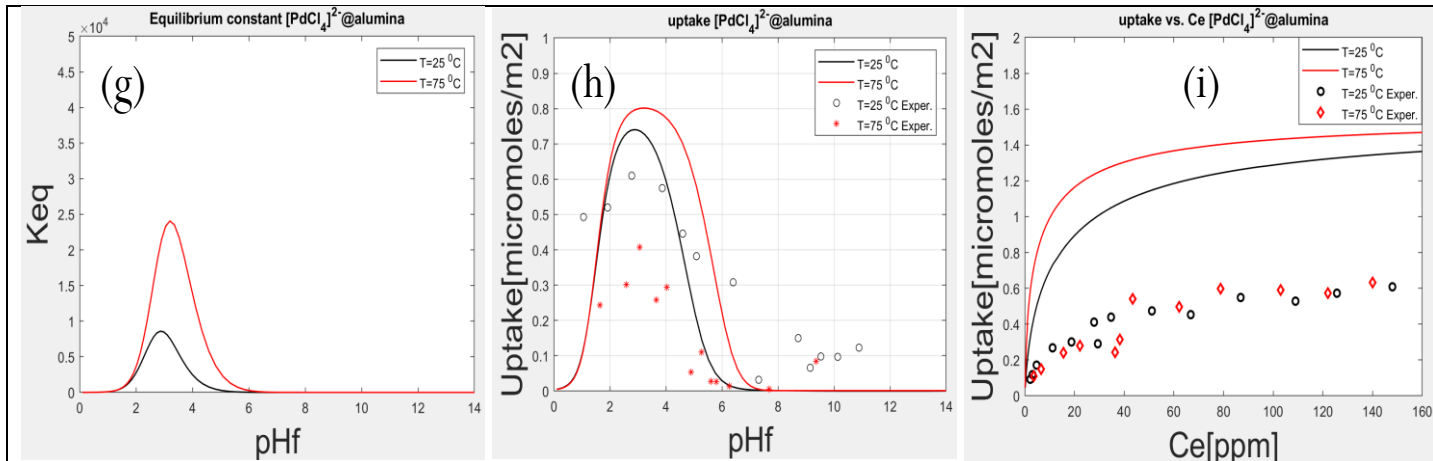
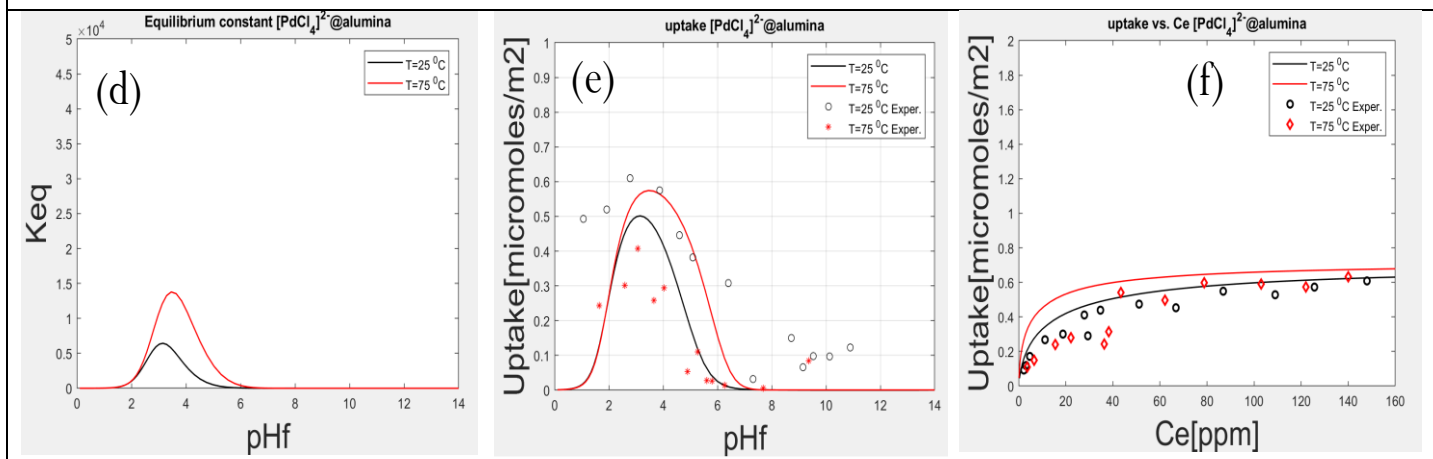
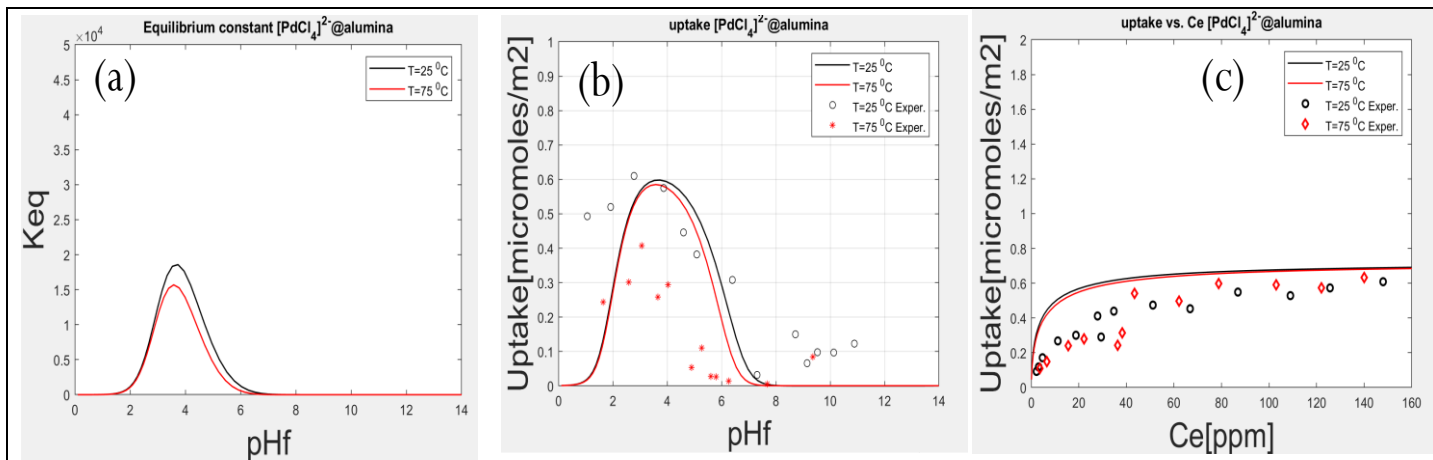


Figure 14. Uptake survey and isotherm of Pd on α -alumina by RPA model $nh=1$ and $DpK = [4.5, 4.0]$ (a-c), $[7.5, 4.5]$ (d-f) and $8.0, 5.0]$ at $T = [25^\circ C, 75^\circ C]$.



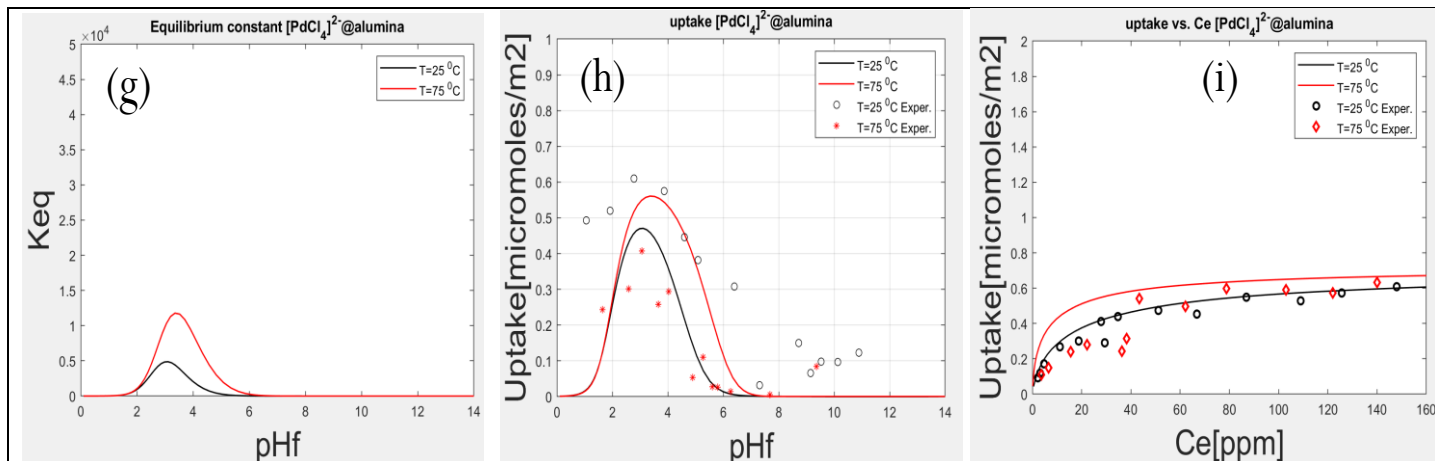
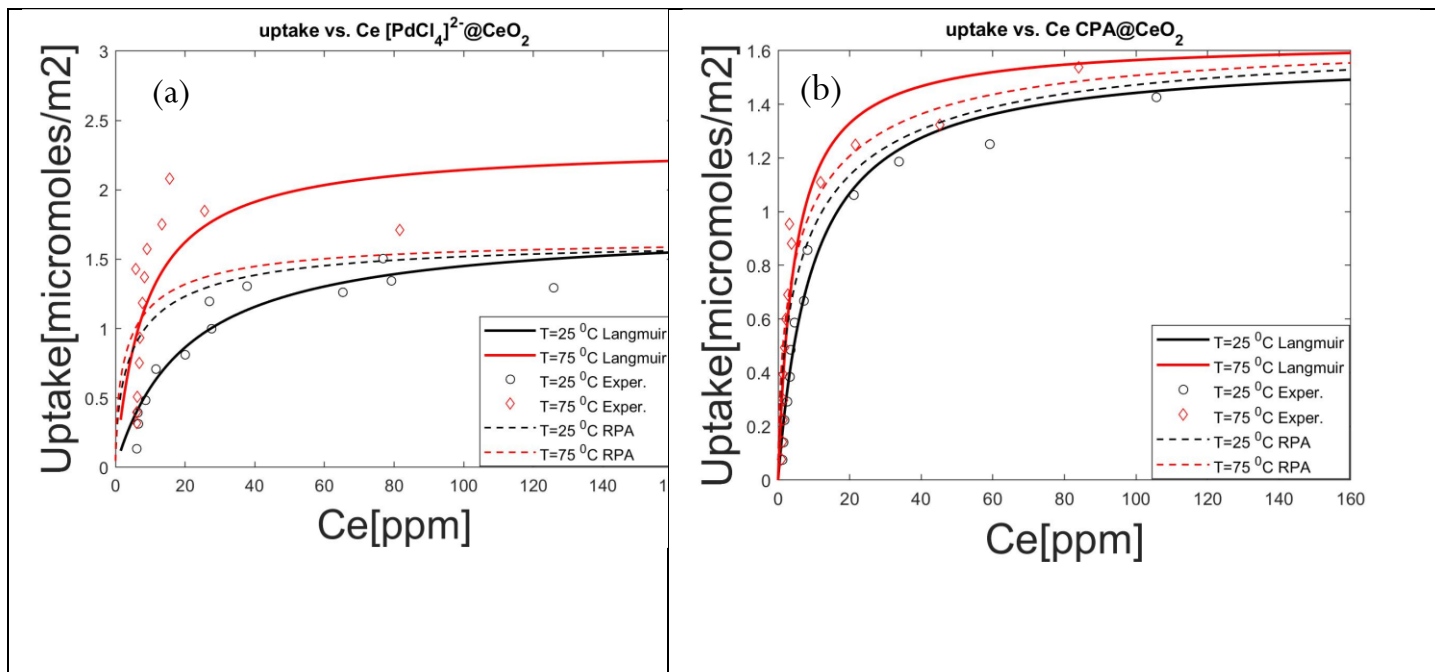


Figure 15. Uptake survey and isotherm of Pd on α -alumina by RPA model $nh=1$ and $DpK = [4.5, 4.0]$ (a-c), $[7.5, 4.5]$ (d-f) and $8.0, 5.0]$ at $T = [25 \text{ } ^\circ\text{C}, 75 \text{ } ^\circ\text{C}]$.

Isotherm Modelling



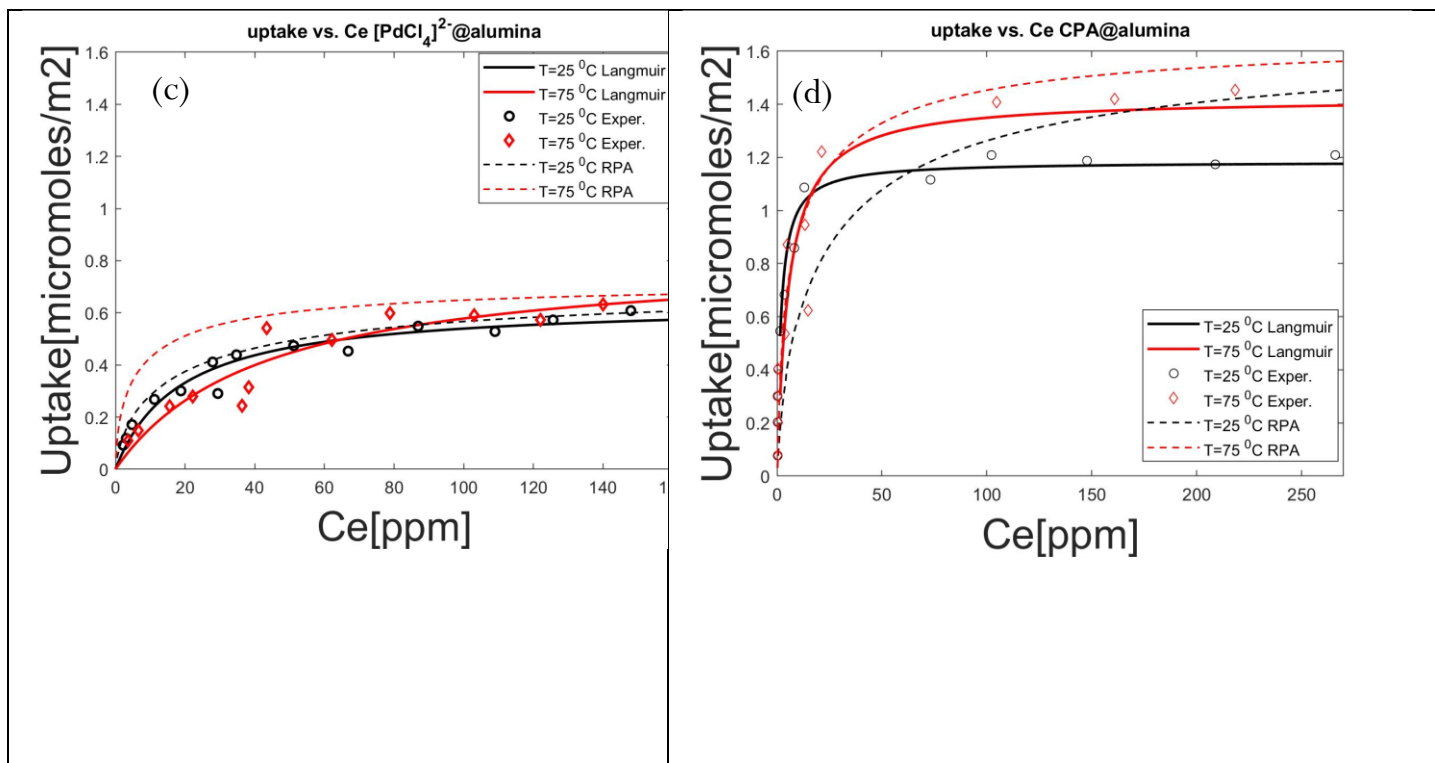


Figure 16. Isotherms of Pd, Pt on α -alumina, ceria with Langmuir model and compared with RPA model

Table 6. Derived Thermodynamic Function from Langmuir Model

Metal on material		ΔG (KJ mol ⁻¹)		ΔH (KJ mol ⁻¹)	ΔS (KJ mol ⁻¹)
		25 °C	75 °C	25 °C & 75 °C	
Pt	α -alumina	-55.1	-61.5	-17.8	-0.13
	ceria	-51.1	-62.0	12.2	-0.2
Pd	α -alumina	-48	-53.9	-13.9	-0.12
	ceria	-47.8	-58.5	14.1	-0.21

Figure 16 shows the simulation for the isotherms of $[PdCl_4]^{2-}$, Pt hexachloride on ceria, α -alumina with Langmuir model and compared with RPA model. The simulations by Langmuir and RPA models are close. Both of them can fit the experimental data well.

Synthesis of Pd- and Pt-catalysts at varying temperatures

To investigate the effects of temperature on metal particle size, monometallic catalysts of Pd, Pt on α -alumina and ceria were prepared by strong electrostatic adsorption (SEA) method at two different temperatures (250C and 750C) over the high ZPC supports of alumina and ceria. Anionic precursors of palladium tetrachloride and platinum hexachloride was used over high PZC α -alumina and ceria. Palladium dichloride powder was dissolved in acidic DI water with the molar ratio of Pd to HCl as 1:2. To get a stable Pt-Cl coordination, chloroplatinic acid solution was aging according to the procedure in Spieker, et al.⁵⁸ All the catalysts were prepared at the optimized pH determined by the uptake survey. HCl and NH₄OH were used to adjust the pH values for all the solutions. Surface loading is 1000 m²/L, shake for one hour, then filtered to get the wet catalysts and dry overnight at room temperature. The Pd catalysts were reduced at 200 0C in 20% H₂/N₂ at a ramp of 50C/min. Catalysts' information including the weight percent of Pt, Pd is listed in Table 7.

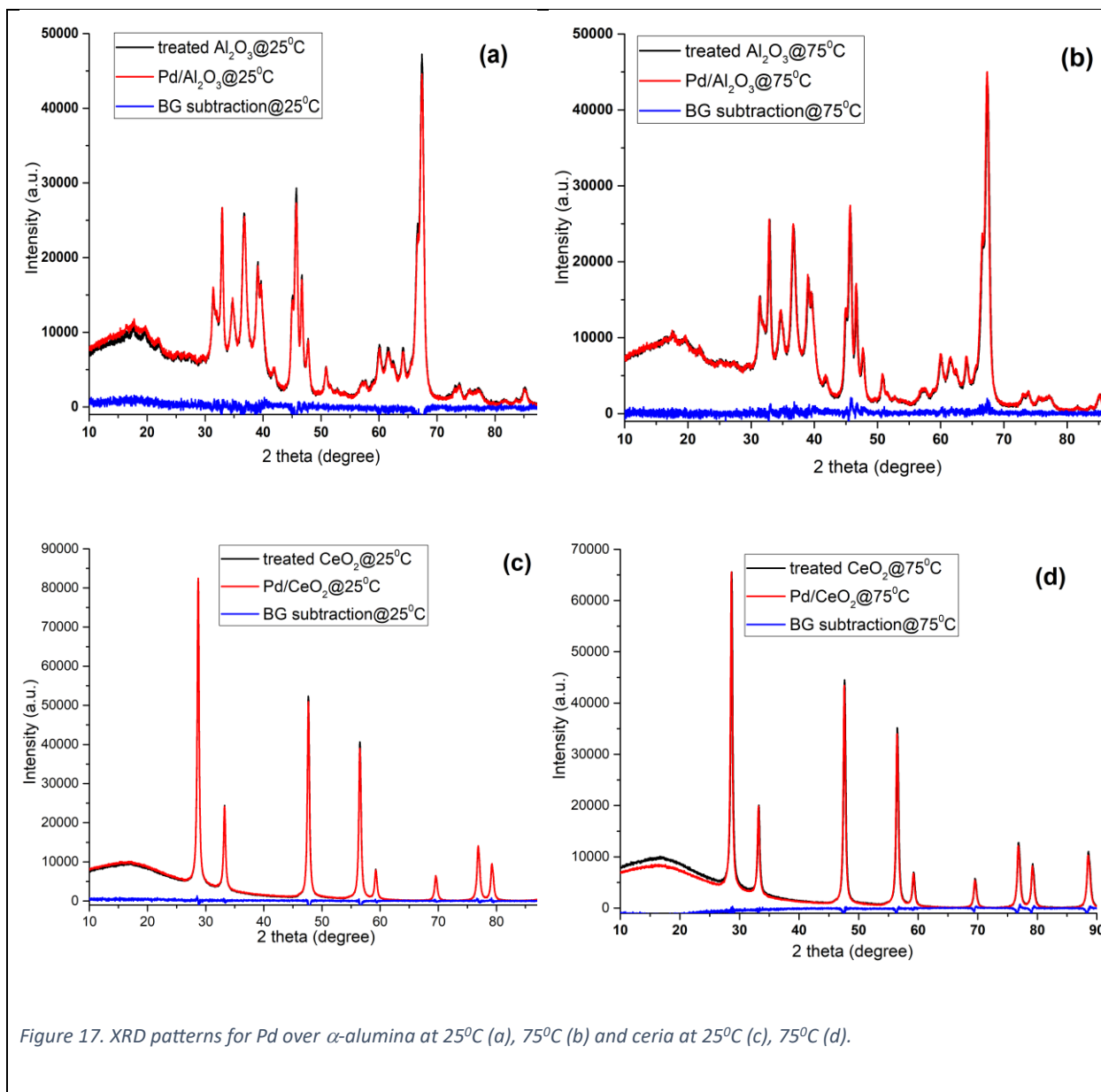
Table 7. Pt, Pd Catalysts Synthesized over α -Al₂O₃ and CeO₂

metal	support	Temperature (°C)	Uptake ($\mu\text{mol}/\text{m}^2$)	Weight percent (%)
Pd	α -Al ₂ O ₃	25	0.73	0.32
		75	0.73	0.32
	CeO ₂	25	0.63	0.33
		75	0.83	0.43
Pt	α -Al ₂ O ₃	25	0.93	0.72
		75	1.00	0.78
	CeO ₂	25	0.83	0.66
		75	0.95	0.76

To check the particle size of Pd and Pt nanoparticles, catalysts were characterized by X-ray diffraction (XRD) using a Rigaku MiniFlex II equipped with a high sensitivity D/tex Ultra Si slit detector. X-ray patterns were recorded from 10-90° 2 θ using a Cu-K α radiation source ($\lambda=1.5406 \text{ \AA}$) operated at 30 mA and 15 kV. The

X-ray patterns were shown in figure 8. The particle size of Pd on α -alumina and ceria at both 25 °C and 75 °C is very small, which is below the detection limit of X-ray equipment.

Additionally, analogous syntheses of cationic Pt and Pd ammine precursors will be conducted at the two temperatures over low PZC titania and silica materials, and these materials will also be characterized by XRD and chemisorption. Uptake data and modeling data for these two systems is given in the following section.



Uptake and Isotherm of High PZC Materials

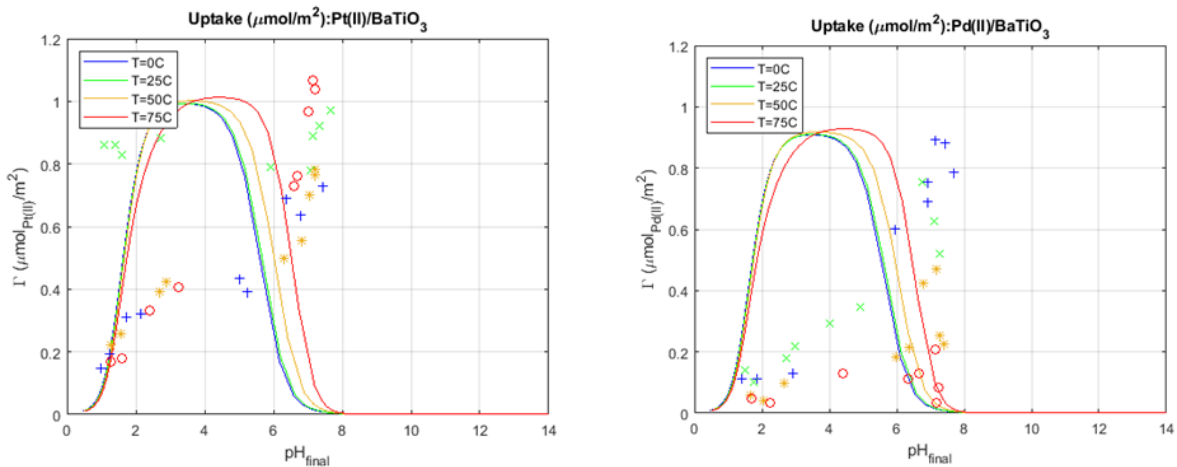


Figure 18. Uptake: Pt(II)/BaTiO₃ (right) and Pd(II)/BaTiO₃ (left)

Pt(II) and Pd(II) adsorption onto barium titanate has differed greatly from the RPA predictions. Both sets of curves had very clearly defined uptake curves but had maximums almost exactly on the PZC of barium titanate. As noted previously, the structure is thought to change into that of titania. If this is happening, with the added complication of pH shifting due to surface barium carbonate, which will basify the solution, the RPA model in its current form may not be equipped to handle barium titanate as a support.

The RPA model for Pt(II) on both silica and titania predicts a switch from positive to negative gibbs free energy around the PZC, as expected. The adsorption equilibrium constant and uptake maximums and the gibbs free energy and surface potential minimums all roughly correspond to each, as predicted by the RPA model. However, the predicted change in adsorption enthalpy and entropy are intriguing. All R² values for both enthalpy and entropy stay at virtually 1 except for at the PZC. For both Pt(II) on silica and titania, enthalpy follows an upward trend toward the PZC, then sharply decreases until roughly the pH value for the maximum uptake. At the pH of the maximum uptake, the enthalpy sharply increases again,

and then slowly lowers. Entropy changes also follow a distinct trend. Entropy values are negative until right around the PZC. They quickly shoot above 0, followed by another sharp fall to slightly above zero. Here the entropy holds virtually constant, with a slight increase at maximum uptake, after which the entropy drops very slightly below zero and holds steady here until pH of 14. Both trends are spoken of very generically in literature, and thus these trends are not well understood currently. Why these trends are shaped this way is actively being considered.

The experiments for uptake determination do not follow well at all the RPA model. Pt(II) on titania follows somewhat for uptake, but the pH-shift curve is completely dissimilar to the RPA model projections. We are unsure of why this is.

For
the

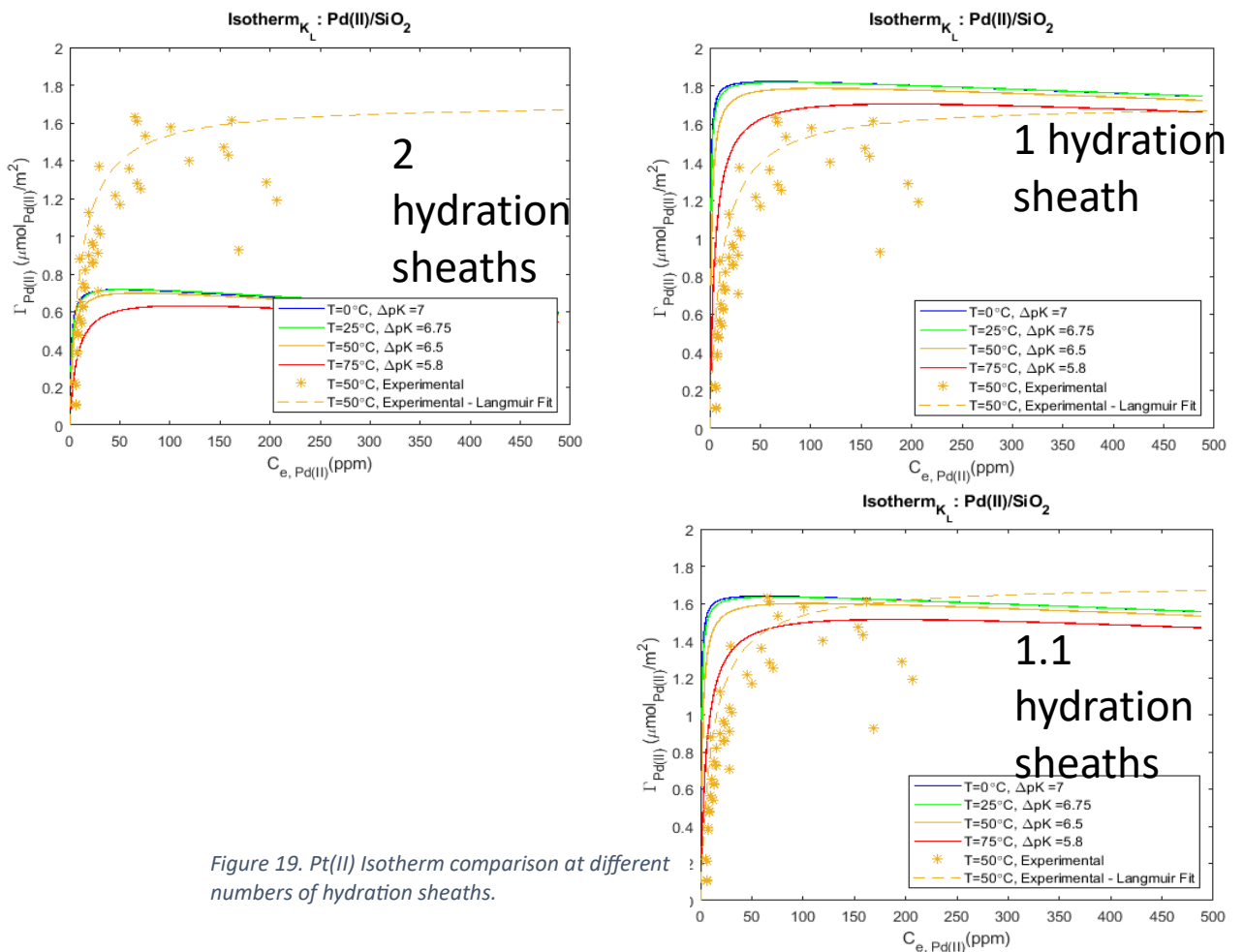


Figure 19. Pt(II) Isotherm comparison at different numbers of hydration sheaths.

isotherm at the pH of maximum uptake for each system, the model was relatively accurate to the data. Pt(II) on silica was almost exactly equivalent to the model at 50°C. At 20°C, the model and experiment differed somewhat, but this was likely due to experimental error, given the shape of the experimental curve. The Pt(II) on titania model initially used 2 hydration sheaths in accordance with past experiments, but that was found to predict roughly half of the experimental uptake. The RPA model was adjusted to have an optimal value of 1.1 hydration sheathes.

Conclusions and Future Work

The PZC of all studied supports decreased with increasing temperature. And RPA simulation of the pH shift on the high PZC materials is better with pH being adjusted by NaOH for NH₄OH due to the additional solution chemistry of the ammonia complex. Temperature has a small but significant effect on the adsorption equilibrium constant and the adsorption of [PdCl₄]²⁻ and Pt hexachloride on α -alumina, ceria, and barium titanate, while being less discernable for Pd(NH₃)₄⁺ and Pt(NH₃)₄⁺ on silica and titania. The impurity of the material has no effects on the adsorption of metal even though the effect on PZC is great. DpK in the RPA model can change equilibrium constant and adsorption of Pt and Pd on α -alumina. The RPA model and Langmuir model can fit the isotherms well, primarily for ceria and alumina.

While further confirmation is needed, the temperature of synthesis does not appear to have a significant effect on the ultra-small size of reduced nanoparticles.

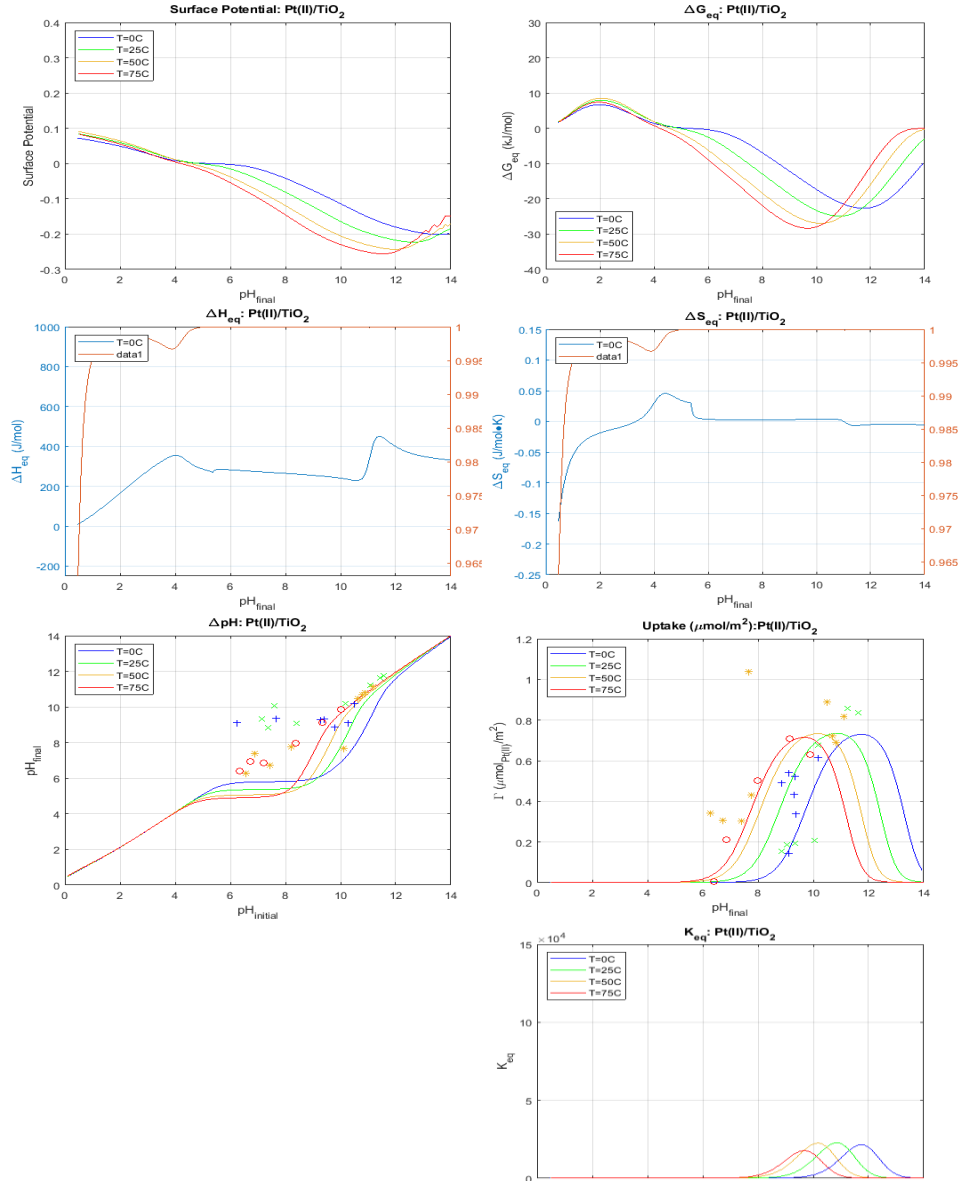
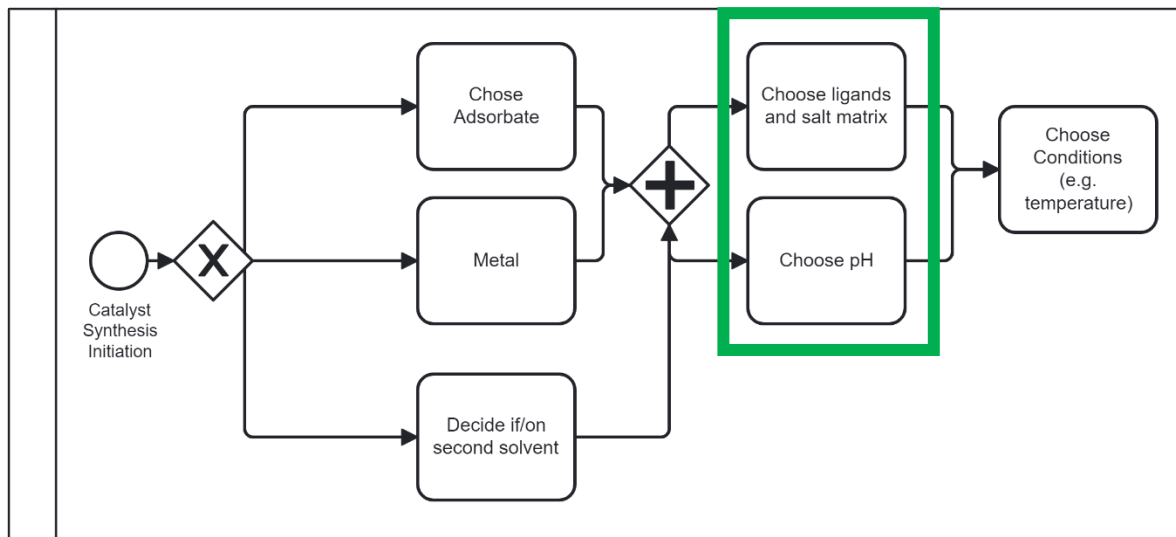


Figure 20. Pt(II)/TiO₂ thermodynamic profile

Chapter Three: Investigation of Platinum and Palladium Deposition using Strong Electrostatic Adsorption Variables



Background

Strong Electrostatic Adsorption (SEA) has been employed with a host of supports and metals to produce highly dispersed supported metal nanoparticles.¹⁰⁹ For some catalytic reactions, however, high dispersion is not desired. Reactivity can be dependent on particle size such that larger particles are in fact optimal. Cobalt nanoparticle size for Fischer-Tropsch Synthesis, for example, is optimal at 6 nm.¹¹⁰ Thorough studies of the dependence of reactivity on supported metal nanoparticle size were planned to feature a catalyst series having a carefully selected range of particle sizes, with tight size distributions. This might be attempted with colloidal methods to produce a carefully controlled series of nanoparticle sizes in solution, and then depositing these particles on a support; however, this methodology suffers from the need to remove the capping agents of the solution-produced nanoparticles, and the thermochemical means to do this often distorts the original particle size.¹¹¹ The ability to synthesize controlled particle sizes with tight size distributions using adsorbed metal precursors (what Schwarz has termed “2 dimensional chemistry” as opposed to “3 dimensional” colloidal syntheses¹¹²). has not been achieved to date. This project attempted to do so by altering the

method of SEA, which normally yields ultra-small nanoparticles in the range of 1 -2 nm with tight size distributions (standard deviations typically 25% of particle size), to yield increased particle size with tight distributions.

An initial attempt to do this with a variation of SEA termed Charge-Enhanced Dry Impregnation (CEDI) was recently made¹¹³ using additional salt (high ionic strength) in the impregnation solutions which decreases precursor-support interaction. Nitrate and citrate ions added to solution gave a small increase in particle size, while chloride and bromide salts at the same atomic ratio gave much larger increases. However, since the halides caused partial ligand substitution in the metal ammine precursors, the presence of two precursor species which reduced at different temperatures caused the particle size distributions to broaden considerably.¹¹³

The goal of this project was to be able to manipulate the conditions discussed in the foregoing paragraphs to vary final particle size. More specifically, we began by varying the metal to anion ratios by adding salt during SEA or charge-enhanced dry impregnation (CEDI) to predictably and reproducibly create supported nanoparticles of precise and narrow particle size distributions. In parallel, we are studying the effect of counterions, anions (NO_3^- and HCO_3^-) and cations (Na^+ and NH_4^+).

Experimental, Results, and Discussion

A series of catalysts with different Pt: NO_3^- ratios on both Timrex HSAG300 carbon support and a Aerosil 300 silica support were synthesized by the SEA and CEDI methods as shown in Table 1. Timrex HSAG300 has a PZC 2.9 and Aerosil 300 has a PZC of 4.1¹¹⁴ so cationic precursor Tetraammineplatinum(II) nitrate was used for adsorption onto both supports. Surface loading was 1000 m^2/L . Max. uptake of Pt (PTA) on HSAG300 was reported to be 0.36 $\mu\text{mol}/\text{m}^2$ @pH_r 12.¹¹⁵ For Aerosil 300, a DOE was performed, varying initial Pt concentration, $\text{H}_2\text{O}/\text{Base}$ (v/v), Pt/anion ratio, cation identity (Na^+ and NH_4^+), and anion identity (NO_3^- and HCO_3^-), and the maximum uptake was found to be around 0.5 $\mu\text{mol}/\text{m}^2$, discounting a few outliers, as shown in Figure 21. SEA Uptake curve for Pt/Aerosil 300. Blue dots represent experimental data, while the orange dotted line shows a quadratic trend of the bulk of the data..

Table 8. Catalysts synthesized testing effect of ionic strength changes on final particle size at pH of maximum uptake.

Anion	Catalyst	Pt:A ⁻	Method	pH _f	XRD Size (nm)
NO ₃ ⁻	1.53% Pt/ Timrex HSAG300	1:0	SEA	12.6	~2.2
	1.14% Pt/ Timrex HSAG300	1:75	SEA	12.4	~2.3
	1.5% Pt/ Timrex HSAG300	1:0	CEDI	9.92	~2.6
	1.5% Pt/Timrex HSAG300	1:40	CEDI	9.48	~2
	2.15% Pt/SiO ₂	1:0	SEA	10.26	<1
	2.5% Pt/SiO ₂	1:8	SEA	9.89	<1
	2.14% Pt/SiO ₂	1:95	SEA	9.87	<1
	2.1% Pt/ SiO ₂	1:40	SEA	9.16	<2
	2.1% Pt/ SiO ₂	1:40	CEDI	9.88	small
CO ₃ ⁻	2.15% Pt/ SiO ₂	1:0	SEA	~10	<2
	2.1% Pt/ SiO ₂	1:40	SEA	~10.6	<2
	2.15% Pt/ SiO ₂	1:0	CEDI	9.62	<2
I ⁻	2.15% Pt/ SiO ₂	1:40	CEDI	~10	large

Characterization of the catalysts in Table 8 was performed by powder x-ray diffraction. XRD analysis of the first catalyst pair, the SEA preparations with the Timrex support, indicates the presence of platinum and platinum oxide Pt₃O₄ with an average particle size of about 2.2 and 2.3 nm respectively for the nanoparticles synthesized with 1:0 and 1:75 ratio of Pt: NO₃⁻, assuming that the Pt oxide exists as a shell over a hemisphere of a Pt core metal. Chemisorption of hydrogen from an oxygen-precovered surface led to particle size estimates of 2.2 and 2.3 nm for the same two samples and was completely consistent with the XRD results. Increasing nitrate in solution during SEA preparation does not appear to affect particle size.

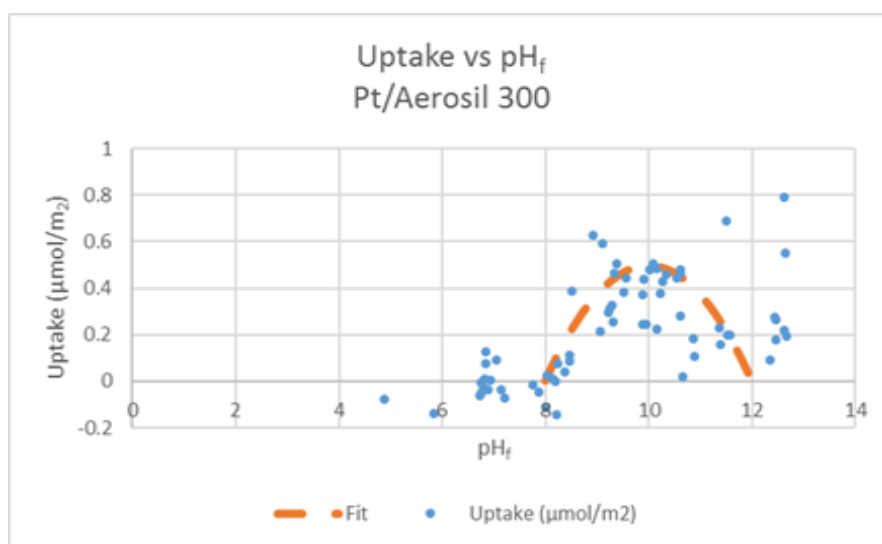


Figure 21. SEA Uptake curve for Pt/Aerosil 300. Blue dots represent experimental data, while the orange dotted line shows a quadratic trend of the bulk of the data.

A second set of nanoparticles were prepared at the same weight loading on Timrex, but using CEDI instead of SEA, so that the counterions were forced to remain in solution, is shown in Figure 21. SEA Uptake curve for Pt/Aerosil

300. Blue dots represent experimental data, while the orange dotted line shows a quadratic trend of the bulk of the data.. These are raw diffraction patterns without background subtraction, but it is clearly seen that neither pattern contains sharp peaks representative of Pt. The wide peak centered at about 38 degrees 2θ in Figure 22 for the catalyst with a $\text{Pt}:\text{NO}_3^-$ ratio of 1:0 implies the presence

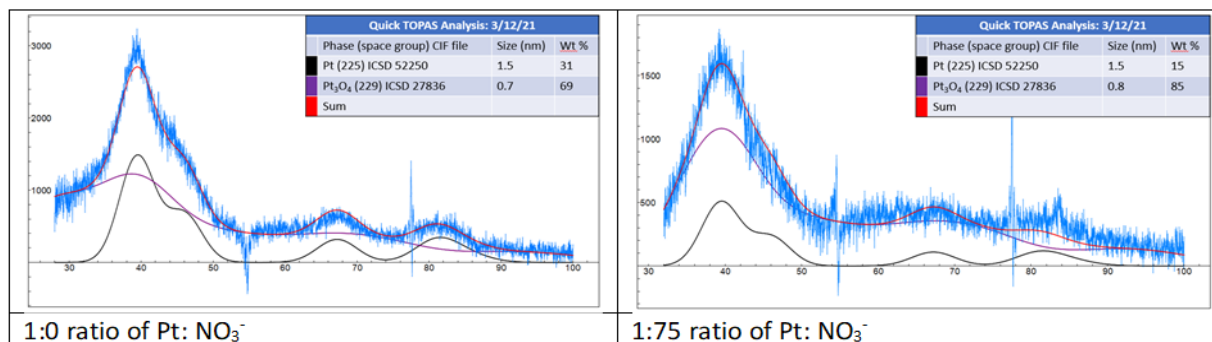


Figure 22. XRD analysis of background-subtracted Timrex-supported nanoparticles prepared with 1:0 and 1:75 ratio of $\text{Pt}:\text{NO}_3^-$

of very small Pt and Pt oxide phases, and curiously, the pattern with the high salt ratio exhibits no Pt-associated peaks at all. The XRD patterns of the final set of nitrate-derived samples by SEA over silica, with ratio of $\text{Pt}:\text{NO}_3^-$ of 1:0, 1:8 and 1:95, are shown in Figure 24. As with the carbon support, no Pt-related peaks were discernable at any of the $\text{Pt}:\text{NO}_3^-$ ratios.

Any interface arises from a balance between 1) an attraction between the molecules within each phase and 2) an attraction between the molecules between each phase. For aqueous solutions, if a solute strengthens the intermolecular forces between water molecules, usually by inserting itself constructively into the hydrogen bonding network, there will be a higher surface tension at the solid-liquid interface, and thus a weaker interaction between molecules in the liquid phase and the solid surface. The converse is true for molecules that weaken the structure of water. The former can be called “structure making,” or “kosmotropic,” while the latter can be called “structure breaking,” or “chaotropic.” A new hypothesis was thus formed: in the formation of nanoparticles from deposited metal precursors, surface tension is more important than electrostatic interaction between precursor and surface. As a corollary hypothesis: structure-making ions in solution will lead to higher surface tension of the solvent, leading to larger particles.

Previous literature has already shown that the effect of ions on the Gibbs free energy of hydrogen bonding (ΔG_{HB}) can be estimated numerically¹¹⁶. Nitrate was found to be a moderately strong structure breaker. Adding more nitrate would thus proportionally increase the attraction between support and adsorbed metal precursor, leading to smaller nanoparticles, and this could explain the lack of effect of nitrate on particle size. Carbonate, iodine, and phosphate were

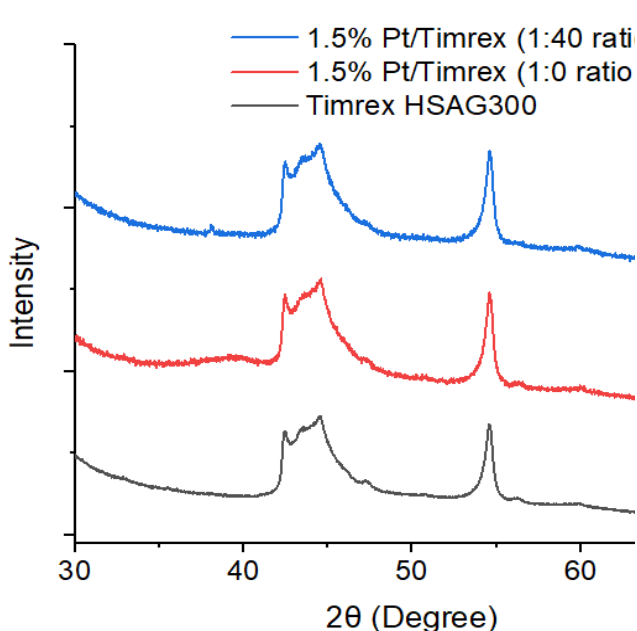


Figure 23. XRD Raw data for 1.5% Pt/Timrex HSAG300 by CEDI with 1:0 and 1:40 ratio of Pt: NO₃⁻

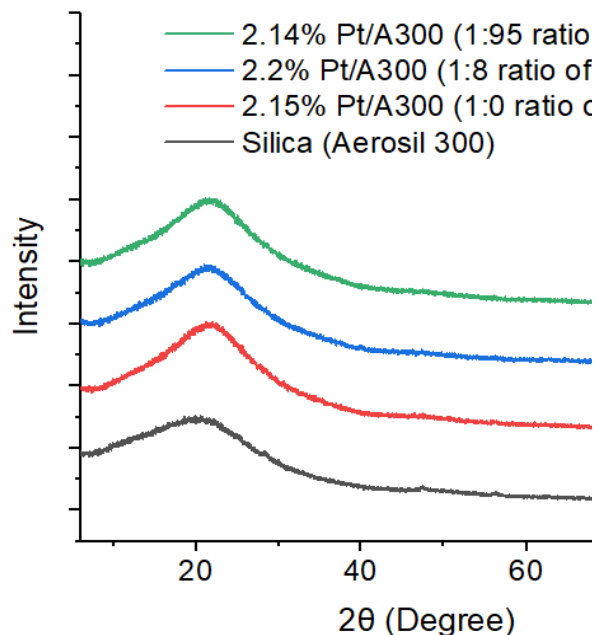


Figure 24. XRD pattern for Pt/SiO₂ by SEA at 1:0, 1:8 and 1:95 ratio of Pt: NO₃⁻

then chosen as ions that would cover the range of kosmotropes and chaotropes. To confirm the correct pH shift, especially given that carbonate and phosphate will buffer the solution, uptake experiments were performed, adding 40 mol of salt per mole of platinum. It was confirmed that the region of maximum uptake does not change for Pt/Aerosil 300, even upon addition of significant amounts of these ions, as seen in **Figure 25**. It should be noted that the cation in each salt matched the cation in the base used to basify the system (eg NaH₂PO₄ + NaOH). Additionally, ammonium phosphate will not dissolve in ammonium hydroxide above pH ~9, and thus sodium phosphate was used.

Nanoparticles were then made in ratios of 1:40 Pt/Anion with these salts. Tetraammineplatinum(II) nitrate was used in conjunction with the nitrate, phosphate, and iodide added salts, as the phosphate and iodide tetraammine platinum salts are currently unavailable as regular products in the chemical supplier marketplace. Tetraammineplatinum(II)

hydrocarbonate was used in conjunction with the carbonate added salts. The XRD results are shown in **Figure 26** for both SEA preparations and CEDI preps. It is seen that the carbonate ion had as little effect on particle size as did the nitrate effect, independent of synthesis method. On the other hand, as seen with chloride and bromide salts in previous work¹¹³, iodide does give rise to a large increase in particle size. This has been attributed to partial exchange of the ammine ligands with the halide, which gives rise to a fraction of more mobile precursors. Given the increase in particle size in concordance with the ordering in the halide series (viz. Cl \rightarrow Br \rightarrow I), halide identity appears to be a tuning parameter. To control particle size, a small amount of halide could be added to seed larger particles. Future work must be done to determine the correct proportions and to develop an experimentally viable model for this. A It also appears that the Pt peaks have broad bases, from which it can be presumed that the particle size is not narrow.

Conclusions

Particle size does not seem to be affected by increasing nitrate or carbonate concentration for SEA synthesis. CEDI produced smaller particles than SEA for Pt/Timrex, which could be due to the lowering of the surface tension of water by introducing nitrate effectively, while nitrate is less concentrated at the dried support surface via SEA. A main

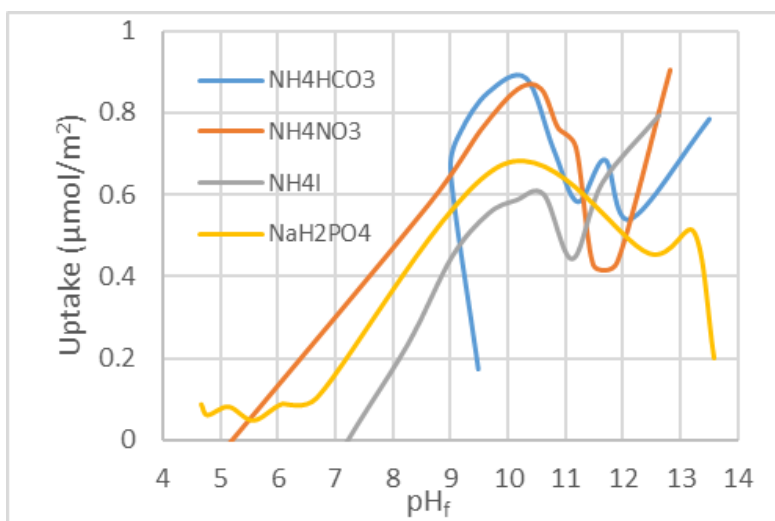


Figure 25. Pt Uptake in various dissolved salts versus final pH over Aerosil 300

takeaway from this preliminary work is that the concentration of counterions in solution, so critical for the electrostatic interaction of the dissolved precursors with the charged support surface during adsorption, is not critical in the process of dried precursors evolving into nanoparticles. In contrast, a correlation has been determined between particle size and halide value. Future work should explore the proportions needed of these halides, in conjunction with reduction conditions, to create an experimentally actionable model to tune particle size.

The preliminary conjectures on the effects of surface tension have in fact opened up a new realm of understanding in the process of drying and nanoparticle formation from adsorbed precursors, and some of these concepts are explored in the next chapter.

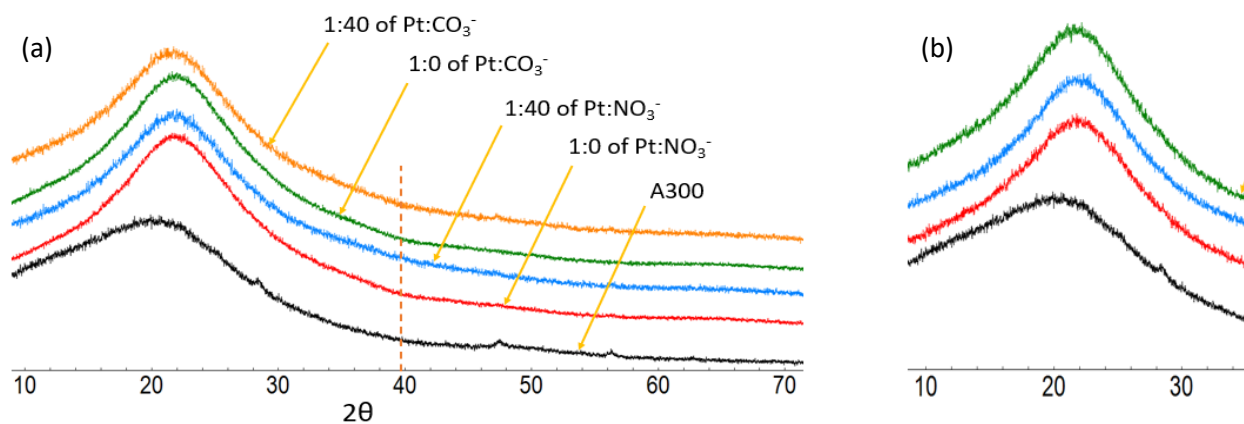
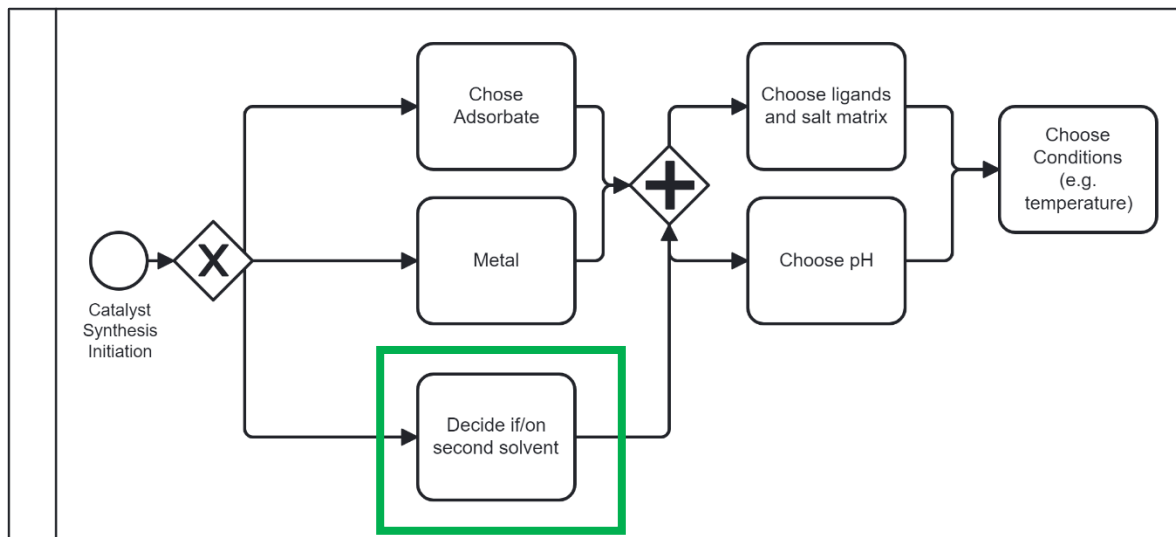


Figure 26. (a) XRD raw data for $\text{Pt(NO}_3^-)$ and $\text{Pt(HCO}_3^-)$ on A300 by SEA; (b) $\text{Pt(NO}_3^-)$, $\text{Pt(HCO}_3^-)$ and $\text{Pt(I}^-)$ on A300 by CEDI.

Chapter Four: Evaluation of Solvent Effects on Platinum Deposition using Switched Solvent Methodology



Background

Despite its success, Strong Electrostatic Adsorption (SEA) has always had an unfortunate lower limit in particle size below 1nm. Abolfazi Shakouri hypothesized that this was an effect of water properties. Water is an excellent solvent because the attractive force between ionic species is an inverse function of the dielectric constant of the medium between them. Water has an exceptional dielectric constant, and thus has significant solubilizing powers and why it has been called the “universal solvent.” However, water also has a surface tension.¹¹⁷

As discussed in Chapter One:, water will agglomerate on the surface, likely into nanodroplets centering on the surface hydroxyls, especially once the rest of the surface has dried. If the affinity by the adsorbed metal complex for the droplet is greater than the affinity for the surface, then as the droplet dries and the boundary reaches a metal atom, it may detach from the surface, and move with the droplet perimeter. Once saturated, the metal in each droplet may agglomerate and form particles or clusters that may grow under reductive conditions. Thus, the final particle size would be a function of the nanodroplet size. As water has a high dipole moment, its starting droplet size is likely large.¹¹⁷

SEA leads to smaller particle sizes in part because the charging of the surface can lower droplet size by decreasing the interfacial tension. However, this can only accommodate so much. It may naturally be asked, then, how the surface tension could be lowered to test this effect, without losing the solubilizing power of water. Shakouri's solution was to perform an initial aqueous wet impregnation, followed by an acetone addition. The acetone, being miscible with water, but also having a higher dipole moment than water would allow it to infiltrate the pores, and displace water from the solvation sheath, thereby minimize the nano-droplet size and thus decreasing the final particle size. This method was called Switched Solvent Synthesis (SwiSS).¹¹⁷

There is little in the literature on similar methods. As we stated in our previous paper,¹¹⁸ perhaps the closest study in the literature to SwiSS is a work in which solvents of decreasing polarity are employed in an effort to atomically disperse carbon supported gold and other noble metals.¹¹⁹ Solvents of decreasing polarity and decreasing boiling point resulted in lower agglomeration of the precursors and the lowest polarity solvents such as acetone yielded isolated metal sites. No solvent switch was employed; metal precursors must be used which are soluble in the particular solvent employed. Solvents were kept free of water and interestingly, when syntheses with mixtures of acetone and water were attempted, higher fractions of water yielded larger particles.

Another group¹²⁰ has used short chain alcohols to decrease activated carbon supported zinc nanoparticle size from > 30 nm, where water was the sole solvent, to < 16 nm by adjusting the proportions of alcohols in the solvent mixture. This effect was attributed to the increased ability of the alcohols to wet the non-polar activated carbon surface, leading to better infiltration of the pore network and a higher metal dispersion. However, more significant lowering of polarity caused increased particle size, attributed to decreased solubility of the metal salt at polarities significantly lower than that of water, leading to agglomeration in solution.¹¹⁸

Because the two papers attribute the effect of the solvent to different causes than Shakouri does, there are now multiple possible causes of the effect of lower particle size. Because of the novelty of SwiSS, in this study, full verification of the theories proposed is not attempted, though these are currently in progress. Rather, an understanding of the relative importance of each step in the synthesis was the goal. This will be achieved by varying

process parameters in the Swiss-type impregnation, as well as testing the effect of other solvents, using chloroplatinic acid adsorbing to a vulcanized, low sulfur support as a model system.

Experimental

Materials

The support used was a Carbon Black – Vulcan XC 72, hereafter called VXC-72, purchased from FuelCellStore (SKU: 16080004). While these came in pellet form, they are weakly held together and collapse into a powder upon wetting. No pre-treatment was done on the support before experiments. N₂ physisorption isotherms were performed using an ASAP 2020 Plus unit by Micromeritics and analyzed by using the ASAP 2020 software. The BET model was used to determine the surface area. Pore size distribution was determined using Non-Local Density Functional Theory (NLDFT) on two separate measurements. The values for these are given in *Table 9*. Plots of the NLDFT micro- (<2), meso- (2-50nm), and macro- (>50nm) pores are given in Figure 27 and Figure 28.

Table 9. Surface Properties of VXC-72.

Parameter	Value	Source
Primary Particle Size (PPS) ¹²¹	30-60 nm	Literature
Specific Surface Area (SSA)	230.31 m ² /g	Experiment
Cumulative Pore Area (<100nm pores)	47.8 cm ³ /g	Experiment
Cumulative Pore Volume (<100nm pores)	0.177 cm ³ /g	Experiment

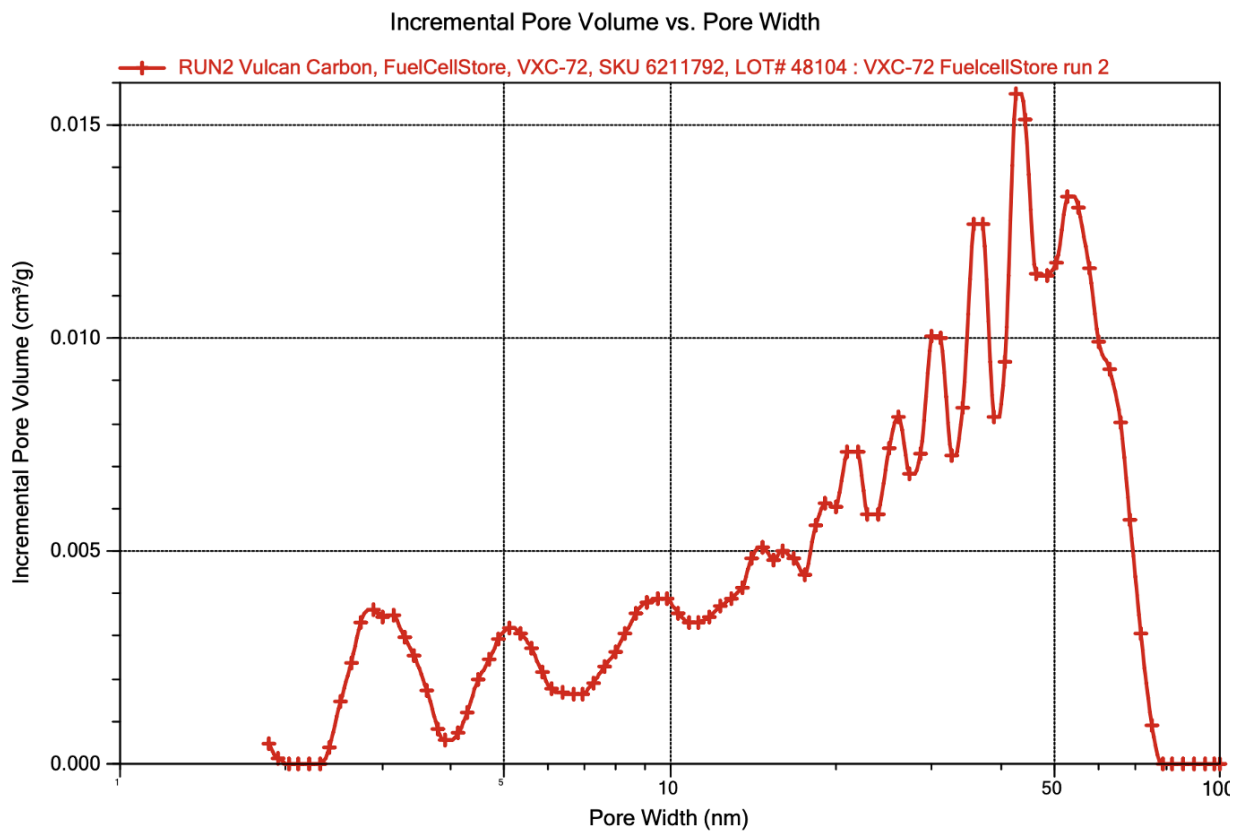


Figure 27. Incremental Pore Volume vs Pore width of VXC-72.

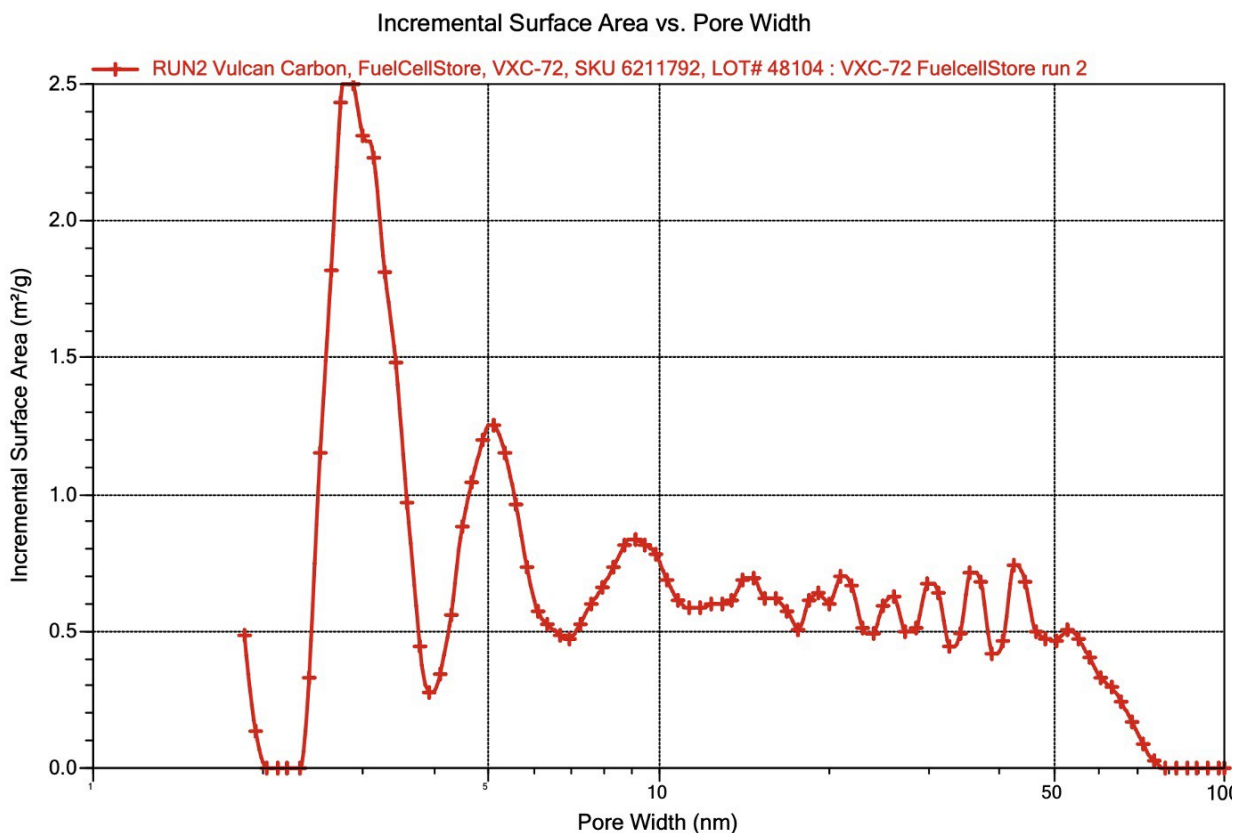


Figure 28. Incremental Surface Area vs Pore Width for VXC-72

Chloroplatinic (IV) acid (H_2PtCl_6) precursor salt was obtained from VWR ($H_2PtCl_6 \cdot (H_2O)_6$, 99.9%, SKU: BT136200), and Fisher Scientific ($H_2PtCl_6 \cdot (H_2O)_x$, 99.9%, SKU: AA1105103). Multiple stock solutions of Platinum were made with a concentration range of 15k-117k ppm and *pH* range of 0.27-0.98. The samples were made by diluting the stock solutions with water to the desired concentration, with a concentration range of 2.6k-22.9k ppm and *pH* range of 0.83-1.7.

Concentrations were confirmed by an Agilent ICP-OES unit. A platinum ICP standard with a 5% HNO_3 matrix from VWR (SKU: BDH82026-038) was used to make an 8 point (including blank) platinum calibration series from 0.3ppm to 300ppm by serial dilution with 5 the same 5% HNO_3 matrix. The samples were diluted first with a small amount of 70% HNO_3 , followed by slow addition of nano-pure water in proportions such that the final HNO_3 concentration would be around 5%, and the platinum

concentration would be around 30ppm. All dilutions for samples and calibration standards were weighed at each addition step in order to ensure accuracy in the calculations, avoiding possible sampling errors associated with pipetting due to surface tension and density changes in the extreme pH regions. ICP-OES determined concentrations were calculated by using a multi-wavelength calibration, taking radial and axial measurement of the most intense wavelengths that don't overlap, and averaging all that had an $R^2 > 0.9999$.

For aqueous solutions, nanopure ($>18.18\text{M}\Omega\cdot\text{cm}$) water was obtained from an in-house Milli-Q Ultrapure Water Filtration System. Solutions were made by simple mixing and vortexing of appropriate amounts of salt and water together. These would be added to the VXC-72 powder, mixed and then organic solvents would be added and the procedure repeated. The standard amount of Pt-solution added to carbon was 465 Organic solvents used were acetone (Fischer, $\geq 99.5\%$), Acetonitrile (Sigma-Aldrich, 99.8%, anhydrous), 1,4-Dimethylpiperazine (Apollo Scientific, 98%), 2-Ethoxyethanol (TCI America, $\geq 99.0\%$), 4-picoline (Thermo Scientific Chemicals, 99%), Morpholine (BeanTown Chemical, $\geq 99\%$), 4-Methylmorpholine (MilliporeSigma, $\geq 98\%$), Cyclopentanone (TCI America, $\geq 99.0\%$), Methyl Formate (TCI America, $\geq 98.0\%$), Pentan-1-ol (TCI America, $\geq 99.0\%$), DL-2-Pentanol (Thermo Scientific Chemicals, 98%).

In order to have total consistency across experiments, great care was taken to have every experiment comparable. To do this, a full procedure, along with discussions of sources of error, mitigation procedures, and what to watch for in the Gupton lab specifically is as follows:

Experimental Preparation

The PTFE boats (see Appendix A: for 2D projections of designs for boats and holder) were cleaned with Gojo or similar cleaner, as regular Alkonox soap doesn't work as well. PTFE typically yields an unstable reading on precise scales, and will slowly drift, which Mettler Toledo attributes to tribocharging,¹²² a charging mechanism where electrons are transferred across an interface to create equally and oppositely

charged surfaces. This leads to an electrostatic force being superimposed on the gravitational force of the PTFE on the scale, and can change the measured weight.¹²³ To mitigate this, the mass was measured in conjunction with a Zerostat 3 antistatic gun. An informal poll was conducted by the author, who found that from more than 10 people across two universities and multiple labs, only one person knew how to use an antistatic gun. A common response was to hold the gun close to the surface, and squeeze multiple times in quick succession. For the benefit of the reader, the correct procedure from the manuals of antistatic guns expressly say: The gun must be held around a foot from the target surface. The trigger must be squeezed slowly for two seconds, releasing positive ions, followed by a slow release over two seconds of the trigger to release negative ions.¹²⁴ Some manuals add a 2 second hold step between compression and release of the trigger. Finally, these ions are made from molecules in the lab air, such as acetone, that pass near to a piezo-electric crystal that ionizes them.¹²⁵ To measure the mass, the boats were turned on their end to minimize contact with the balance surface, and then the gun was used as stated earlier on all angles of the boat, and the stabilized reading was used.

All support powders were pre-weighed on a low precision balance. Then using a high precision ($\pm 10\mu g$) balance, the mixing containers (2-50mL polypropylene centrifuge tubes with cap) were weighed. Then followed the pre-weighed support powders were added to their respective mixing containers and weighed.

Procedure of mixing

Early experiments seemed very sensitive to many different conditions. This may be because of complex interactions between pore infiltration, drying, etc. Because of this, addition weights and step times were checked and kept track of. The general procedure shown in Figure 29 involves a sequence of additions of material, mixing, and checking of conditions. To keep track of times between steps in the mixing process,

use of a stopwatch (the author found the Multi-Timer StopWatch app to be the best app for this⁵) was critical. In each use of Start or Lap , the start or lap buttons were pressed so that both the overall and step times could be kept track of. “Cap” refers to the cap on the mixing container. The mixer that was used was either a Scientific Industries, Inc. Vortex Genie 2 or a Resodyne Lab Ram I. It was found that different lab members would hold the tubes at very different levels of firmness on the Vortex Genie. In some cases, the contents would not be finished mixing. To minimize this effect, a vertical Adapter head by Stellar Scientific (SKU: SI-V525) to hold the tubes was used to hold the tubes on the Vortex Genie while mixing. The Lab Ram had such a feature built in. To measure relative humidity, a Temperature and Humidity USB-PDF Datalogger by Triplet Test Equipment & Tools (SKU: RHDL30) was used. A glass thermometer was used to measure furnace temperatures below 50°C where indicated. Shakouri had previously hypothesized that surface tension driven spontaneous transport increased quality of mixing, thereby decreasing particle size.¹¹⁷ Some have called this Marangoni Flow, though others have objected to this use and prefer the term Benard Flow.¹²⁶ Because of this, an attempt was made at keeping track of the “thickness” of the slurry, the level of settling by the support, and the degree of spontaneous convection once poured. These were measured by visual inspection and rated on qualitative, empirical scales.

The thickness of the slurry was measured by its ability to flow once the tube was turned upside down over the boat with the following 1-7 point scale: 1) No flow out of the tube, requiring scraping of the slurry with a spatula, 3) no immediate flow, but manual tapping of the tube end forced the slurry to drop out, 5) most of the slurry would pour out, but would require some small degree of manual tapping to get the final portion out, 7) the “slurry” had an apparent viscosity similar to water, and would flow freely out, leaving only a slight residue.

⁵ Android: https://play.google.com/store/apps/details?id=com.jee.timer&hl=en_US&gl=US

The settling of the wetted substrate was measured by visual inspection of the slurry, having been poured into the PTFE boats, according to the 1-5 point scale: 1) No settling, substrate stays completely suspended, 3) Substrate slightly settles up to thin layer of supernatant, 5) Substrate settles fully to the bottom of boat with minimal suspension.

Finally, the degree of spontaneous convection of the wetted substrate was also measured by visual inspection, having been poured into the PTFE boats, according to the 1-5 point scale: 1) No observable flow. This could include fully suspended solutions where none could be seen even if it were happening, 2) Patches of sporadically circulating substrate, 3) Entire boat wall was lined with circulating substrate.

Action				Stopwatch
Open cap				→ Start <input type="checkbox"/>
Pipette aqueous metal solution onto support powder				→ Lap <input type="checkbox"/>
Close cap				→ Lap <input type="checkbox"/>
Place on mixer, Start mixer				→ Lap <input type="checkbox"/>
Stop mixer				→ Lap <input type="checkbox"/>
Weigh	→		Open cap	→ Lap <input type="checkbox"/>
Pipette organic solvent onto slurry				→ Lap <input type="checkbox"/>
Close Cap				→ Lap <input type="checkbox"/>
Place on mixer, Start mixer				→ Lap <input type="checkbox"/>
Stop mixer				→ Lap <input type="checkbox"/>
Weigh	→		Open Cap	→ Lap <input type="checkbox"/>
Note the Relative humidity (%) and Room temperature (C) using the gray sensor	→	Pour/scrape into boat	→ If pourable: Recap and weigh immediately then store in hood for a day or more to dry (then reweigh and note time and date)	→
Note the flowability (1-7), settling at about 2min (1-5), and spontaneous mixing at about 2min (1-5)	→	Note reading of thermometer in tube for accurate tube temp measurement	→ Carefully place boat into furnace and close the door as described in the earlier section at intended time	→
Turn on gas flow				→ Lap <input type="checkbox"/>
Press start on furnace	→	Note the time and date of turning on the H2 gas	→ Note relative humidity levels and	

Figure 29. Procedure for keeping track of changes during mixing in SwiSS.

Furnace Reduction

The treatment runs were performed in a 4 chambered horizontal tube furnace with alumina tubes (25OD x 22ID x 460L, mm), from MTI (SKU: GSL-1700X-MGI-4), custom fitted with alumina jacketed type B thermocouples fitted inside the tube, rather than in contact with it, as well as another alumina insulator fitted to the other side of the tube. The samples were all put under a flow of 10 vol% H₂/Ar at 200sccm (8.77mm/s, about 52.5s to completely displace gas in the tube). Most experiments involved an initial soak at room temperature or ramp at 2°/min to 60°C and hold for 30min unless otherwise noted. It should also be noted that due to the furnace having Pt/Rh type B thermocouples, which has a non-unique temperature-voltage function from 0 to 42°C, the furnace does not read lower than 50°. This means that there is likely an unmeasured spike in energy input at the beginning of the ramp, as the feedback to the furnace reads energy input with no temperature change below 50°C. The furnace would then be ramped at 2°/min to 170°C, and be held for 1 hr. After this, the sample would be cooled ambiently, as the furnace had no active cooling; however, the furnace would not allow a ramp down faster than 10°/min. The ramp and soak diagram is shown in Figure 30.

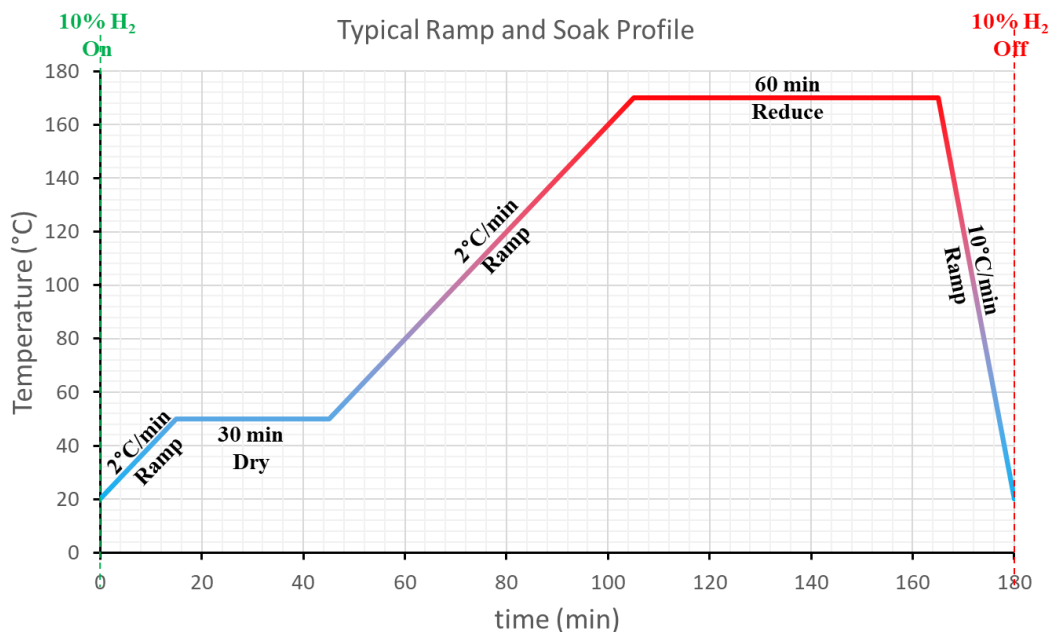


Figure 30. Example ramp and soak profile. Here is shown a ramp to 60°C, though many experiments performed the drying at room temperature.

Once the furnace had reached a temperature of below 80°C, the sample was removed and exhibited the fracture pattern of a desiccated soil. This was collected into a 2mL polypropylene centrifuge tube, weighed and taken to XRD for particle analysis. An image sequence of how the sample looks at each stage in the process is shown in Figure 31.

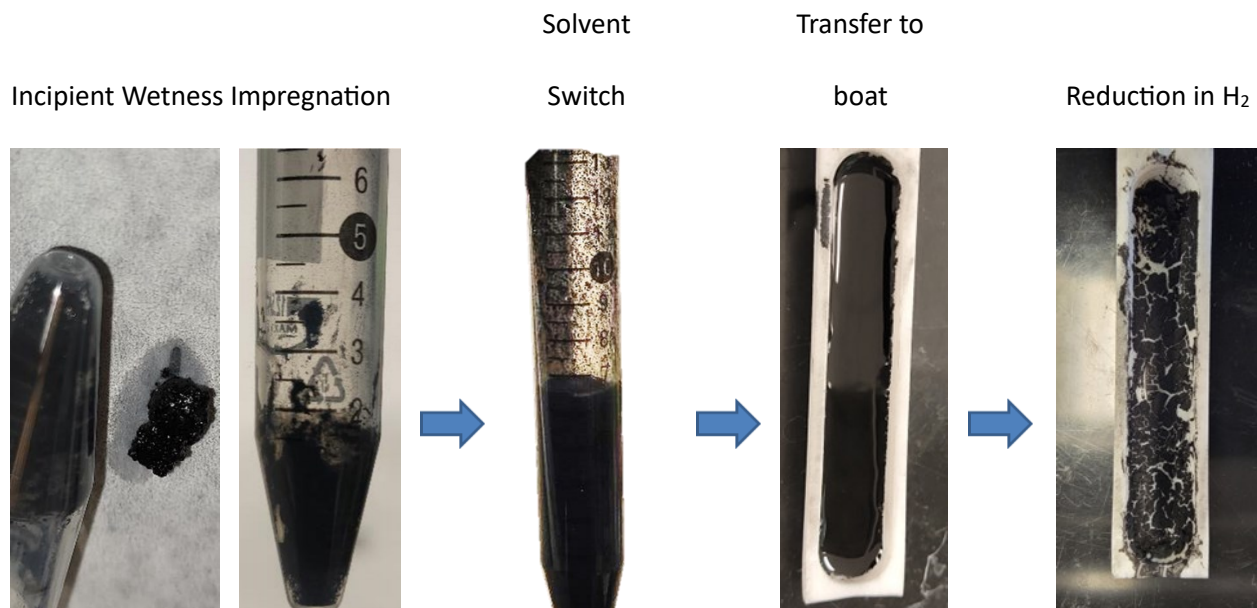


Figure 31. A visual progression through the steps of SwiSS.

XRD Analysis

The XRD measurements were performed using the Empyrean by Malvern Panalytical with a 255x255 pixel PIXcel3D detector. Samples were mildly ground using a spatula, and gently scattered across the surface of a zero-background holder (Product Code: 943001817321) made by cutting pure silicon at a high lattice angle to minimize the background contribution from the sample holder. The holder was cleaned in between each measurement with EtOH, and weighed before the addition of carbon, as well as after the scan to determine the mass of carbon added to the scan. The scan was performed using

Bragg-Barento geometry, from 10-90° 2 θ , with a step size of 0.053° 2 θ , and the sample stage spinning at a constant rate of 2rev/s, in order to limit the effect of preferred orientation. Instrument conditions are included in Table 10.

Table 10. XRD conditions for all samples collected analyzed

Scan Conditions					
Scan Range 2 θ (°)	10-90	Step Size 2 θ (°)	0.05252	Common Counting Time (s)	227.205
Spinner Revolution (rev/s)	0.5				
X-ray Conditions					
X-ray Tube Current (mA)	40	X-ray Tube Tension (mA)	45	Pulse Height Distribution Range (%)	25-80
Incident Beam					
Goniometer Radius (mm)	240	X-ray Acceptance Angle (deg)	0.8	X-ray Mirror Length (mm)	55.3
Soller Slit Opening (rad)	0.03	Mask 1 Distance to Sample	171.5	IBP – Mask 1 Distance to Sample	111
IBP – Mask 1 Width (mm)	14	IBP – Mask 2 Width (mm)	14	IBP – Divergence Slit Distance to Sample (mm)	99.5
IBP – Fixed Divergence Slit Angle (°)	0.63				
Divergent Beam					
DBP – Radius (mm)	240	DBP – Anti-scatter Slit Angle (°)	4	DBP – Soller Slit Opening (rad)	0.04

Results and Discussion

The lion share of experiments were performed with acetone, and this is the solvent that the variety of process parameters were studied under. Until the section that specifically addresses the different solvents, if it is not clear, the solvent being used is acetone. In addition, the particle size will be approximated by the apparent size of the associated peak, such as the Pt(111) peak at ~39.8° 2 θ .

Tube Size and Mixing Parameters

Early tests showed that certain process variables often completely overlooked by researchers as variables were found to have some effect on the final particle size. One of these seemingly innocuous parameters was the size of the tube that the mixing was done in. In general, as not all particles will always hit the wall at every oscillation during mixing, larger tubes can lead to fewer impacts per solution particle per unit time. An observation that was made during these experiments was that a significant portion of the slurry in a 50mL tube would move vertically rather than horizontally and never even hit a surface before the next oscillation. Conversely, small containers, such as a 2mL, appeared to limit any sort of internal bulk motion of the slurry. Both of these could inhibit mixing, leading to possible inhomogeneities in the final slurry.

As a precedent in literature, Faure, et al.¹²⁷ found that the factor of primary importance was the same level of wet mass consistency between granulation experiments of identical conditions. They also showed that geometry differences between mixers was critical, even mixers in the same line of products from the same company. In a sort of inverse problem, Landin, et al.¹²⁸ showed that within the same

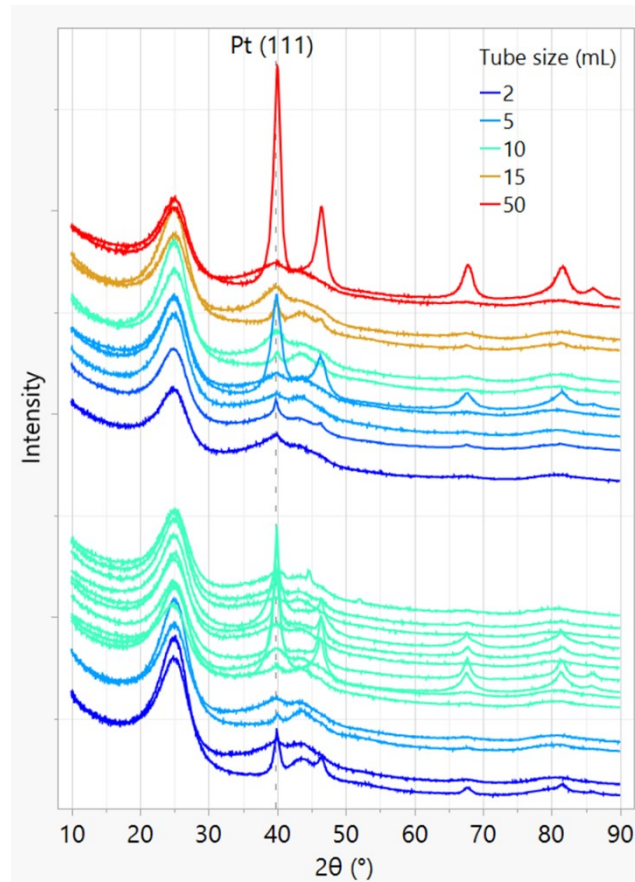


Figure 32. Pt/VXC-72 XRD diffractograms: variation of tube size. Upper block involved a vortex mixer, while the lower block is involved a Resodyne. Then, the subdivisions within each block are by color, representing each mixing tube size, as indicated by the legend

geometry, batch size can have an effect on the granulation process. Even if batch sizes are similar, their relative difference to different containers, even geometrically similar ones, may lead to final mixing qualities.

As a first test, Figure 32 shows the XRD diffractograms of a series of Pt/VXC-72 catalysts, synthesized with acetone, with a variety of platinum weight loadings (4.1-7.1%), acetone-to-water ratios (2.2:1 – 4.3:1 mol:mol) shaking times (12-603s), accelerations by the Resodyne (30-50G), and time between pouring into the boat and loading into the furnace (viz, acetone evaporation) (49-161s). As a note, the resodyne cannot accommodate the height of the 15mL or 50mL tubes, and so those tube size-mixing type combinations were not included.

Unfortunately, there is a lot of noise in the effect of tube size on crystallite size. Even within the same

tube size and mixing type, such as for the data rich category of 10mL-Resodyne (teal, bottom block), or for the more sparse categories of 50/5mL-vortex (red/light blue, top block) combinations, there is wide variation. This may

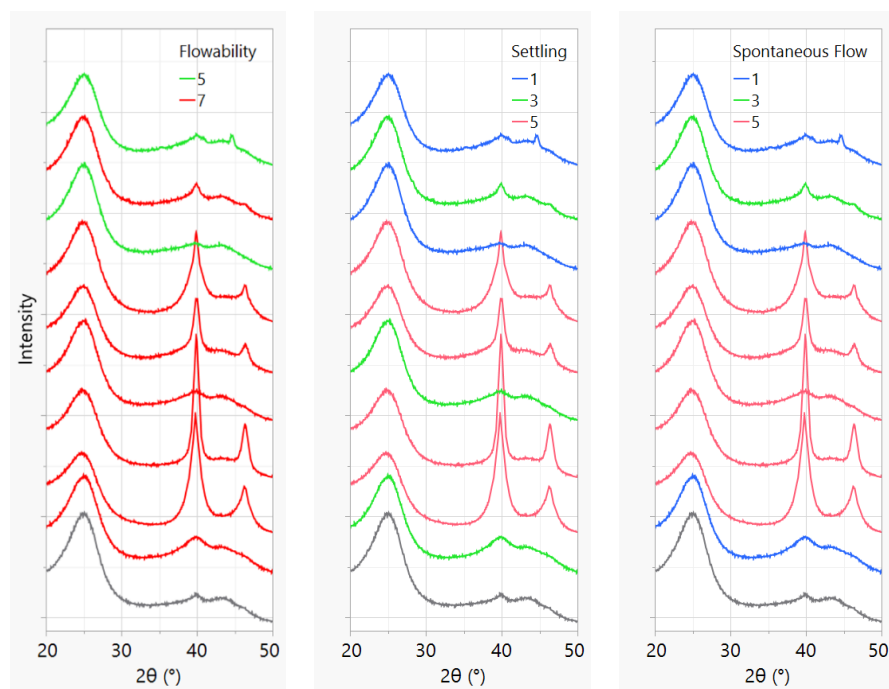


Figure 33. The effect of the three empirical parameters "Flowability," Level of Settling, and Level of Spontaneous Convection on Pt(111) peak. The legends that are shown give the color-level pairing.

be attributable to the wide variation in other process parameters.

However, when one zero's in on the 10mL-Resodyne subset, a trend does emerge.

Figure 33 shows the three empirical parameters of “Flowability,” Settling, and Spontaneous Flow described earlier (see Chapter Four: Procedure of mixing). Flowability and Spontaneous Flow show a rather weak correlation with crystallite size. However, the settling of the powder trends very strongly with particle size, even across such a wide crystallite size distribution. By the Scherrer equation, the largest crystallite is around 11.5nm, while the smallest is significantly below 1nm, possibly around 0.6. It should be stated however, that the Scherrer equation loses its validity in the sub-nm range.

A high level of settling (red) always shows very large particles, while less settling shows significantly smaller particles, possibly an order of magnitude smaller, though there are some seemingly bi-modal particle size distributions. This is a very large correlation, especially given the wide variation in other process parameters. In fact, there is an interaction between flowability and settling, where large particles are only found in both high levels of settling are only found in high levels of flowability.

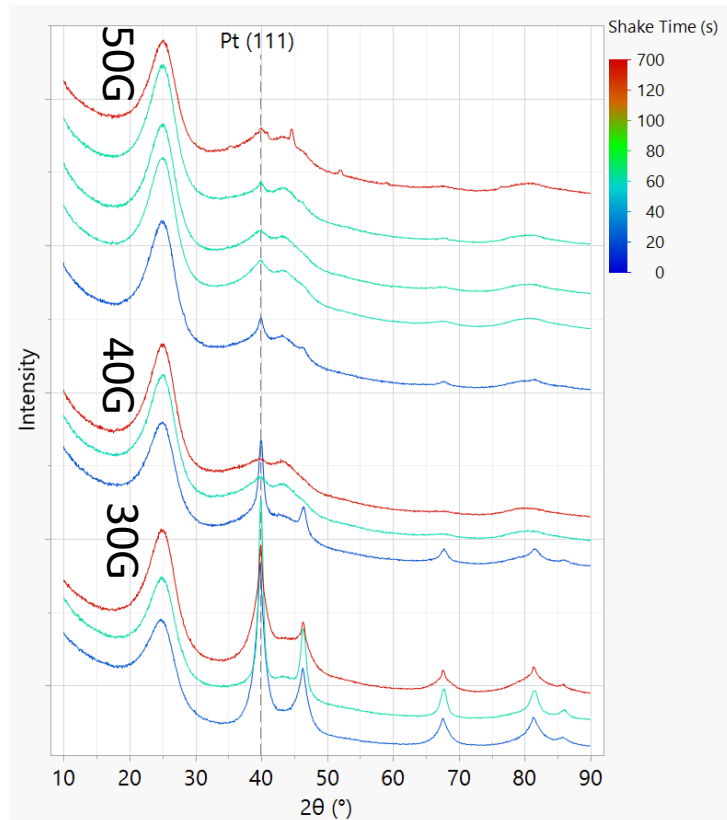


Figure 34. Pt/VXC-72 XRD diffractograms: Variations of

When plotting this 10mL-Resodyne subset parameterized against shake time and shake intensity, a similar trend to that of the settling occurs. In Figure 34, the 10mL-Resodyne is grouped vertically by intensity of mixing (50G, 40G, and 30G, where G is the acceleration due to earth’s gravity). This range was chosen because there was no mixing

below 30G, while above 50G, the polypropylene tube began to deform. As can be seen, all of the low acceleration samples have large crystallites, while all of the high intensity shaken samples have predominantly smaller particles. A similar trend is observed with the duration of shaking, and there appears to be an interaction between the two.

This strong interaction could be explained by a few things. First, upon mixing with the aqueous solution, a thick paste is formed, as seen in Figure 31. The mixing with the acetone is then required to break it up. There first must be enough acetone to conceivably break it up, which this dataset has (>3.5mL acetone/150mg VXC-72). However, a certain energy barrier must be overcome to completely break up the agglomerations. Simply energy input alone to break up agglomerants may be the driving force of these effects. This can also be compared with the results in Figure 35 where the high levels settling only occur for the low energy input end (low shake time, low mixing speed). In fact, this effect may be a force against flocculation. However, flocculation in the context of organic solvents is more complex due to the nature of the double layer in non-aqueous environments.¹²⁹ This will need to be the focus of future studies.

Effect of Drying

In the process of SwiSS, once the mixing is done, the sample is poured into a boat (see Chapter Four: Procedure of mixing). This is an opportunity for some degree of drying, as acetone has nearly 100 times the vapor pressure of water at room temperature. In order to test this effect Effect of Drying.

In the process of SwiSS, once the mixing is done, the sample is poured into a boat (see Chapter Four: Procedure of mixing). This is an opportunity for some degree of drying, as acetone has nearly 100 times the vapor pressure of water at room temperature. This was also seen in prior experiments, such as in Sun, et al., that showed drying was an important process parameter in controlling the agglomeration of nanoparticles. This is a vast experimental space, so in the service of practicality, this study was limited

simply to drying time, which would lead to varying levels of solvent remaining in the system at the point of beginning thermal treatment. In order to test this effect almost 20 experiments were conducted, as shown in Figure 36, with relatively similar treatments: weight loading (3.6-4.6%), acetone:water (2.9-3.9 mol:mol), and shake time (59-61s).

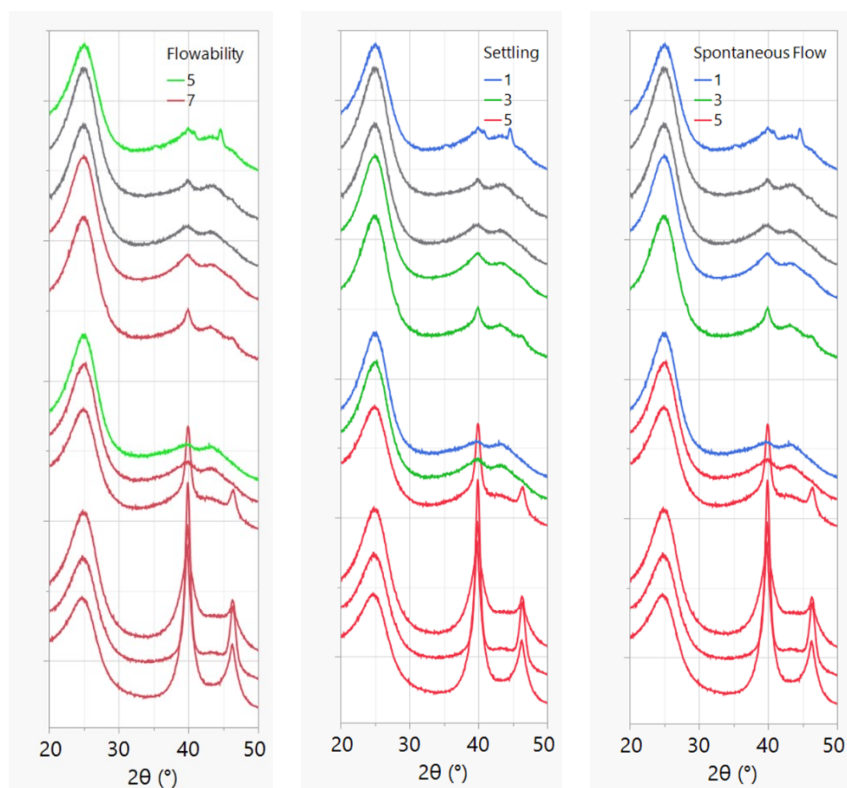


Figure 35. The effect of the three empirical parameters "Flowability," Level of Settling, and Level of Spontaneous Convection on Pt(111) peak grouped by intensity of shaking (bottom group=30G, middle group=40G, top group=50G). The legends that are shown give the color-level pairing.

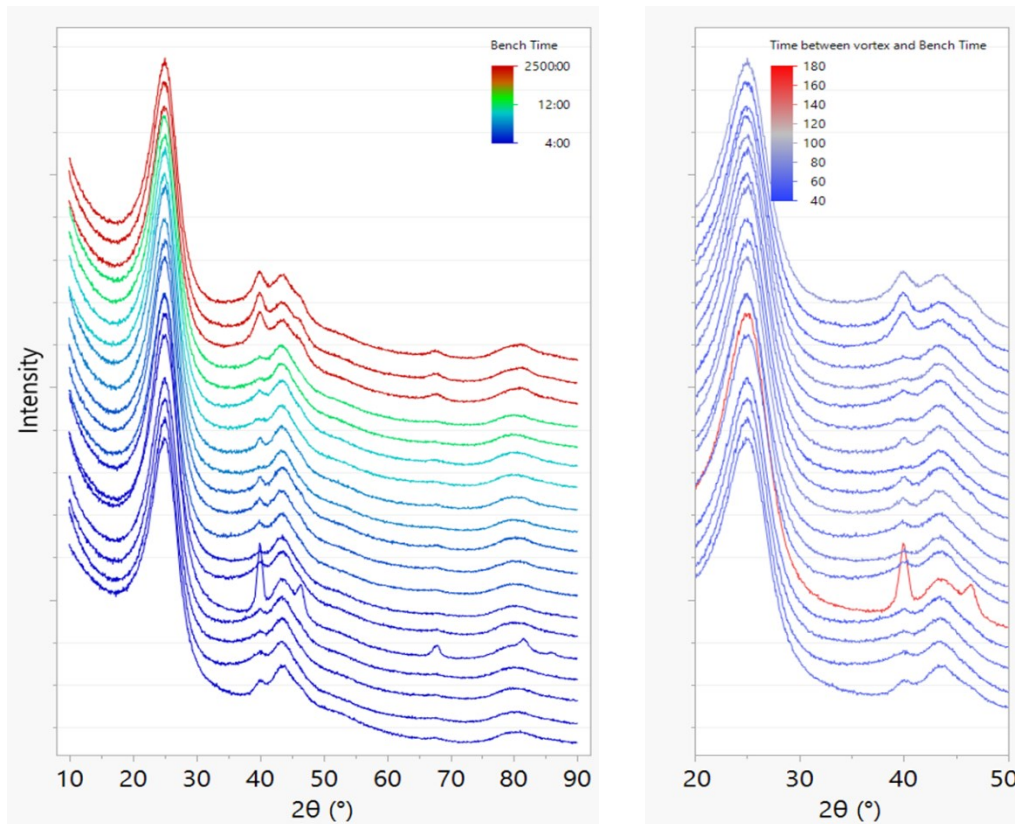


Figure 36. Variation of XRD diffractogram from 1:30m to 40h of time between opening the cap to pour the slurry into the boat, and turning on the H₂-flow to the sealed furnace. The left shows the dataset against that time, while the right recolors as a function of time between mixing and bringing to the bench.

The left of Figure 36 shows the trend of crystallite size from low amounts of time exposed to air, to high amounts of time (1:30m – 40h). The general trend is that if you keep every other parameter relatively constant, the time on the bench does not seem to have much of an effect. There does seem to be a slight, reproducible effect at 40h, but this is such a long period, it doesn't seem significant for the purposes of creating smaller particles. From these results, time on the bench appears to be a process parameter that can be ruled out. This is interesting, as longer times should lead to more settling, and thus larger particles. However, there is another interesting detail. One diffractogram (bench time=2:33m)

has significant particle growth. On the right side plot, the dataset is colored against the amount of time the sample sat in the sealed tube before being poured into the boat. This is the only variable in our database that segments the data such that that diffractogram is singled out. While this could be a coincidence, the physical connection here may be that there was time to settle out in the tube before being poured. Unfortunately, this sample was made before the accounting of the three empirical parameters of flowability, settling, and spontaneous flow were begun to be measured. More experiments will be needed to determine the reproducibility of this result.

The Effect of Drying Temperature and the Ratio of Acetone to Water

The bulk of the work done in prior studies had been on the ratio of acetone to water, and this section furthers that work. Figure 37-Figure 42 shows a series of SwiSS experiments at a wide range of acetone-to-water ratios, under various drying conditions. All catalysts are roughly 4% Pt.

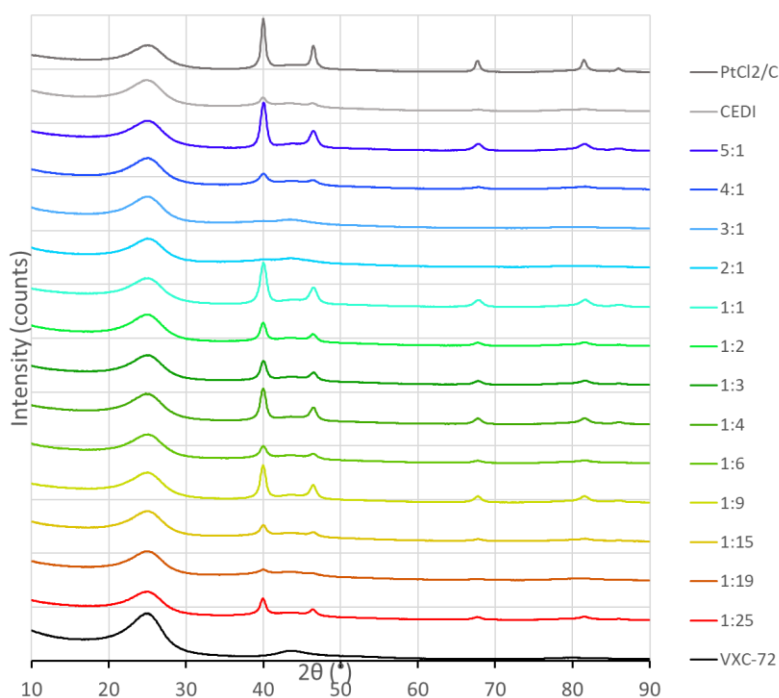


Figure 37. Effect of the molar ratio of acetone to water, while drying at room temperature under 10% H_2 /Ar for 30 mins before ramping to 170°C.

Figure 37 shows a series of catalysts that saw molar ratios of 5:1 down to 1:25 acetone-to-water, and were pre-dried at room temperature. The ratios seem to yield a rather random distribution of crystallite size. Experiments prior to this study had dried at 40°C, and tested only ratios of 4:1, 1:1, and 1:4, settling on a ratio of 4:1 as optimal. When drying at room

temperature, 4:1 yields small, but not the smallest particles. Considering only high ratios, around 2-3:1 is much more optimal. At lower ratios, the optimal value is difficult to say. 1:1 and 1:4 certainly yield larger particles. However, 1:19 yields almost as small particles as 2-3:1. The effect in this region is not clear, and because of the difficulties already discussed regarding homogeneity of mixing, it was decided not to continue in this region of low liquid loading.

Figure 38 shows a second series of experiments, zeroing-in on that region of moderate to high acetone loading, about a 1:2.75 to 5:1 molar ratio to water. Aside from a quick drop off in the 1:2.75 region, which does not cohere with the results from Figure 37, the parabolic shape of the effect seen in the first dataset remains, albeit in a much-flattened form. Similar experiments were conducted with ramping at 2°C/min to elevated drying temperatures of 60°C (Figure 39), 90°C (Figure 40), and 120°C (Figure 41), which are just above the boiling point of acetone, just below the boiling point of water, and just above the boiling point of water, respectively. Interestingly, the lower bound of the particle sizes does not seem to decrease. Whatever the effect of acetone is, it seems to have either completed its work by the end of the drying process, or acetone has an abnormally strong binding to the surface and remains past the drying process. Figure 42 shows a summary of the trends of the acetone-to-water molar ratio across the different temperatures by plotting the intensity of the Pt(111) peak against the solvent ratio. Below the boiling point of water, the minimum particle size clearly goes down. Once above the boiling point of water, the slope of the downward trend shifts to the high solvent ratios.

Also interesting of note is the comparison between the two 20 degree series. The lower ratios of first series (see Figure 37) has been cut off for clarity, as there was no discernible trend. Upon comparison with the narrower series of experiments, the plateau is consistently wider. Thus there must be some source of variation as yet unexplained, either in the effect of the solvent, or some process parameter that was missed during the planning of these experiments.

The drying however, has a significant effect. However, it is not clear whether the effect is due to the change in vapor pressure and subsequent rate of change in the proportion of the solvents, or the rate of exiting pores and desolvating the surface and metal or some other effect. Another option to consider is a direct effect of temperature dependent macroscopic properties of the solvents, such as changing surface tension, dielectric constant, or even some exotic process, such as an azeotrope between acetone and water at high pressures that could be created within confined spaces such as macropores. These questions cannot be answered by this data. However, further studies are already being conducted into addressing these questions.

XRD
4wt% - Drying at RT
A:W variation

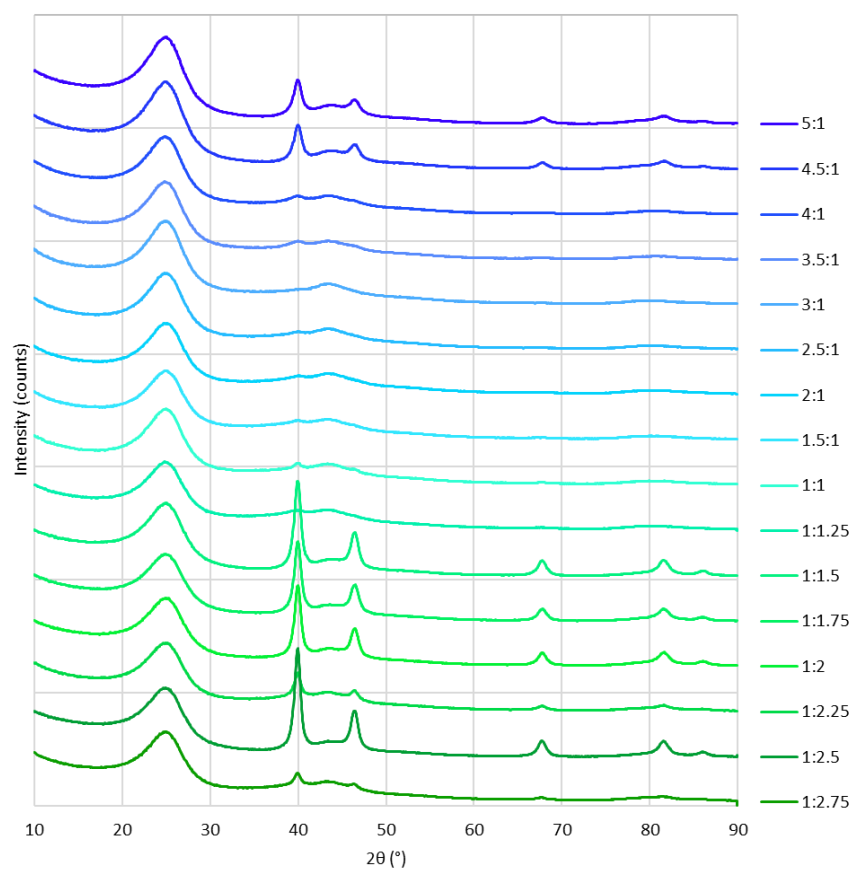


Figure 38. Effect of the molar ratio of acetone to water over a narrow region, while drying under 10% H_2 /Ar for 30 mins before ramping to 170°C.

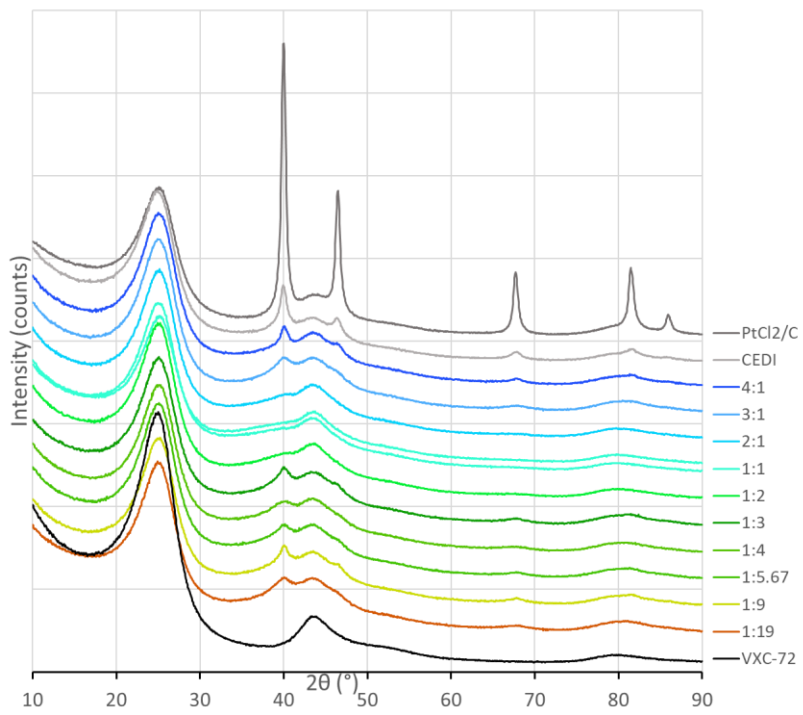


Figure 39. Effect of the molar ratio of acetone to water, while drying at 60°C under 10%H₂/Ar for 30 mins before ramping to 170°C.

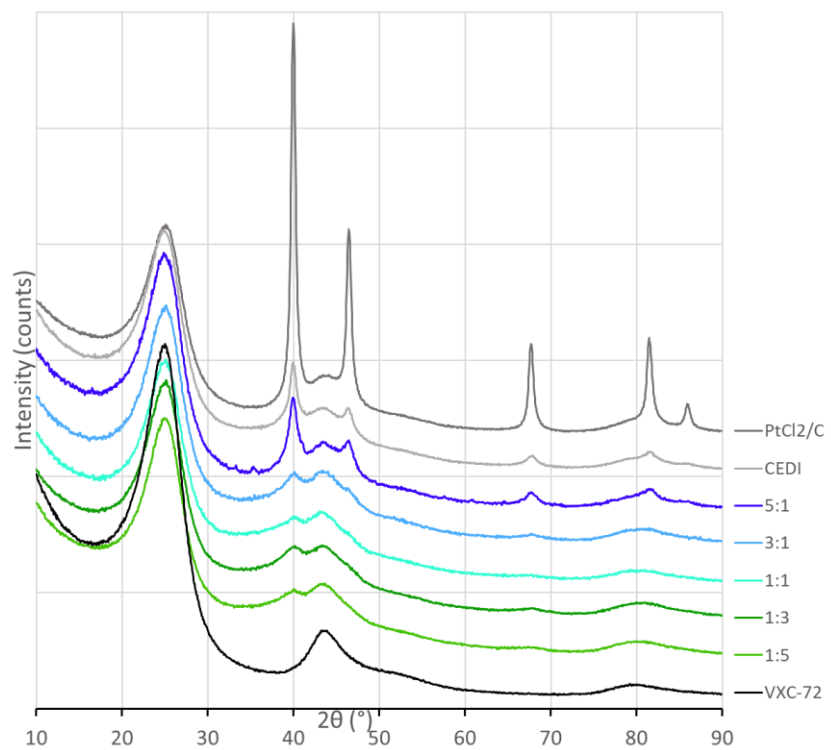


Figure 40. Effect of the molar ratio of acetone to water, while drying at 90°C under 10%H₂/Ar for 30 mins before ramping to 170°C.

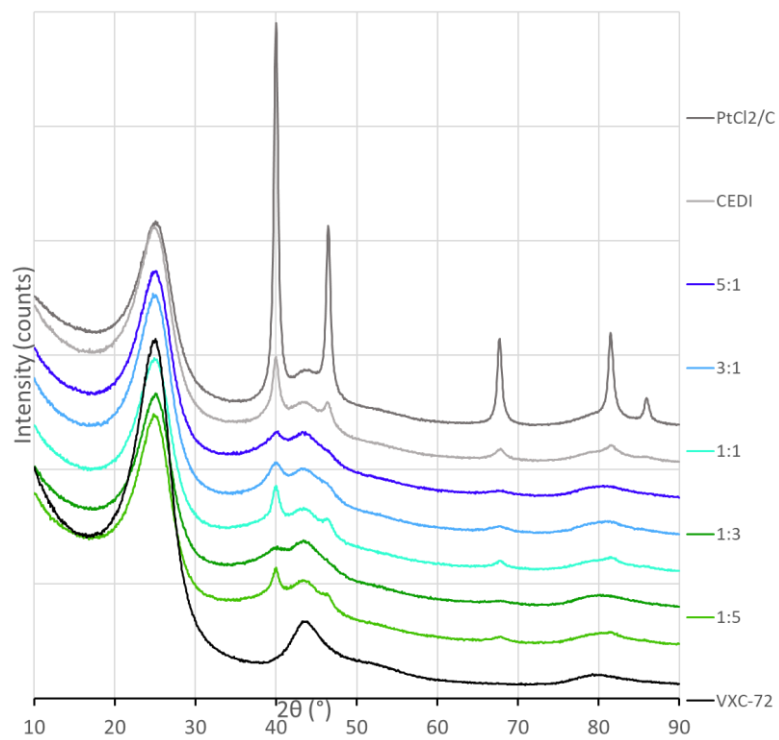


Figure 41. Effect of the molar ratio of acetone to water, while drying at 120°C under 10%H₂/Ar for 30 mins before ramping to 170°C.

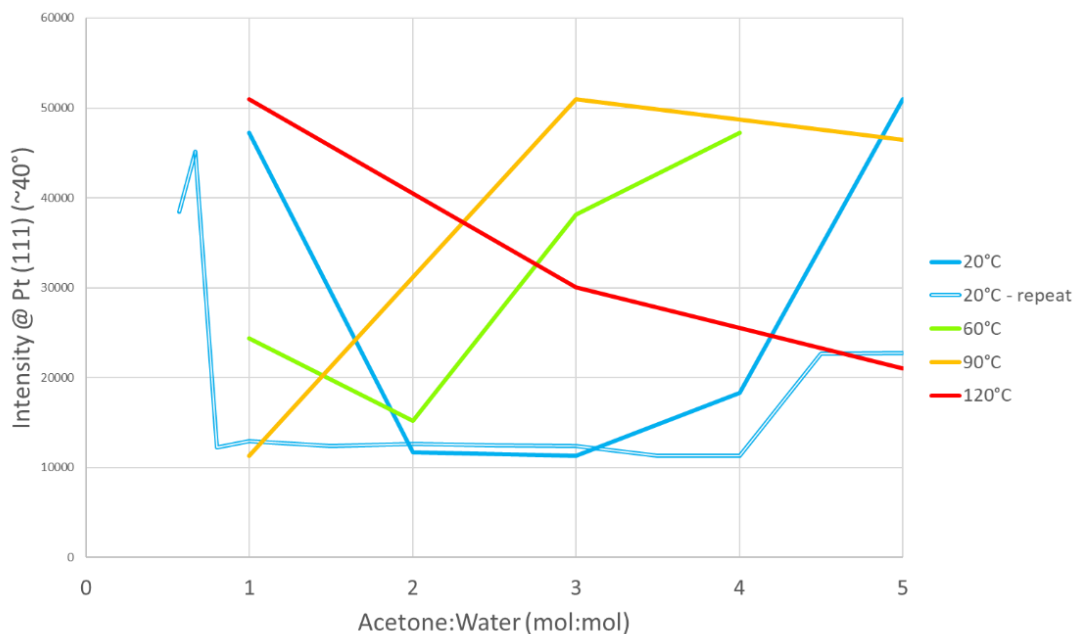


Figure 42. Summary of the effect of drying temperature and acetone:water molar ratio on the particle size of platinum. The y-axis is the intensity of the Pt(111) peak, while the x-axis is the acetone to water ratio. The colors are the temperature of drying that the sample was left at for 30m before ramping to 170°C.

Effect of Solvents Other Than Acetone

Solvent in the previous sections has been shown to have a very strong impact on particle size, simply by changing its proportion. However, we still do not know the cause of acetone's effect in the first place. It was hypothesized in the introduction and in prior work¹¹⁷ that surface tension, boiling point, and dielectric constant played a roll, but these were hypotheses. As the goal of this study was to determine which parameters were important, rather than determine the mechanistic detail behind SwISS, the question of the important solvent properties was addressed by testing other ketones, as well as some other functional groups to see the difference they have with acetone. At the end of this section, functional data analysis with the diffractograms provides some insight into the important solvent properties at play.

Figure 43 shows the effect of solvent-to-water ratio on particle size for two other ketones: 2-butanone, a structurally similar solvent to acetone, and cyclopentanone, a structurally dissimilar solvent to acetone. When comparing these solvents to acetone, it is clear that the structural similarity parallels the SwiSS activity. 2-butanone has a very similar curve to acetone, having a higher particle size above 4:1, and decreasing size with decreasing solvent ratio. At the lowest ratio, around 1.0, the particle is nearly invisible, even with an extremely high weight loading of 7.5%. The cyclopentanone did very little at different ratios to decrease the particle size from its maximum, aside from a moderate decrease at a high solvent ratio. This clarifies the importance of the choice of solvent: The primary functional group may not be the only important characteristic of a particular solvent. Other properties associated with geometry, electronics and orbitals, etc. could be critical as well.

Looking at acetonitrile in Figure 44, it is clearly seen that there is very little effect across a wide range of solvent ratios on the platinum particle size. The middle ratio, around 2, shows a slight increase in particle size. However, this is not a clear trend, and no pattern explains it from the data. Thus, either acetonitrile is missing a property that acetone has, or has an additional property that counteracts the effect of its loading on final metal particle size. 2-ethoxyethanol on the other hand does have some sort of effect that is distinct at low and high solvent ratios. However, the particles are not particularly small.

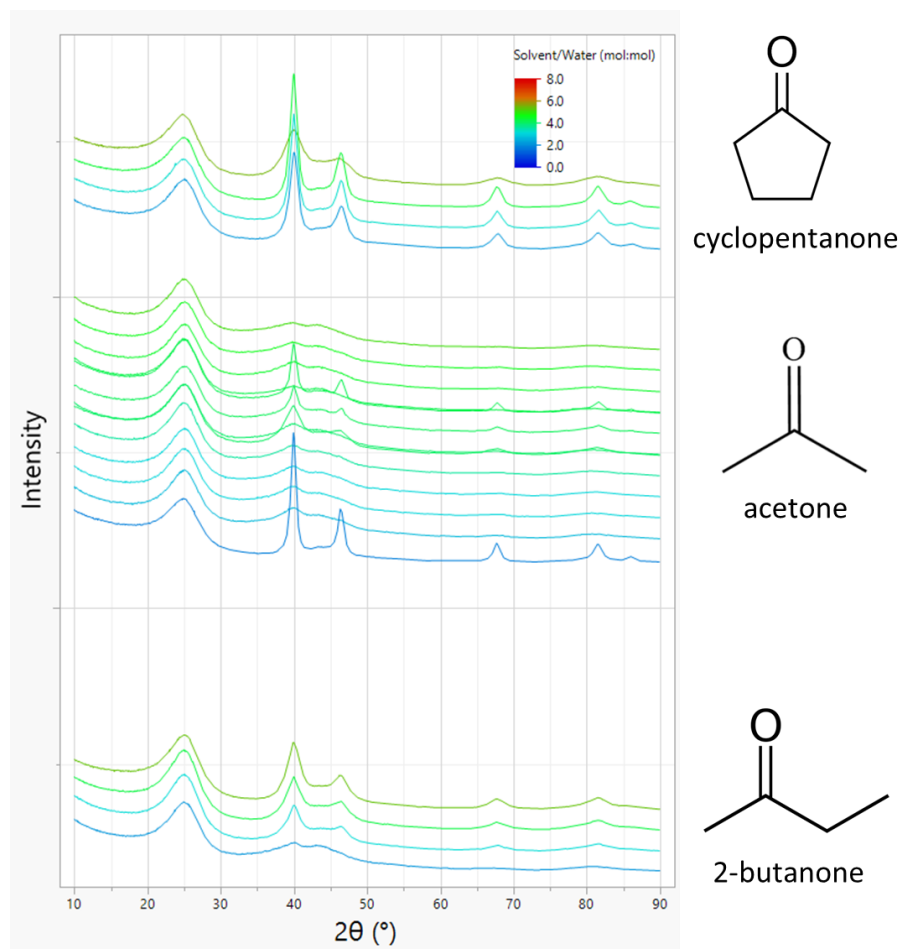


Figure 43. Summary of the effect of solvent:water molar ratio, comparing acetone to cyclopentanone and 2-butanone. The color gradient is a function of the molar ratio of the solvents.

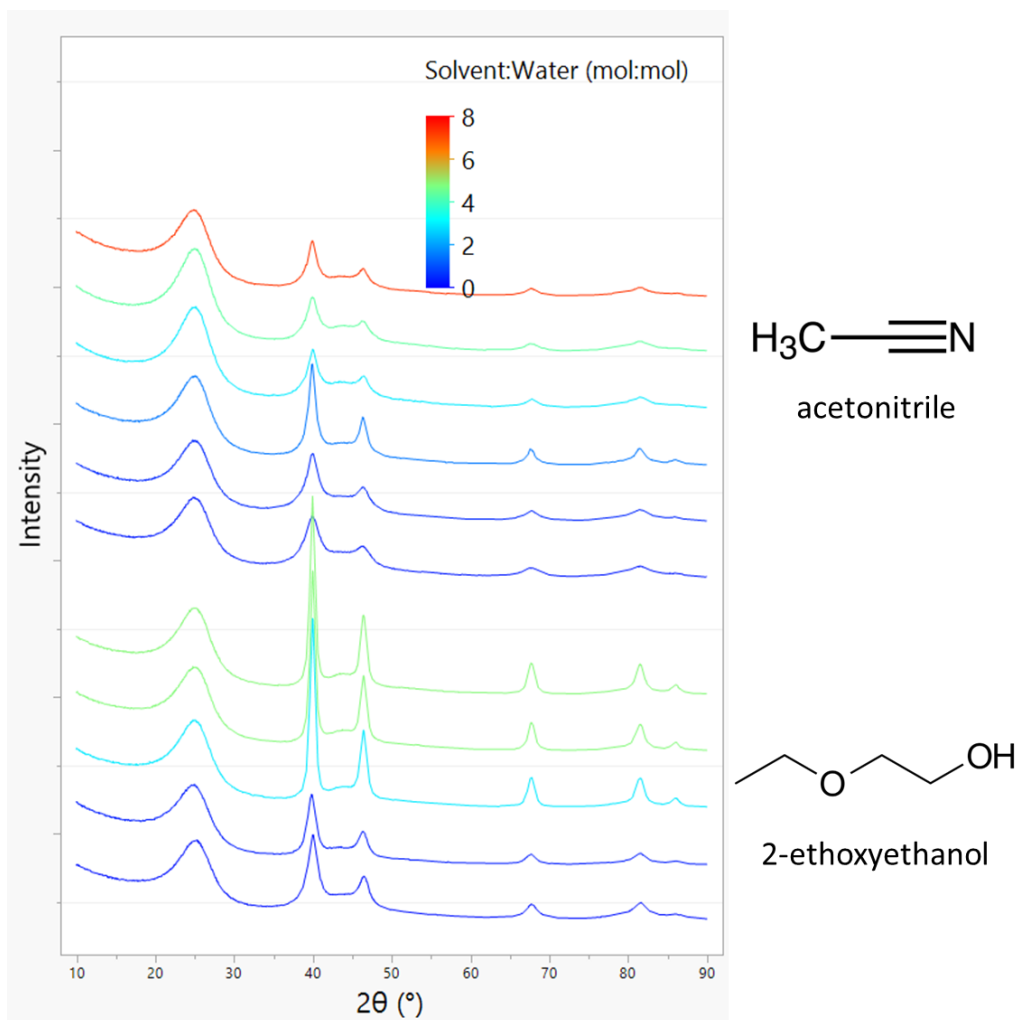


Figure 44. Summary of the effect of solvent:water molar ratio showing new functional groups, such as the nitrile, ether, and alcohol. The color gradient is a function of the molar ratio of the solvents.

In an effort to use this data to make recommendations about the next steps for future projects studying SwiSS, a functional data analysis was performed on the set of 100 XRD diffractograms that were collected over the course of this study. Functional data analysis is similar in principal to linear regression, except that it takes series of data as its output, rather than a single y-value for every x-value. This can be immensely helpful in analyzing a variety of systems, such as a high throughput screening setting where continuous or semi-continuous spectroscopy is taken of each product, and the results need to be

analyzed quickly. A model fit (such as a spline or wavelet model) is fit to the dataset, and the parameters within the model become the y-variable to be fit by x-data.

In this study, the diffractograms are the y-axis data series, while the solvent properties are the x-axis data. The solvent properties were taken from a study by Katritzky, et al. who collected 127 solvents scaled from the literature for 774 solvents. They were able to use a model involving theoretical descriptors to fill in the gaps in the database, and then correlate all of the property scales into 5 Principal Component (PC) Scales that accounted for about 75% of the variance across the properties. The PC scales will be referenced in a moment, but in order to perform the Functional Data Analysis, their database of solvent scales was used to compare to the changes in the diffractograms as a function of the various properties of solvents, accounting for the other changes such as solvent ratio. Other system parameters did not need to be accounted for, as the solvent experiments were done under similar conditions.

Figure 45 shows the results of this analysis. In the top left is a sort of average diffractogram. The vertical red line is at the red value, $39.8^\circ 2\theta$, indicated below. All subsequent plots are the effect of the solvent property, indicated below each plot, at the value of the red line in the first plot, i.e. at $39.8^\circ 2\theta$. The more slope a curve has, the more effect it will have on the platinum peak. As can be seen, a wide variety of solvent properties hold a strong effect on the Pt(111) peak intensity. Some of these have been discussed before, such as dielectric constant and enthalpy of vaporization (almost identical to boiling point). However, there are other interesting ones not discussed, such as acidity and basicity of the solvent. Table 11 shows a representative list of properties which were confirmed to be statistically significant, with regard to the growth of the Pt(111) peak.

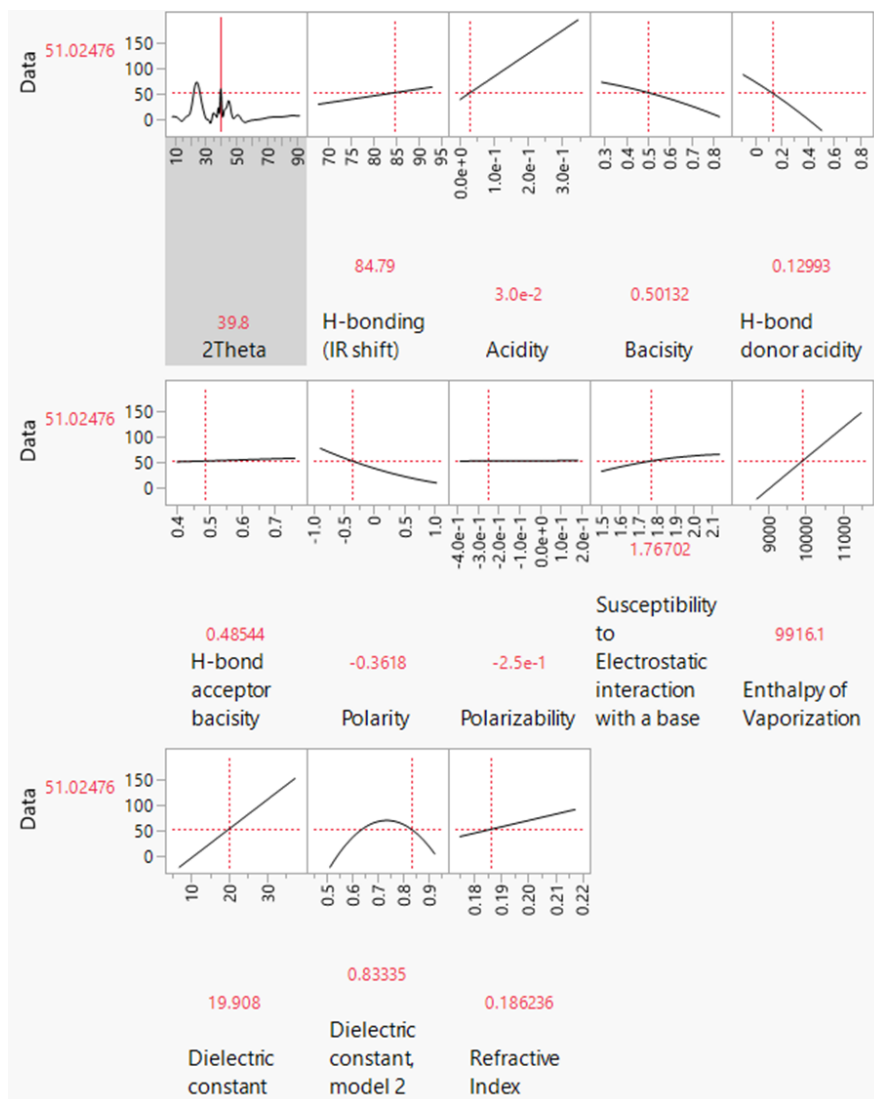


Figure 45. Functional Data Analysis of the diffractograms against certain solvent properties.

Table 11. List of the most statistically significant properties associated with the growth of Pt particles.

Selected solvent properties that strongly correlate to Pt (111) peak intensity	
1	Solvatochromic parameter - index of solvent dipolarity/polarizability
2	Heat of mixing data, for mixtures of chloroform with various solvents
3	Basicity from stretching frequency of CH ₃ OD in solution
4	Solvent basicity, evaluated from UV/Vis spectral shifts of dyes
5	Donor strength – decrease in symmetric stretching frequency of Hg ₂ Br ₂ between the gas phase and solutions

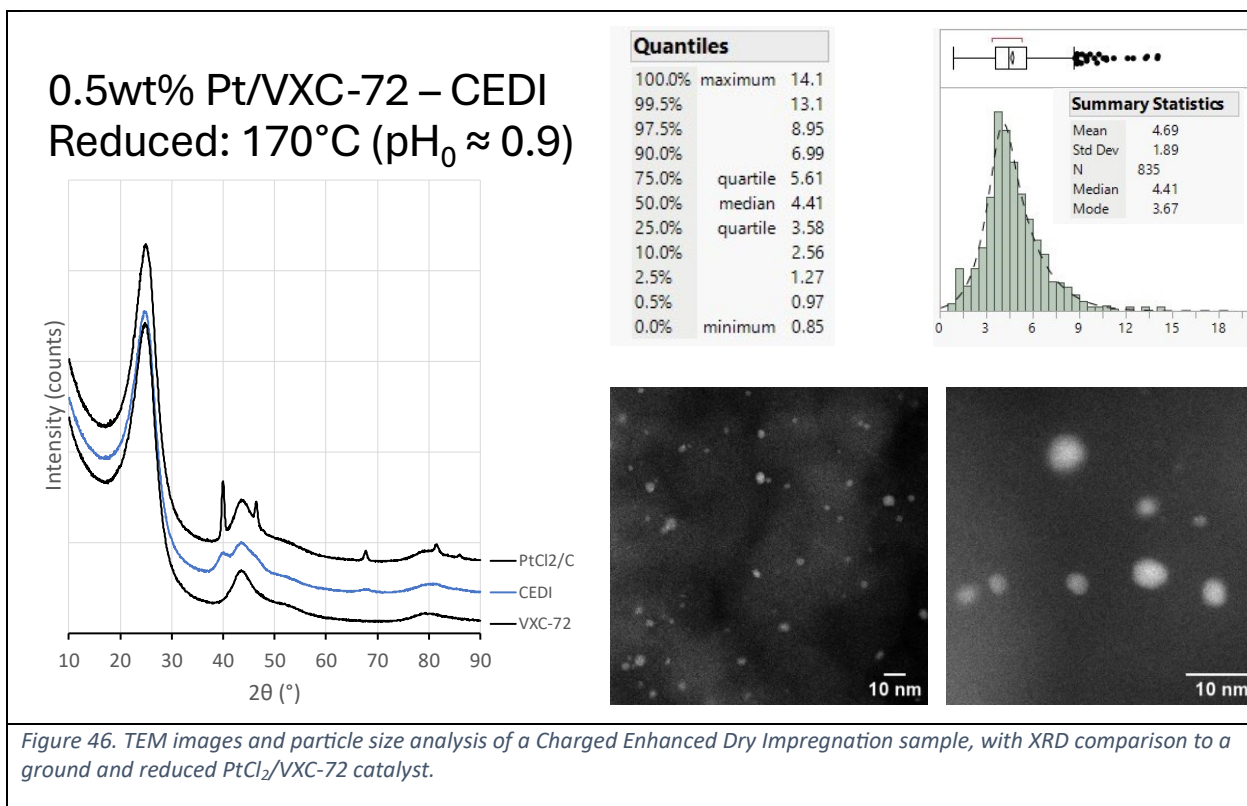
6	Solvatochromic parameter of solvent HBD (hydrogen bond donor) strength
7	Acceptor number , derived from 31P NMR of triethylphosphine oxide
8	F19NMR shielding parameters of fluorobenzene in solution
9	The maximum absorption band of Cu(tmen)(acac)(solv)
10	Relative band intensities(I/III) for benzo[ghi]perylene
11	Relative band intensities(I/III) for ovalene fluorescence
12	Relative band intensities I1/I3 for pyrene fluorescence
13	Ratio of the fluorescence intensities of bands I and III for pyrene
14	Ratio of the fluorescence intensities of bands I and IV of the vibronic spectra of dibenzo[α j]coronene
15	Bathochromic shifts of 6 azo merocyanine dyes
16	Bathochromic UV/Vis spectra shifts of λ_{max} of 4-dimethylamino-4'-nitrostilbene
17	Transition energies for the charge transfer band of a series of merocyanine dyes
18	Transition energy of merocyanine dye (VII)
19	Molar electronic transition energy of dissolved negatively solvatochromic betaine dye
20	Nile red transition energy
21	Calculated from the difference of the longest-wavelength absorption maxima of two merocyanine dyes in solution
22	Perturbation of solvents on the C=O vibration band of acetophenone

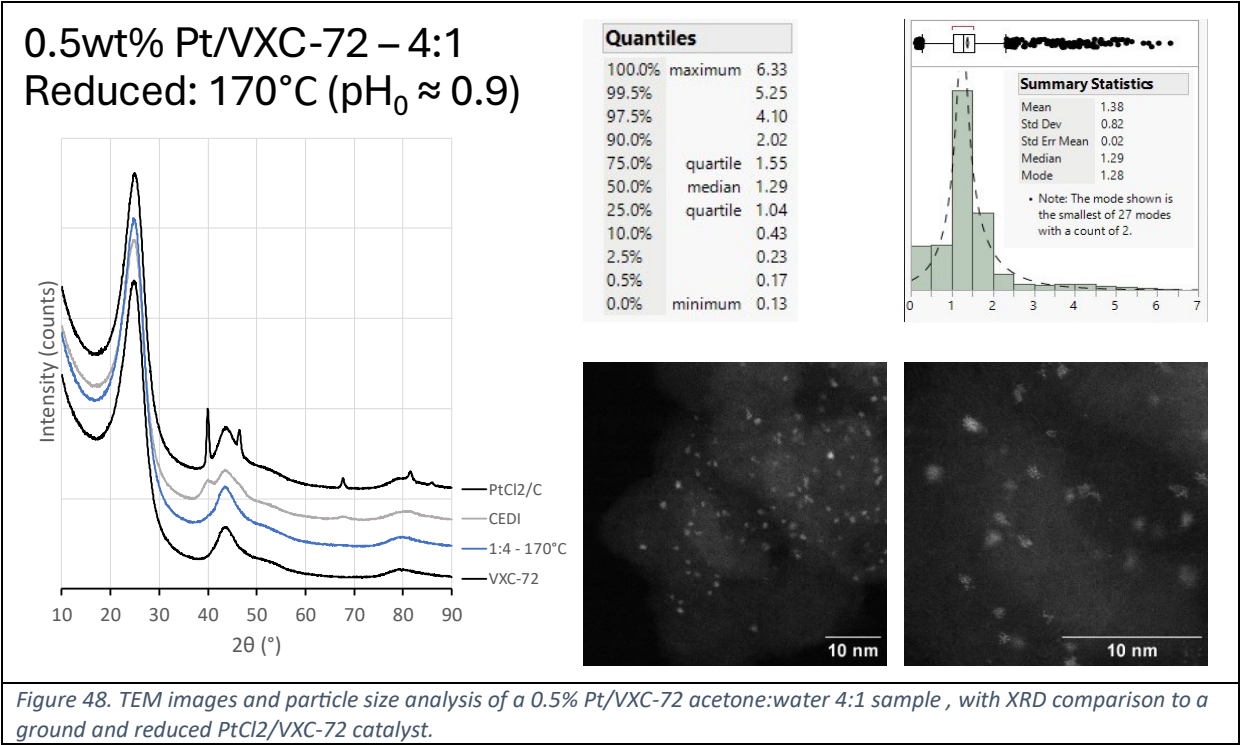
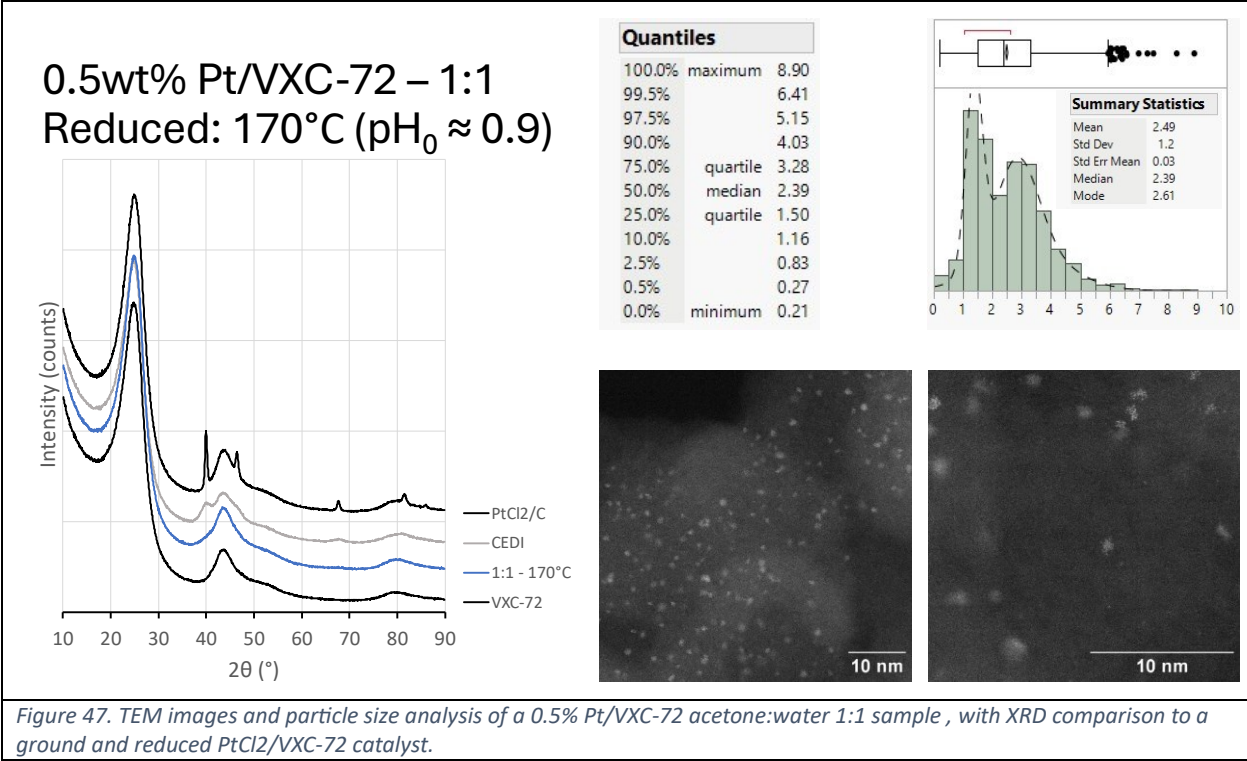
STEM Determined Particle Size

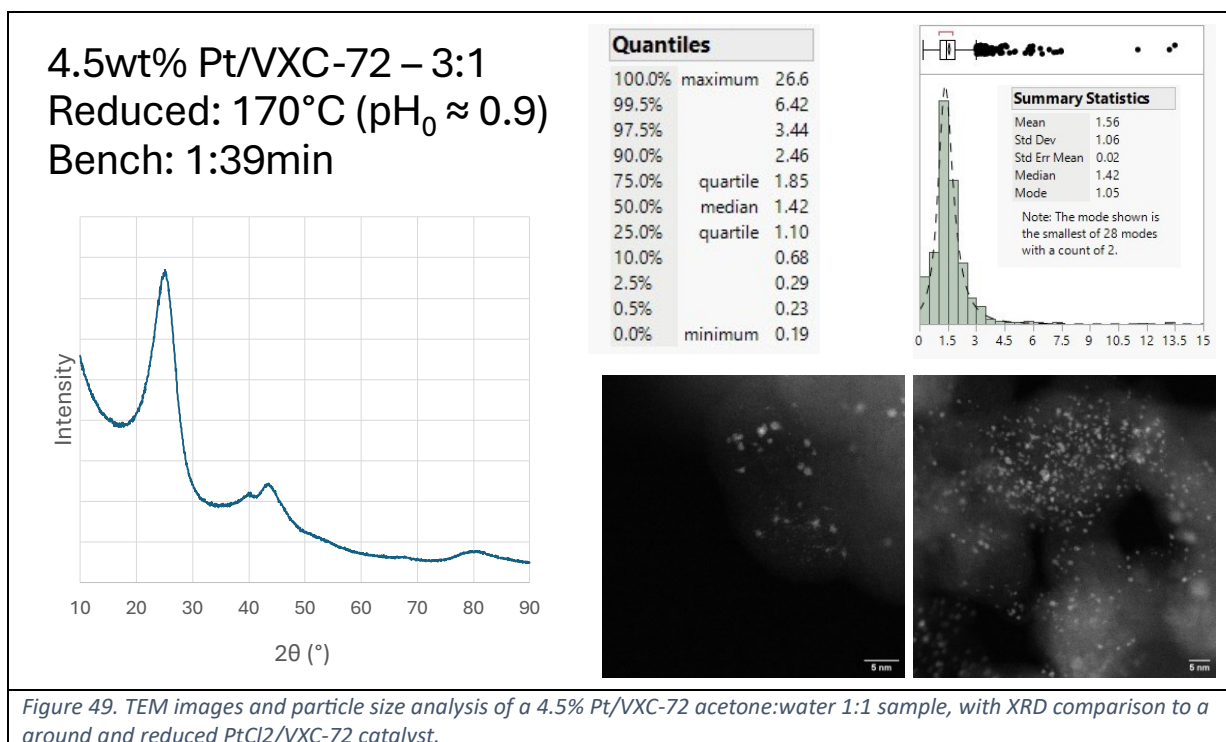
One issue with this dataset is that a large number of the particles are significantly below 1nm, making the calculation of particle size virtually impossible using standard techniques as with the Fityk software package. The initial background subtraction suggested by Liu, et al.¹³⁰ worked for some of the larger samples, but was unable to isolate and resolve the platinum peaks enough to get a realistic, accurate fit. As such, various TEM images were collected and analyzed using Dragonfly by Object Research Systems. 1000 particles was the counting target in every sample except two, which had larger particles and only over 800 could be counted for each. A table summarizing the important experimental information is provided in Table 12. *Experimental Conditions for Each Sample Analyzed with STEM.*

Table 12. Experimental Conditions for Each Sample Analyzed with STEM

#	Sample name	Switching Solvent	Solvent ratio and pretreatment	Tube Size (mL)	Carbon mass (mg)	Time drying in boat on bench (min)(NT=Not Timed)	Wt%
1	CEDI	N/A	R170	15	150	NT	0.5%
2	1:1	Acetone	1:1, R170	15	150	NT	0.5%
3	4:1	Acetone	4:1, R170	15	150	NT	0.5%
4	VCU1	Acetone	3:1, R170	5	75	1:30	4%
5	VCU2	Acetone	3:1, R170	5	75	10:00	4%
6	VCU3	Acetone	3:1, R170	5	75	60:00	4%
7	VCU4	Acetone	3:1, R170	5	75	36h	4%
8	VCU5	ACN	3:1, R170	5	75	3:00	4%
9	VCU6	2-ethoxyethanol	3:1, R170	5	44	3:00	4%







In Figure 46-Figure 49, it can be seen that the XRD data is clearly reflected in the TEM data. The particles of the unoptimized Charge Enhanced Dry Impregnation (CEDI) catalyst are slightly larger (median = 4.41) than the upper bound on their size, were they optimized for pH, which is typically around 1-3nm. The interquartile range is also 2.03nm, while only about 0.5% fall below 1nm. In contrast, the SwISS samples were much smaller across the board as seen in Table 13, with two having about 25% below 1nm.

Table 13. Results of the TEM analysis.

	0.5wt% - CEDI	0.5wt% - 1:1	0.5wt% - 1:4	4.5wt% - 3:1
Median Particle Size (nm)	4.41	2.39	1.29	1.42
Interquartile Range	5.61-3.58	1.50-3.28	1.04-1.55	1.10-1.85
% that fall below 1nm	~0.5	~5%	~25%	~23%
Smallest Particle (nm)	0.85	0.21	0.13	0.19
Largest Particle (nm)	14.1	8.90	6.33	26.6

Conclusions and recommendations

A comprehensive study was performed on the adsorption of platinum ions onto the surface of VXC-72, in the context of Switched Solvent Synthesis (SwiSS). It was shown that many process variables such as mixing conditions (shaking time, acceleration, and container volume), drying temperature, and solvent ratio to water have significant impacts on particle size, though container volume seems to have a high variation in its effect. Certain observable parameters were monitored, including flowability of the slurry, degree of settling to the bottom of the boat, and spontaneous flow were also found to have some effect, though the level of settling far outpaced the other two. Conversely, the time of drying on the bench before entering the furnace seems to have a marginal effect, and only at time spans far greater than the few seconds or minutes needed to adequately perform the mixing. Solvent also plays a huge role, not only in its ratio to water, but also in what solvent is being used. Simple exchanges within the same traditional family of molecules will not always work, as seen with acetone and cyclopentanone. Perhaps the most tremendous result is that samples up to 8 wt% were synthesized with significant portions of particles below 1nm, including what appeared to be significant amounts of clusters. While a noble metal catalyst with clusters could hardly be called efficient at 8 wt%, this shows the serious power of the SwiSS method: To be able to make catalysts with sub-nanometer particles with an unoptimized solution of water and subsequently, acetone.

Unfortunately the mechanisms behind why SwiSS works so well are still not yet fully revealed. Currently work is being done on two fronts, to decipher the solvent property space by using the principal component (PC) model by Katritzky et al.¹³¹ as an orthogonal set of factors in a design of experiments. The results will then be compared not to the principal components themselves, but to the actual properties collected and calculated by Katritzky, via methods such as functional data analysis and partial least squares. The PC model will therefore allow a non-biased sampling of the solvent property space, and testing of each property for activity in SwiSS. The other project being conducted is an attempt to

gain clarity about the microscopic nature of drying when a metal is strongly adsorbed to a surface, such as in strong electrostatic adsorption, or in a Swiss context. These two projects will build upon this work by teasing out the mechanisms of the effects that have herein been determined to be significant for Swiss.

Chapter Five: Conclusions

This thesis has focused on a variety of adjustments to the traditional wet and dry impregnation procedures. First, an investigation into the effect of temperature on adsorption was performed, focusing on Strong Electrostatic Adsorption (SEA), and its formal model, the Revised Physical Adsorption (RPA) model. In this investigation, the RPA model was first expanded to account for all the effects of temperature, both direct and indirect. This not only required adding equations to the RPA model, it required changing the governing adsorption equation: Langmuir isotherm. Then, multiple systems were tested to see how they comport with the updated RPA model. The pH-shift at high surface loading experiments worked well, generally capturing most of the features. However, inclusion of ammonia as a base led to complications. These were largely mitigated by the switching to sodium hydroxide instead. The adsorption isotherms required more finesse. For one, the measured PZC of some of the supports was likely due to impurities. However, the adsorption acts as if there were a pure PZC value. This and the number of hydration sheaths had to be optimized. In addition, certain systems fundamentally did not follow the RPA model. While some of these make sense, like BaTiO_3 as it is prone to dissolving quickly in acidic media, others such as TiO_2 don't make much sense, and require further study. The major takeaway is that while the RPA model may be able to handle certain conditions better for well behaved systems such as Pt/SiO_2 , the effect of temperature is one that does not appear to have a significant effect on particle size.

The second study addressed another condition of SEA: That of the ionic strength. From Chapter One, it can be seen that ion content should have an effect on the surface metal interface, especially in the context of SEA. In this project, multiple salts were tested at various ionic strengths for their effect on Platinum particle size. Oddly enough, even at loadings of 90:1 anion to platinum, there was no effect on particle size. Overall ionic strength does not seem like a good additional variable to keep track of during SEA.

In the third project, Switched Solvent Synthesis (SwiSS) was used to create sub-nanometer particles at extremely high weight loadings, up to over 8% Pt/vulcanized carbon. In contrast to the foregoing studies into temperature and ionic strength, this study yielded a multitude of possible parameters to explore further. Some include mixing conditions (mixing tube, rate, and time), drying conditions in the furnace, temperature of drying, and solvent. Conversely,

some parameters were not found to be significant, such as time of ambiently drying in the boat. Certain conditions can yield catalysts with an excess of 25% particle size below 1nm, and a quarter the size of a simple wet impregnation. SwiSS can then be thought of as a companion technique to SEA. However, the physical property space is vast, and a systematic investigation of each of the important parameters determined here need to be investigated.

Two projects furthering the art of both SwiSS and SEA are already underway: 1) a drying project, systematically determining the difference between the surface phase water and organic solvents, as opposed to the bulk phase solvents. These surface interactions could lead to dramatic differences in solvent behavior, 2) a solvent property project, focusing on the difference between different solvents. This project is using a generalized principal component model for the solvent property space. This will allow the DoE to be performed in a manner as un-biased as possible. Upon collection of the data, the diffractograms, XPS output, etc. will be fit using either functional data analysis or partial least squares to the solvent properties to see which properties are predictive of the behavior. In general, moving forward, more proper XRD analysis will be used, such as Rietveld Refinement, so that more definite values can be had from the XRD diffractogram. As these progress, the understanding of how solvents and drying methods influence the synthesis and stability of nanoparticles will deepen. The outcomes from these studies will provide valuable insights into optimizing the conditions for metal deposition and nanoparticle formation, crucial for the design of more efficient and robust catalysts.

Overall, this work has explored the interplay between process conditions and impregnation procedures. While some results pushed up against the limits of science, others found new avenues, particularly in the realm of SwiSS. The intricate relationships between the operational parameters and the physicochemical properties of the nanoparticles suggest a complex yet rich field of study that promises significant advancements in catalyst technology. This thesis not only contributes to the academic knowledge but also lays a foundation for future investigations, aiming to optimize catalyst performance across various reactions.

References

- (1) *Catalysis Looks to the Future*; National Research Council, Washington, DC, 1992. <https://nap.nationalacademies.org/catalog/1903/catalysis-looks-to-the-future> (accessed 10/01/2022). DOI: 10.17226/1903.
- (2) Peters, M. H. *Molecular Thermodynamics and Transport Phenomena: Complexities of Scales in Space and Time*; The McGraw-Hill Companies, Inc., 2005. DOI: 10.1036/0071445617.
- (3) catalyst. In *IUPAC. Compendium of Chemical Terminology*, 2nd ed.; McNaught, A. D., Wilkinson, A. Eds.; Blackwell Scientific Publications, 1997.
- (4) Convention, U. P. <232> ELEMENTAL IMPURITIES—LIMITS. In *United States Pharmacopeia and National Formulary (USP-NF)*, 39th ed.; US Pharmacopeial Convention, 2016.
- (5) Collman, J. P.; Zhong, W.; Straumanis, A.; Quelpejeu, M.; Rose, E. An Efficient Catalyst for Asymmetric Epoxidation of Terminal Olefins. *Journal of the American Chemical Society* **1999**, *121* (2), 460-461. DOI: <https://doi.org/10.1021/ja9818699> (accessed 4/16/2024). From VCU Library.
- (6) Cole-Hamilton, D. J. Homogeneous catalysis--new approaches to catalyst separation, recovery, and recycling. *Science* **2003**, *299* (5613), 1702-1706. DOI: 10.1126/science.1081881 (accessed 4/16/2024). From VCU Libraries ProQuest.
- (7) Yang, Y.; Gilliland III, S. E.; Ghobadi, S.; Burkholder, M.; Smith, S. E.; Gupton, B. F.; Castano, C. E. Three dimensional composites of graphene as supports in Pd-catalyzed synthetic applications. *Reaction Chemistry & Engineering* **2019**, *4* (1), 90-99. DOI: <https://doi.org/10.1039/C8RE00185E> (accessed 4/17/2024). From VCU Library.
- (8) Ud Din, I.; Nasir, Q.; Garba, M. D.; Alharthi, A. I.; Alotaibi, M. A.; Usman, M. A Review of Preparation Methods for Heterogeneous Catalysts. *Mini-Reviews in Organic Chemistry* **2022**, *19* (1), 92-110. DOI: 10.2174/1570193X18666210308151136 (accessed 4/17/2024). From VCU ILLiad.
- (9) Vethosodsakda, T.; Free, M. L.; Janwong, A.; Moats, M. S. Evaluation of liquid retention capacity measurements as a tool for estimating optimal ore agglomeration moisture content. *International Journal of Mineral Processing* **2013**, *119*, 58-64. DOI: <https://doi.org/10.1016/j.minpro.2012.12.005> (accessed 4/17/2024). From VCU Library.
- (10) Afrassiabian, Z.; Leturia, M.; Benali, M.; Guessasma, M.; Saleh, K. An overview of the role of capillary condensation in wet caking of powders. *Chemical Engineering Research and Design* **2016**, *110*, 245-254. DOI: <https://doi.org/10.1016/j.cherd.2016.03.020> (accessed 4/17/2024). From VCU Library.
- (11) Urso, M. E. D.; Lawrence, C. J.; Adams, M. J. Pendular, Funicular, and Capillary Bridges: Results for Two Dimensions. *Journal of Colloid and Interface Science* **1999**, *220* (1), 42-56. DOI: <https://doi.org/10.1006/jcis.1999.6512> (accessed 4/17/2024). From VCU Library.
- (12) Zhang, C.; Lu, N. Unitary Definition of Matric Suction. *Journal of Geotechnical and Geoenvironmental Engineering* **2018**, *145* (2), 1. DOI: [https://doi.org/10.1061/\(ASCE\)GT.1943-5606.000200](https://doi.org/10.1061/(ASCE)GT.1943-5606.000200) (accessed 4/18/2024). From VCU Library.
- (13) Zhang, L.; Yu, X.; Chen, Z.; Li, J.; Hui, G.; Yang, M.; Yu, R. Capillary dynamics of confined water in nanopores: The impact of precursor films. *Chemical Engineering Journal* **2021**, *409*, 1-10. DOI: <https://doi.org/10.1016/j.cej.2020.128113> (accessed 4/18/2024). From VCU Libraries.
- (14) Asay, D. B.; Kim, S. H. Evolution of the Adsorbed Water Layer Structure on Silicon Oxide at Room Temperature. *The Journal of Physical Chemistry B* **2005**, *109* (35), 16760-16763. DOI: <https://doi.org/10.1021/jp053042o> (accessed 4/18/2024). From VCU Libraries.
- (15) Urashima, S.; Uchida, T.; Yui, H. A hydrogen-bonding structure in self-formed nanodroplets of water adsorbed on amorphous silica revealed via surface-selective vibrational spectroscopy. *Physical Chemistry Chemical Physics* **2020**, *22*, 27031-27036. DOI: 10.1039/D0CP03207G (accessed 4/18/2024). From VCU Library.

- (16) International Union of Pure and Applied Chemistry, P. C. D., Commission on Colloid and Surface Chemistry. MANUAL OF SYMBOLS AND TERMINOLOGY FOR PHYSICOCHEMICAL QUANTITIES AND UNITS- APPENDIX II - Definitions, Terminology and Symbols in Colloid and Surface Chemistry - PART II: HETEROGENEOUS CATALYSIS. *Pure and Applied Chemistry* **1976**, *46* (1), 71-90. DOI: <https://doi.org/10.1351/pac197646010071> (accessed 4/18/2024). From VCU Libraries.
- (17) Hao, X.; Barnes, S.; Regalbuto, J. R. A fundamental study of Pt impregnation of carbon: Adsorption equilibrium and particle synthesis. *Journal of Catalysis* **2011**, *279* (1), 48-65. DOI: <https://doi.org/10.1016/j.jcat.2010.12.021> (accessed 4/11/2024). From VCU Libraries.
- (18) Mehrabadi, B. A. T.; Eskandari, S.; Khan, U.; White, R. D.; Regalbuto, J. R. Advances in Catalysis. In *ACS Catalysis*, Song, C. Ed.; A Review of Preparation Methods for Supported Metal Catalysts, Vol. 61; Elsevier, Inc., 2017; pp 1-35.
- (19) Nelmark, A. V.; Kheifets, L. I.; Fenelonov, V. B. Theory of preparation of supported catalysts. *Industrial & Engineering Chemistry Product Research and Development* **1981**, *20* (3), 439-450. DOI: 10.1021/i300003a006 (accessed 10/13/2022). From VCU Libraries.
- (20) Zhuravlev, L. T. The surface chemistry of amorphous silica. Zhuravlev model. *Colloids and Surfaces A: Physicochemical and Engineering Aspects* **2000**, *173* (1-3), 1-38. DOI: [https://doi.org/10.1016/S0927-7757\(00\)00556-2](https://doi.org/10.1016/S0927-7757(00)00556-2) (accessed 4/19/2024). From VCU Libraries.
- (21) Kan, Y.; Zhang, Q. Transition Metal Complexes for Hydrogen Activation. In *Nanostructured Materials for Next-Generation Energy Storage and Conversion Hydrogen Production, Storage, and Utilization*, Chen, Y.-P., Bashir, S., Liu, J. L. Eds.; Springer-Verlag GmbH, 2017; pp 43-84.
- (22) Yuvaraj, S.; Fan-Yuan, L.; Tsong-Huei, C.; Chuin-Tih, Y. Thermal Decomposition of Metal Nitrates in Air and Hydrogen Environments. *The Journal of Physical Chemistry B* **2003**, *107* (4), 1044-1047. DOI: <https://doi.org/10.1021/jp026961c> (accessed 4/19/2024). From VCU Library.
- (23) Luidold, S.; Antrekowitsch, H. Hydrogen as a reducing agent: State-of-the-art science and technology. *The Journal of The Minerals, Metals & Materials Society (JOM)* **2007**, *59*, 20-26. DOI: <https://doi.org/10.1007/s11837-007-0072-x> (accessed 4/19/2024). From VCU Library.
- (24) LaMer, V. K.; Dinegar, R. H. Theory, Production and Mechanism of Formation of Monodispersed Hydrosols. *Journal of the American Chemical Society* **1950**, *72* (11), 4847-4854. DOI: <https://doi.org/10.1021/ja01167a001> (accessed 4/19/2024). From VCU Libraries.
- (25) Thanh, N. T. K.; Maclean, N.; Mahiddine, S. Mechanisms of Nucleation and Growth of Nanoparticles in Solution. *Chemical Reviews* **2014**, *114* (15), 7610-7630. DOI: <https://doi.org/10.1021/cr400544s> (accessed 4/19/2024). From VCU Library.
- (26) Besson, C.; Finney, E. E.; Finke, R. G. A Mechanism for Transition-Metal Nanoparticle Self-Assembly. *Journal of the American Chemical Society* **2005**, *127* (22), 8179-8184. DOI: <https://doi.org/10.1021/ja0504439> (accessed 4/19/2024). From VCU Library.
- (27) Watzky, M. A.; Finke, R. G. Transition Metal Nanocluster Formation Kinetic and Mechanistic Studies. A New Mechanism When Hydrogen Is the Reductant: Slow, Continuous Nucleation and Fast Autocatalytic Surface Growth. *Journal of the American Chemical Society* **1997**, *119* (43), 10382-10400. DOI: <https://doi.org/10.1021/ja9705102> (accessed 4/19/2024). From VCU Library.
- (28) Mindset, T. E. Capacitors Explained - The basics how capacitors work working principle. Youtube, Aug 25, 2019. <https://www.youtube.com/watch?v=X4EUwTwZ110> (accessed 3/21/2024).
- (29) Helmholtz, H. Ueber galvanische Polarisation in gasfreien Flüssigkeiten. *Annalen der Physik* **1874**, *226* (11), 483-495. DOI: <https://doi.org/10.1002/andp.18742261116>.
- (30) Ivanov, V. D. The Helmholtz model. *Journal of Solid State Electrochemistry* **2024**. DOI: <https://doi.org/10.1007/s10008-024-05850-5> (accessed 3/21/2024).

- (31) Gouy, L. G. Sur la constitution de la charge électrique à la surface d'un électrolyte. *Journal de Physique Théorique et Appliquée* **1910**, 9 (1), 457-468. DOI: 10.1051/jphys:019100090045700 (accessed 3/21/2024).
- (32) Chapman, D. L. A contribution to the theory of electrocapillarity. *The London, Edinburgh, and Dublin Philosophical Magazine and Journal of Science* **1913**, 25 (148), 475-481. DOI: <https://doi.org/10.1080/14786440408634187> (accessed 3/21/2024).
- (33) Stern, O. ZUR THEORIE DER ELEKTROLYTISCHEN DOPPELSCHICHT. *Zeitschrift für Elektrochemie und angewandte physikalische Chemie* **1924**, 30 (21-22), 508-516. DOI: <https://doi.org/10.1002/bbpc.192400182> (accessed 3/22/2024).
- (34) Rahm, M.; Hoffman, R.; Ashcroft, N. W. Atomic and Ionic Radii of Elements 1-96. *Chemistry—A European Journal* **2016**, 22 (41), 14625-14632. DOI: 10.1002/chem.201602949 (accessed 11/18/2022). From VCU Library.
- (35) Debye, P.; Hückel, E. Zur Theorie der Elektrolyte. I. Gefrierpunktserniedrigung und verwandte Erscheinungen. *Physikalische Zeitschrift* **1923**, 24 (9), 185-206. (accessed 3/31/2024). From HathiTrust.
- (36) Frank, H. S. Local Dielectric Constant and Solute Activity. A Hydration-Association Model for Strong Electrolytes. *Journal of the American Chemical Society* **1941**, 63 (7), 1789-1799. DOI: <https://doi.org/10.1021/ja01852a003> (accessed 4/1/2024). From VCU Library.
- (37) Stokes, R. H.; Robinson, R. A. Ionic Hydration and Activity in Electrolyte Solutions. *Journal of the American Chemical Society* **1948**, 70 (5), 1870-1878. DOI: <https://doi.org/10.1021/ja01185a065> (accessed 4/1/2024). From VCU Libraries.
- (38) Grahame, D. C. The Electrical Double Layer and the Theory of Electrocapillarity. *Chemical Reviews* **1947**, 41 (3), 441-501. DOI: <https://doi.org/10.1021/cr60130a002> (accessed 4/1/2024). From VCU Libraries.
- (39) Fuerstenau, D. W. Interfacial processes in mineral/water systems. *Pure and Applied Chemistry* **1970**, 24 (1), 135. DOI: <https://doi.org/10.1351/pac197024010135> (accessed 4/4/2024).
- (40) James, R. O.; Healy, T. W. Adsorption of hydrolyzable metal ions at the oxide—water interface. I. Co(II) adsorption on SiO₂ and TiO₂ as model systems. *Journal of Colloid and Interface Science* **1972**, 40 (1), 42-52. DOI: [https://doi.org/10.1016/0021-9797\(72\)90172-5](https://doi.org/10.1016/0021-9797(72)90172-5) (accessed 4/4/2024). From VCU Libraries.
- (41) James, R. O.; Healy, T. W. Adsorption of hydrolyzable metal ions at the oxide—water interface. III. A thermodynamic model of adsorption. *Journal of Colloid and Interface Science* **1972**, 40 (1), 65-81. DOI: 10.1016/0021-9797(72)90174-9 (accessed 09/05/2022).
- (42) Andersen, T. N.; Bockris, J. O. M. Forces involved in the “specific” adsorption of ions on metals from aqueous solution. *Electrochimica Acta* **1964**, 9 (4), 347-371. DOI: [https://doi.org/10.1016/0013-4686\(64\)80042-6](https://doi.org/10.1016/0013-4686(64)80042-6) (accessed 4/6/2024). From VCU Libraries.
- (43) James, R. O.; Healy, T. W. Adsorption of hydrolyzable metal ions at the oxide—water interface. II. Charge reversal of SiO₂ and TiO₂ colloids by adsorbed Co(II), La(III), and Th(IV) as model systems. *Journal of Colloid and Interface Science* **1972**, 40 (1), 53-64. DOI: [https://doi.org/10.1016/0021-9797\(72\)90173-7](https://doi.org/10.1016/0021-9797(72)90173-7) (accessed 4/6/2024). From VCU Libraries.
- (44) Healy, T. W.; Yates, D. E.; White, L. R.; Chan, D. Nernstian and non-Nernstian potential differences at aqueous interfaces. *Journal of Electroanalytical Chemistry and Interfacial Electrochemistry* **1977**, 80 (1), 57-66. DOI: [https://doi.org/10.1016/S0022-0728\(77\)80103-4](https://doi.org/10.1016/S0022-0728(77)80103-4) (accessed 4/8/2024). From VCU Libraries.
- (45) Healy, T. W.; White, L. R. Ionizable surface group models of aqueous interfaces. *Advances in Colloid and Interface Science* **1978**, 9 (4), 303-345. DOI: [https://doi.org/10.1016/0001-8686\(78\)85002-7](https://doi.org/10.1016/0001-8686(78)85002-7) (accessed 4/8/2024).
- (46) Agashe, K. B.; Regalbuto, J. R. A Revised Physical Theory for Adsorption of Metal Complexes at Oxide Surfaces. *Journal of Colloid and Interface Science* **1996**, 185 (1), 174-189. DOI: <https://doi.org/10.1006/jcis.1996.4493> (accessed 4/8/2024). From VCU Libraries.

- (47) Yates, D. E.; Levine, S.; Healy, T. W. Site-binding model of the electrical double layer at the oxide/water interface. *Journal of the Chemical Society, Faraday Transactions 1: Physical Chemistry in Condensed Phases* **1974**, 70 (0), 1807-1818. DOI: <https://doi.org/10.1039/F19747001807> (accessed 4/8/2024). From VCU Libraries.
- (48) Grotthuss, C. J. T. D. Sur la composition de l'eau et des corps qu'elle tient en dissolution laide de l'électricité galvanique. In *Annales De Chimie*, J. de Boffe: 1806; pp 54-75.
- (49) Marx, D.; Tuckerman, M. E.; Hutter, J.; Marrinello, M. The nature of the hydrated excess proton in water. *Nature* **1999**, 397, 601-604. DOI: <https://doi.org/10.1038/17579> (accessed 4.8/2024). From VCU Libraries.
- (50) Park, J.; Regalbuto, J. R. A Simple, Accurate Determination of Oxide PZC and the Strong Buffering Effect of Oxide Surfaces at Incipient Wetness. *Journal of Colloid and Interface Science* **1995**, 175 (1), 239-252. DOI: 10.1006/jcis.1995.1452 (accessed 09/06/2022).
- (51) Levine, S.; Mingsins, J.; Bell, G. M. The discrete-ion effect in ionic double-layer theory. *Journal of Electroanalytical Chemistry and Interfacial Electrochemistry* **1967**, 13 (3), 280-329. DOI: [https://doi.org/10.1016/0022-0728\(67\)80125-6](https://doi.org/10.1016/0022-0728(67)80125-6) (accessed 4/9/2024). From VCU Libraries.
- (52) Wiese, G. R.; James, R. O.; Healy, T. W. Discreteness of charge and solvation effects in cation adsorption at the oxide/water interface. *Discussions of the Faraday Society* **1971**, 52, 302-311. DOI: DOI <https://doi.org/10.1039/DF9715200302> (accessed 4/9/2024). From VCU Libraries.
- (53) Kausch, H. H.; Fesko, D. G.; Tschögl, N. W. The Random Packing of Circles in a Plane. *Journal of Colloid and Interface Science* **1971**, 37 (3), 603-611. DOI: [https://doi.org/10.1016/0021-9797\(71\)90338-9](https://doi.org/10.1016/0021-9797(71)90338-9) (accessed 4/9/2024). From VCU Library.
- (54) Hao, X.; Spieker, W. A.; Regalbuto, J. R. A further simplification of the revised physical adsorption (RPA) model. *Journal of Colloid and Interface Science* **2003**, 267 (2), 259-264. DOI: 10.1016/S0021-9797(03)00644-1 (accessed 09/05/2022).
- (55) Regalbuto, J. R.; Navada, A.; Shadid, S.; Bricker, M. L.; Chen, Q. An Experimental Verification of the Physical Nature of Pt Adsorption onto Alumina. *Journal of Catalysis* **1999**, 184 (2), 335-348. DOI: 10.1006/jcat.1999.2471 (accessed 09/05/2022).
- (56) Park, C.; Fenter, P. A.; Sturchio, N. C.; Regalbuto, J. R. Probing Outer-Sphere Adsorption of Aqueous Metal Complexes at the Oxide-Water Interface with Resonant Anomalous X-Ray Reflectivity. *Physical Review Letters* **2005**, 94 (7), 1-4. DOI: <https://doi.org/10.1103/PhysRevLett.94.076104> (accessed 4/1/2024). From VCU Libraries.
- (57) Noble, S. R.; Barnes, S. E.; Banerjee, R.; Miller, J.; Regalbuto, J. R. Supported nanoparticle synthesis with Au bis-Ethylenediamine: The mechanism of adsorption onto oxides and carbons. *Journal of Catalysis* **2021**, 393 (Special Issue in Honour of Prof. Michel Che), 344-356. DOI: <https://doi.org/10.1016/j.jcat.2020.11.026> (accessed 4/11/2024). From VCU Libraries.
- (58) Spieker, W. A.; Liu, J.; Miller, J. T.; Regalbuto, J. R. An EXAFS study of the co-ordination chemistry of hydrogen hexachloroplatinate(IV): 1. Speciation in aqueous solution. *Applied Catalysis A: General* **2002**, 232 (1-2), 219-235. DOI: 10.1016/S0926-860X(02)00116-3 (accessed 09/07/2022).
- (59) Spieker, W. A.; Liu, J.; Hao, X.; Miller, J. T.; Kropf, A. J.; Regalbuto, J. R. An EXAFS study of the coordination chemistry of hydrogen hexachloroplatinate (IV) 2. Speciation of complexes adsorbed onto alumina. *Applied Catalysis A: General* **2003**, 243 (1), 53-66. DOI: [https://doi.org/10.1016/S0926-860X\(02\)00537-9](https://doi.org/10.1016/S0926-860X(02)00537-9) (accessed 4/11/2024). From VCU Libraries.
- (60) D'Souza, L.; Jiao, L.; Regalbuto, J. R.; Miller, J. T.; Kropf, A. J. Preparation of silica- and carbon-supported cobalt by electrostatic adsorption of Co(III) hexaammines. *Journal of Catalysis* **2007**, 248 (2), 165-174. DOI: <https://doi.org/10.1016/j.jcat.2007.03.010> (accessed 4/11/2024). From VCU Libraries.
- (61) Schreiber, M.; Regalbuto, J. R. A fundamental study of Pt tetraammine impregnation of silica: 1. The electrostatic nature of platinum adsorption. *Journal of Catalysis* **2004**, 255 (1), 190-202. DOI: <https://doi.org/10.1016/j.jcat.2004.03.034> (accessed 4/11/2024). From VCU Libraries.

- (62) Schreier, M. R. Toward a molecular understanding of catalyst preparation. Doctoral Dissertation, University of Illinois at Chicago, Chicago, Illinois, 2014.
https://indigo.uic.edu/articles/thesis/Toward_a_molecular_understanding_of_catalyst_preparation_/10.890275/1 (accessed 4/24/2024).
- (63) Hao, X.; Quach, L.; Korah, J.; Spieker, W. A.; Regalbuto, J. R. The control of platinum impregnation by PZC alteration of oxides and carbon. *Journal of Molecular Catalysis A: Chemical* **2004**, *219* (1), 97-107. DOI: <https://doi.org/10.1016/j.molcata.2004.04.026> (accessed 4/11/2024).
- (64) Schreier, M.; Teren, S.; Belcher, L.; Regalbuto, J. R.; Miller, J. T. The nature of 'overexchanged' copper and platinum on zeolites. *Nanotechnology* **2005**, *16* (7), 582-591. DOI: 10.1088/0957-4484/16/7/036 (accessed 4/11/2024). From VCU Libraries.
- (65) Jiao, L.; Regalbuto, J. R. The synthesis of highly dispersed noble and base metals on silica via strong electrostatic adsorption: I. Amorphous silica. *Journal of Catalysis* **2008**, *260* (2), 329-341. DOI: 10.1016/j.jcat.2008.09.022 (accessed 09/05/2022).
- (66) Schreier, M.; Feltes, T. E.; Schaal, M. T.; Regalbuto, J. R. The determination of oxide surface charging parameters for a predictive metal adsorption model. *Journal of Colloid and Interface Science* **2010**, *348* (2), 571-578. DOI: <https://doi.org/10.1016/j.jcis.2010.04.064> (accessed 4/11/2024). From VCU Libraries.
- (67) Zhu, X.; Cho, H.-r.; Pasupong, M.; Regalbuto, J. R. Charge-Enhanced Dry Impregnation: A Simple Way to Improve the Preparation of Supported Metal Catalysts. *ACS Catalysis* **2013**, *3* (4), 625-630. DOI: 10.1021/cs3008347 (accessed 9/13/2023). From VCU Libraries.
- (68) Binz, J. M. Quantitative thermodynamic understanding of the solid-liquid interface during heterogenous catalysis. Doctoral, The Pennsylvania State University, 2013.
<https://etda.libraries.psu.edu/catalog/19730> (accessed 4/25/2024).
- (69) Ewbank, J. L.; Kovarik, L.; Diallo, F. Z.; Sievers, C. Effect of metal-support interactions in Ni/Al₂O₃ catalysts with low metal loading for methane dry reforming. *Applied Catalysis A: General* **2015**, *494*, 57-67. DOI: <https://doi.org/10.1016/j.apcata.2015.01.029> (accessed 4/25/2024). From VCU Libraries.
- (70) Asokan, C.; Xu, M.; Dai, S.; Pan, X.; Christopher, P. Synthesis of Atomically Dispersed Rh Catalysts on Oxide Supports via Strong Electrostatic Adsorption and Characterization by Cryogenic Infrared Spectroscopy. *The Journal of Physical Chemistry C* **2022**, *126* (44), 18704-18715. DOI: <https://doi.org/10.1021/acs.jpcc.2c05426> (accessed 4/25/2024). From VCU Library.
- (71) Regalbuto, J. R.; Ansel, O.; Miller, J. T. An evaluation of Pt sulfite acid (PSA) as precursor for supported Pt catalysts. *Topics in Catalysis* **2006**, *39*, 237-243. DOI: <https://doi.org/10.1007/s11244-006-0062-1> (accessed 4/11/2024). From VCU Libraries.
- (72) D'Souza, L.; Regalbuto, J. R.; Miller, J. T. Preparation of carbon supported cobalt by electrostatic adsorption of [Co(NH₃)₆]Cl₃. *Journal of Catalysis* **2008**, *254* (2), 157-169. DOI: <https://doi.org/10.1016/j.jcat.2007.12.007> (accessed 4/11/2024). From VCU Libraries.
- (73) Jiao, L.; Regalbuto, J. R. The synthesis of highly dispersed noble and base metals on silica via strong electrostatic adsorption: II. Mesoporous silica SBA-15. *Journal of Catalysis* **2008**, *260* (2), 342-350. DOI: <https://doi.org/10.1016/j.jcat.2008.09.023> (accessed 4/11/2024). From VCU ILLiad.
- (74) Lambert, S.; Job, N.; D'Souza, L.; Pereira, M. F. R.; Pirard, R.; Heinrichs, B.; Figueiredo, J. L.; Pirard, J.-P.; Regalbuto, J. R. Synthesis of very highly dispersed platinum catalysts supported on carbon xerogels by the strong electrostatic adsorption method. *Journal of Catalysis* **2009**, *261* (1), 23-33. DOI: <https://doi.org/10.1016/j.jcat.2008.10.014> (accessed 4/11/2024). From VCU Libraries.
- (75) Job, N.; Lambert, S.; Chatenet, M.; Gommès, C. J.; Maillard, F.; Berthon-Fabry, S.; Regalbuto, J. R.; Pirard, J.-P. Preparation of highly loaded Pt/carbon xerogel catalysts for Proton Exchange Membrane fuel cells by the Strong Electrostatic Adsorption method. *Catalysis Today* **2010**, *150* (1-2), 119-127. DOI: <https://doi.org/10.1016/j.cattod.2009.06.022> (accessed 4/11/2024). From VCU Libraries.
- (76) Feltes, T. E.; AEspinosa-Alonso, L.; de Smit, E.; D'Souza, L.; Meyer, R. J.; Weckhuysen, B. M.; Regalbuto, J. R. Selective adsorption of manganese onto cobalt for optimized Mn/Co/TiO₂ Fischer-

Tropsch catalysts. *Journal of Catalysis* **2010**, 270 (1), 95-102. DOI: <https://doi.org/10.1016/j.jcat.2009.12.012> (accessed 4/11/2024). From VCU Libraries.

(77) Feltes, T. E.; Zhao, Y.; Klie, R. F.; Meyer, R. J.; Regalbuto, J. R. The Influence of Preparation Method on Mn–Co Interactions in Mn/Co/TiO₂ Fischer–Tropsch Catalysts. *ChemCatChem* **2010**, 2 (9), 1065-1068. DOI: <https://doi.org/10.1002/cctc.201000103> (accessed 4/11/2024).

(78) Zhao, Y.; Feltes, T. E.; Regalbuto, J. R.; Meyer, R. J.; Klie, R. F. In-Situ Electron Energy Loss Spectroscopy Study of Mn-Promoted Co/TiO₂ Fischer–Tropsch Catalysts. *Catalysis Letters* **2011**, 141, 641-648. DOI: <https://doi.org/10.1007/s10562-011-0559-5> (accessed 4/11/2024). From VCU Libraries.

(79) Liu, J.; Regalbuto, J. R. Molecular Characterization of Noble Metal Adsorption at the Water-Aluminum Oxide Interface. *Advanced Materials Research* **2012**, 369-398, 745-750. DOI: <https://doi.org/10.4028/www.scientific.net/AMR.396-398.745> (accessed 11 April, 2024). From VCU ILLiad.

(80) Qiuli, L.; Joshi, U. A.; Über, K.; Regalbuto, J. R. The control of Pt and Ru nanoparticle size on high surface area supports. *Physical Chemistry Chemical Physics* **2014**, 16 (48), 26431-26435. DOI: <https://doi.org/10.1039/C4CP02714K> (accessed 4/11/2024). From VCU Libraries.

(81) O'Connell, K.; Regalbuto, J. R. High Sensitivity Silicon Slit Detectors for 1 nm Powder XRD Size Detection Limit. *Catalysis Letters* **2015**, 145, 777-783. DOI: <https://doi.org/10.1007/s10562-015-1479-6> (accessed 4/11/2024). From VCU Libraries.

(82) Srivastava, R. R.; Kim, M.-s.; Lee, J.-c. Separation of Tungsten from Mo-Rich Leach Liquor by Adsorption onto a Typical Fe–Mn Cake: Kinetics, Equilibrium, Mechanism, and Thermodynamics Studies. *Industrial & Engineering Chemistry Research* **2013**, 52 (49), 17591-17597. DOI: <https://doi.org/10.1021/ie402434a> (accessed 4/27/2024). From VCU Library.

(83) He, J.; Hong, S.; Zhang, L.; Gan, F.; Ho, Y.-S. Equilibrium and thermodynamic parameters of adsorption of Methylene Blue onto rectorite. *Fresenius Environmental Bulletin* **2010**, 19 (11a), 2651-2656. (accessed 4/27/2024). From VCU Libraries.

(84) Gupta, V. K. Equilibrium Uptake, Sorption Dynamics, Process Development, and Column Operations for the Removal of Copper and Nickel from Aqueous Solution and Wastewater Using Activated Slag, a Low-Cost Adsorbent. *Industrial & Engineering Chemistry Research* **1998**, 37 (1), 192-202. DOI: <https://doi.org/10.1021/ie9703898> (accessed 4/27/2024). From VCU Libraries.

(85) Lv, L.; Tsoi, G.; Zhao, X. S. Uptake Equilibria and Mechanisms of Heavy Metal Ions on Microporous Titanosilicate ETS-10. *Industrial & Engineering Chemistry Research* **2004**, 43 (24), 7900-7906. DOI: <https://doi.org/10.1021/ie0498044> (accessed 4/27/2024). From VCU Library.

(86) Wagner, W.; Pruß, A. The IAPWS Formulation 1995 for the Thermodynamic Properties of Ordinary Water Substance for General and Scientific Use. *Journal of Physical and Chemical Reference Data* **2002**, 31, 387-535. DOI: <https://doi.org/10.1063/1.1461829> (accessed 4/26/2024).

(87) *Revised Release on the IAPWS Formulation 1995 for the Thermodynamic Properties of Ordinary Water Substance for General and Scientific Use*; International Association for the Properties of Water and Steam, Prague, Czech Republic, 2018. <http://www.iapws.org/relguide/IAPWS95-2018.pdf> (accessed 4/26).

(88) *Revised Release on the Ionization Constant of H₂O*; The International Association for the Properties of Water and Steam, Banff, Canada, 2019. <http://www.iapws.org/relguide/Ionization.pdf> (accessed 4/26/2024).

(89) Bandura, A. V.; Lvov, S. The Ionization Constant of Water over Wide Ranges of Temperature and Density. *Journal of Physical and Chemical Reference Data* **2006**, 35 (1), 15-30. DOI: <https://doi.org/10.1063/1.1928231> (accessed 4/26/2024). From Academia.com.

(90) Harris, F. E.; Alder, B. J. Dielectric Polarization in Polar Substances. *The Journal of Chemical Physics* **1953**, 21 (6), 1031-1038. DOI: <https://doi.org/10.1063/1.1699105> (accessed 4/27/2024). From VCU ILLiad.

- (91) Fernandez, D. P.; Goodwin, A. R. H.; Lemmon, E. W.; Sengers, J. M. H. L.; Williams, R. C. A Formulation for the Static Permittivity of Water and Steam at Temperatures from 238 K to 873 K at Pressures up to 1200 MPa, Including Derivatives and Debye–Hückel Coefficients. *Journal of Physical and Chemical Reference Data* **1997**, *26* (4), 1125-1166. DOI: <https://doi.org/10.1063/1.555997> (accessed 4/27/2024). From VCU Libraries.
- (92) *Release on the Static Dielectric Constant of Ordinary Water Substance for Temperatures from 238 K to 873 K and Pressures up to 1000 MPa*; The International Association for the Properties of Water and Steam, Erlangen, Germany, 1997. <http://www.iapws.org/relguide/dielec.pdf> (accessed 4/27/2024).
- (93) Russel, W. B.; Saville, D. A.; Schowalter, W. R. *Colloidal Dispersions*; Cambridge University Press, 1989. DOI: <https://doi.org/10.1017/CBO9780511608810>.
- (94) Wright, M. R. *An Introduction to Aqueous Electrolyte Solutions*; John Wiley & Sons Inc., 2007.
- (95) Duan, Z.; Li, D. Coupled phase and aqueous species equilibrium of the H₂O–CO₂–NaCl–CaCO₃ system from 0 to 250 °C, 1 to 1000 bar with NaCl concentrations up to saturation of halite. *Geochimica et Cosmochimica Acta* **2008**, *72* (20), 5128-5145. DOI: <https://doi.org/10.1016/j.gca.2008.07.025> (accessed 4/27/2024). From VCU Libraries.
- (96) *Saturated Vapor Pressure*. Dortmund Data Bank (DDB), <http://ddbonline.ddbst.com/AntoineCalculation/AntoineCalculationCGI.exe?component=Carbon+dioxide&tunit=%C2%B0C&punit=mmHg&TemperaturesEdit=&calculate=Calculate> (accessed 2020).
- (97) Milonjić, S. K. A consideration of the correct calculation of thermodynamic parameters of adsorption. *Journal of the Serbian Chemical Society* **2007**, *72* (12), 1363-1367. DOI: <https://doi.org/10.2298/JSC0712363M> (accessed 4/28/2024).
- (98) Zhou, X.; Yu, X.; Maimaitiniyazi, R.; Zhang, X.; Qu, Q. Discussion on the thermodynamic calculation and adsorption spontaneity re Ofudje et al. (2023). *Heliyon* **2024**, *10* (8), 1-7. DOI: <https://doi.org/10.1016/j.heliyon.2024.e28188> (accessed 2/28/2024).
- (99) Zhou, X.; Zhou, X. THE UNIT PROBLEM IN THE THERMODYNAMIC CALCULATION OF ADSORPTION USING THE LANGMUIR EQUATION. *Chemical Engineering Communications* **2014**, *201* (11), 1459-1467. DOI: <https://doi.org/10.1080/00986445.2013.818541> (accessed 4/28/2024). From VCU ILLiad.
- (100) Liu, Y. Is the Free Energy Change of Adsorption Correctly Calculated? *Journal of Chemical and Engineering Data* **2009**, *54* (7), 1981-1985. DOI: <https://doi.org/10.1021/jc800661q> (accessed 4/27/2024). From VCU Library.
- (101) Tewari, P. H.; Campbell, A. B. Temperature dependence of point of zero charge of cobalt and nickel oxides and hydroxides. *Journal of Colloid and Interface Science* **1976**, *55* (3), 531-539. DOI: [https://doi.org/10.1016/0021-9797\(76\)90063-1](https://doi.org/10.1016/0021-9797(76)90063-1) (accessed 4/27/2024). From VCU Libraries.
- (102) Tewari, P. H.; McLean, A. W. Temperature dependence of point of zero charge of alumina and magnetite. *Journal of Colloid and Interface Science* **1972**, *40* (2), 267-272. DOI: [https://doi.org/10.1016/0021-9797\(72\)90016-1](https://doi.org/10.1016/0021-9797(72)90016-1) (accessed 4/29/2024). From VCU Libraries.
- (103) Bérubé, Y. G.; de Bruyn, P. L. Adsorption at the rutile-solution interface: I. Thermodynamic and Experimental Study. *Journal of Colloid and Interface Science* **1968**, *27* (2), 305-318. DOI: [https://doi.org/10.1016/0021-9797\(68\)90038-6](https://doi.org/10.1016/0021-9797(68)90038-6) (accessed 4/28/2024). From VCU Library.
- (104) Neubrand, A.; Lindner, R.; Hoffman, P. Room-Temperature Solubility Behavior of Barium Titanate in Aqueous Media. *Journal of the American Ceramic Society* **2004**, *83* (4), 860-864. DOI: <https://doi.org/10.1111/j.1151-2916.2000.tb01286.x> (accessed 4/29/2024). From VCU ILLiad.
- (105) Hérard, C.; Faivre, A.; Lemaître, J. Surface decontamination treatments of undoped BaTiO₃—part I: Powder and green body properties. *Journal of the European Ceramic Society* **1995**, *15* (2), 135-143. DOI: [https://doi.org/10.1016/0955-2219\(95\)93059-C](https://doi.org/10.1016/0955-2219(95)93059-C) (accessed 4/29/2024). From VCU Libraries.
- (106) Zhou, H.; Zhang, H.; Yuan, S. Comparison of H₂O Adsorption and Dissociation Behaviors on Rutile (110) and Anatase (101) Surfaces Based on ReaxFF Molecular Dynamics Simulation. *Molecules* **2023**, *28* (19), 1-14. DOI: <https://doi.org/10.3390/molecules28196823> (accessed 4/28/2024).

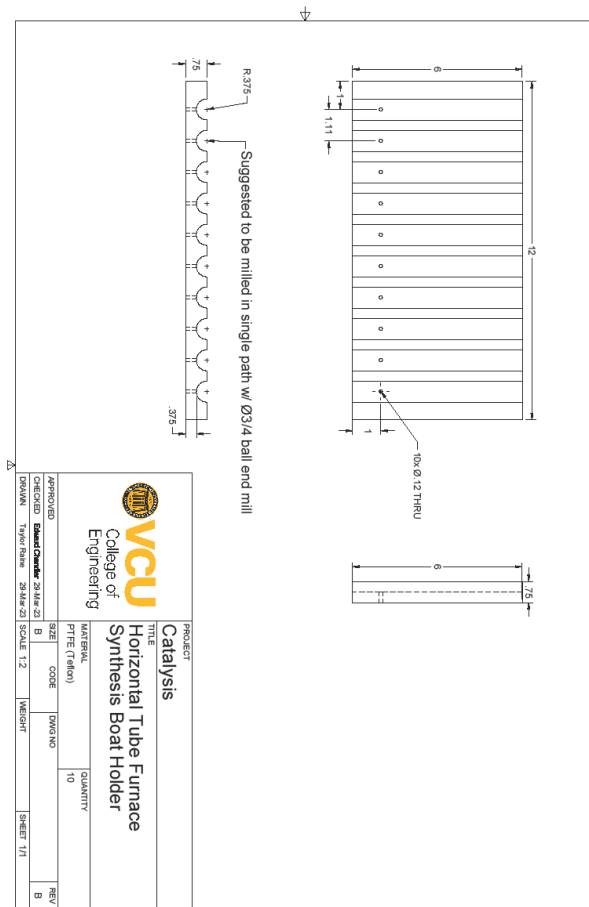
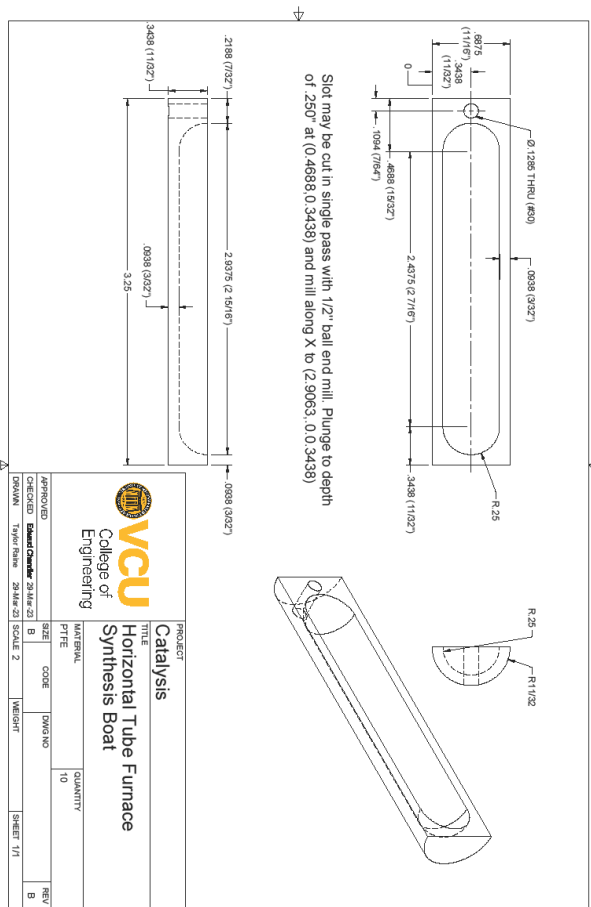
- (107) Korah, J.; Spieker, W. A.; Regalbuto, J. R. Why Ion-Doped, PZC-Altered Silica and Alumina Fail to Influence Platinum Adsorption. *Catalysis Letters* **2003**, *85* (1-2), 123-127. DOI: <https://doi.org/10.1023/A:1022189312386> (accessed 4/29/2024). From VCU Libraries.
- (108) Cho, H.-R.; Regalbuto, J. R. The rational synthesis of Pt-Pd bimetallic catalysts by electrostatic adsorption. *Catalysis Today* **2015**, *246*, 143-153. DOI: <https://doi.org/10.1016/j.cattod.2014.09.029> (accessed 4/30/2024). From VCU Libraries.
- (109) Regalbuto, J. R. Strong Electrostatic Adsorption of Metals onto Catalyst Supports. In *Catalyst Preparation*, Regalbuto, J. R. Ed.; CRC Press, 2006; pp 297-318.
- (110) Eschmann, T. O.; Lamme, W. S.; Manchester, R. L.; Parmentier, T. E.; Cognigni, A.; Rønning, M.; de Jong, K. P. Effect of support surface treatment on the synthesis, structure, and performance of Co/CNT Fischer–Tropsch catalysts. *Journal of Catalysis* **2015**, *328*, 130-138. DOI: <https://doi.org/10.1016/j.jcat.2014.12.010> (accessed 5/2/2024). From VCU Libraries.
- (111) Zhong, C. J.; Regalbuto, J. R. Metal Nanoparticle Synthesis. In *Comprehensive Inorganic Chemistry II*, Reedijk, J., Poeppelemeier, K. Eds.; Vol. 7; Elsevier, Ltd., 2013; pp 75-102.
- (112) Contescu, A.; Contescu, C.; Schwarz, J. A. Methods for Preparation of Catalytic Materials. *Chemical Reviews* **1995**, *95* (3), 477-510. DOI: <https://doi.org/10.1021/cr00035a002> (accessed 5/2/2024). From VCU Libraries.
- (113) Eskandari, S.; Li, Y.; Tao, F. F.; Regalbuto, J. R. The Use of Salts to Control Silica Supported Pt Particle Size in Charge Enhanced Dry Impregnation Syntheses. *Catalysis Today* **2019**, *334*, 187-192. DOI: <https://doi.org/10.1016/j.cattod.2018.11.033> (accessed 5/2/2023). From VCU Libraries.
- (114) Samad, J. E. Rational Design and Synthesis of Pt/SilicaAlumina Metal-Acid Bifunctional Catalysts. Doctoral, University of South Carolina, Columbia, 2016. <https://scholarcommons.sc.edu/etd/3562/> (accessed 5/2/2024).
- (115) Nieto, M. A. Effect of Pretreatment on Metal Dispersion in Carbon and Oxide Supported Catalysts. University of Illinois at Chicago, Chicago, 2012. https://indigo.uic.edu/articles/thesis/Effect_of_Pretreatment_on_Metal_Dispersion_in_Carbon_and_Oxide_Supported_Catalysts/10827044 (accessed 5/2/2024).
- (116) Marcus, Y. Effect of Ions on the Structure of Water: Structure Making and Breaking. *Chemical Reviews* **2009**, *109* (3), 1346-1370. DOI: <https://doi.org/10.1021/cr8003828> (accessed 5/2/2024). From VCU Libraries.
- (117) Shakouri, A. Insights Into Rational Catalysts Synthesis. Doctoral Dissertation, University of South Carolina, Columbia, 2021. <https://scholarcommons.sc.edu/etd/6826/> (accessed 09/10/2022).
- (118) Regalbuto, J. R.; Chandler, E.; Ezeorah, C.; Ojo, A.; Thornburg, N.; Romero, M.; Pham, H.; Datye, A.; Jeon, T.-Y.; Gupton, B. F.; Williams, C. T. From deposited metal precursors to supported atoms or nanoparticles. *Catalysis Today* **2024**, *431*, 1-9. DOI: <https://doi.org/10.1016/j.cattod.2024.114556> (accessed 4/30/2024). From VCU Libraries.
- (119) Sun, X.; Dawson, S. R.; Parmentier, T. E.; Malta, G.; Davies, T. E.; He, Q.; Lu, L.; Morgan, D. J.; Carthey, N.; Johnston, P.; et al. Facile synthesis of precious-metal single-site catalysts using organic solvents. *Nature Chemistry* **2020**, *12*, 560-567. DOI: 10.1038/d.2020.0098831512 (accessed 10/17/2023). From University of South Carolina Libraries.
- (120) Xu, Z.; Li, M.; Shen, G.; Chen, Y.; Lu, D.; Ren, P.; Jiang, H.; Wang, X.; Dai, B. Solvent Effects in the Preparation of Catalysts Using Activated Carbon as a Carrier. *Nanomaterials* **2023**, *13* (3), 1-10. DOI: 10.3390/nano13030393 (accessed 9/4/2023). From VCU Libraries.
- (121) Khodabakhshi, S.; Fulvio, P. F.; Andreoli, E. Carbon black reborn: Structure and chemistry for renewable energy harnessing. *Carbon* **2020**, *162*, 604-649. DOI: <https://doi.org/10.1016/j.carbon.2020.02.058> (accessed 5/1/2024). From VCU Libraries.

- (122) Burgom, T. A. L.; Ducati, T. R. D.; Francisco, K. R.; Clinckspoor, K. J.; Galembeck, F.; Galembeck, S. E. Triboelectricity: Macroscopic Charge Patterns Formed by Self-Arraying Ions on Polymer Surfaces. *Langmuir* **2012**, *28* (19), 7407-7416. DOI: 10.1021/la301228j (accessed 8/29/2023). From VCU Libraries.
- (123) Ryser, P. *Electrostatics and Weighing: Dealing with Static Samples* 30475700A; Mettler Toledo, 2018. https://www.mt.com/dam/non-indexed/po/labtec/13_White_Papers/WP_Electrostatics_Weighing_EN.pdf (accessed 8/29/2023).
- (124) Zerostat Use Instructions. SPI Supplies: 206 Garfield Avenue
West Chester, PA 19380, USA, p 1.
- (125) Kumbhani, S. R.; Wingen, L. M.; Perraud, V.; Finlayson-Pitts, B. J. A cautionary note on the effects of laboratory air contaminants on ambient ionization mass spectrometry measurements. *Rapic Communications in Mass Spectrometry* **2017**, *31* (19), 1659-1668. DOI: 10.1002/rcm.7951 (accessed 8/29/2023). From VCU Libraries.
- (126) Koschmieder, E. L. *Bénard Cells and Taylor Vortices*; Cambridge University Press, 1993.
- (127) Faure, A.; Grimsey, I. M.; Rowe, R. C.; York, P.; Cliff, M. J. Applicability of a scale-up methodology for wet granulation processes in Collette Gral High Shear Mixer-granulators. *European Journal of Pharmaceutical Sciences* **1999**, *8* (2), 85-93. DOI: [https://doi.org/10.1016/S0928-0987\(98\)00063-3](https://doi.org/10.1016/S0928-0987(98)00063-3) (accessed 5/1/2024). From VCU Library.
- (128) Landin, M.; York, P.; Cliff, M. J.; Rowe, R. C.; Wigmore, A. J. The effect of batch size on scale-up of a pharmaceutical granulation in a fixed bowl mixer granulator. *International Journal of Pharmaceutics* **1996**, *134* (1-2), 243-246. DOI: [https://doi.org/10.1016/0378-5173\(96\)04461-4](https://doi.org/10.1016/0378-5173(96)04461-4) (accessed 5/1/2024). From VCU Library.
- (129) Xu, R.; Wi, C.; Xy, H. Particle size and zeta potential of carbon black in liquid media. *Carbon* **2007**, *45* (14), 2806-2809. DOI: <https://doi.org/10.1016/j.carbon.2007.09.010> (accessed 5/1/2024). From VCU Library.
- (130) Liu, Q.; Tengco, J. M.; Banerjee, R.; Keels, J.; Regalbuto, J. R. Accurate Subtraction and Deconvolution of Pt Nanoparticles from Crystalline Supports Using Powder XRD with a High Sensitivity Detector. University of South Carolina: p 16.
- (131) Katritzky, A. R.; Fara, D. C.; Kuanar, M.; Hur, E.; Karelson, M. The Classification of Solvents by Combining Classical QSPR Methodology with Principal Component Analysis. *Journal of Physical Chemistry: A* **2005**, *109* (45), 10323-10341. DOI: 10.1021/jp050395e (accessed 11/16/2022). From VCU Libraries.

Appendix A: PTFE Boats and Holder Designs for Switched Solvent

Synthesis (SwiSS)

These plans were designed by Taylor Raine, graduate student in chemical and life science engineering at VCU, under Dr. Frank Gupton.



Appendix B: Decision Tree for One-Way Analysis of particle size from STEM Samples.

There is a wide variety of statistical test, many of which have explicit assumptions about the data, such as normality and equal variance across multiple samples. This means that different analyses work for different samples. The following shows the decision tree being used in the analysis of STEM samples of Switched Solvent Synthesis.

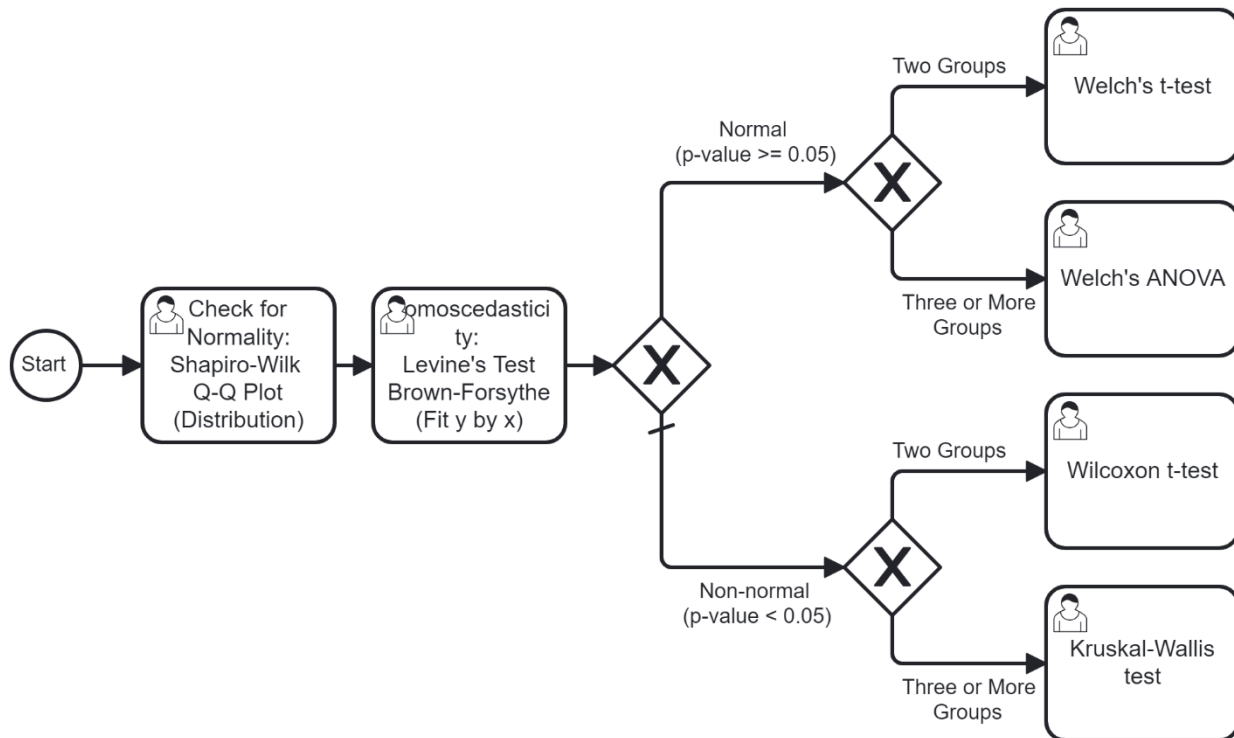


Figure 50. Decision tree showing comparison of datasets. In this work, those datasets are particle size distributions, collected by STEM in Chapter Four:.

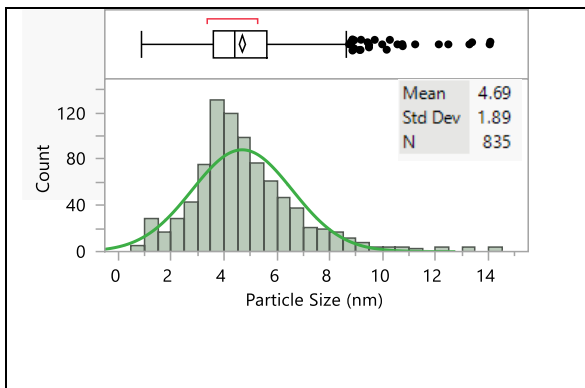
Appendix C: Statistical Analysis of STEM Particle Size Distributions for Switched Solvent Synthesis

Show Distributions for each sample

Table 14 shows the empirical distributions with an overlain best-fitted normal distribution for each of the samples measured, along with their summary statistics and values at each quantile. In addition, it shows the distribution of particles overlaid for each individual image. The Shapiro-Wilk Normality Test and the Anderson-Darling Test using critical values for normal distributions are used to assess normality and are reported in Table 16. All plots and test statistics are generated using JMP Pro 18.1.

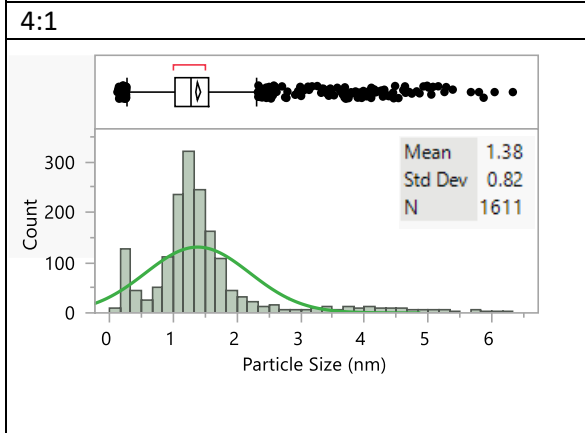
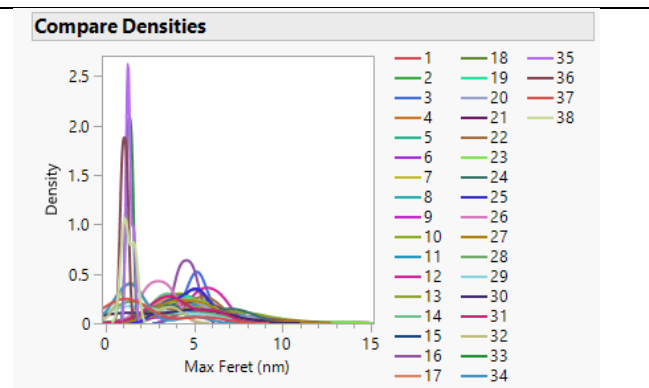
Table 14. STEM analysis for SwiSS. Particle Size Distributions, Summary Statistics, Quantiles, and particle size densities for each image sampled.

CEDI



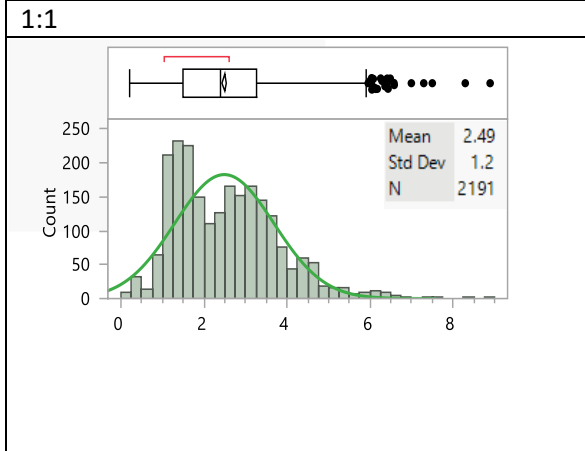
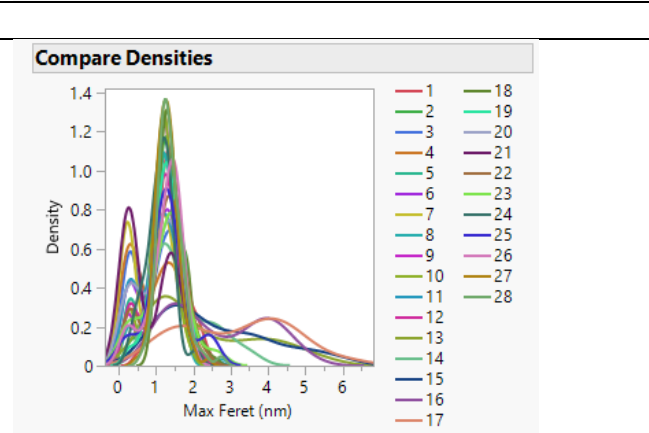
Quantiles

100.0%	maximum	14.1
99.5%		13.1
97.5%		8.95
90.0%		6.99
75.0%	quartile	5.61
50.0%	median	4.41
25.0%	quartile	3.58
10.0%		2.56
2.5%		1.27
0.5%		0.97
0.0%	minimum	0.85



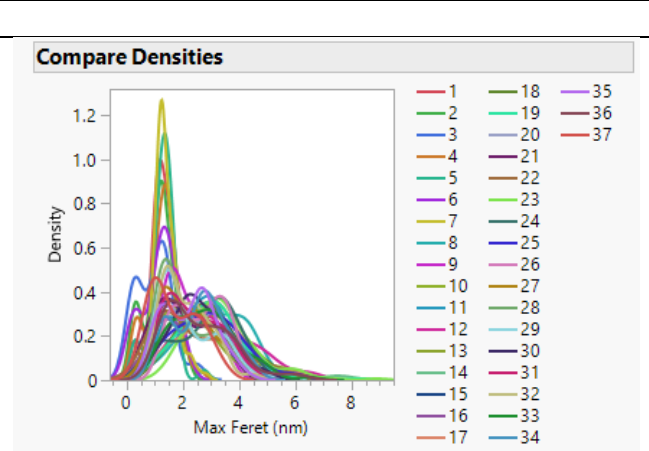
Quantiles

100.0%	maximum	6.33
99.5%		5.25
97.5%		4.1
90.0%		2.02
75.0%	quartile	1.55
50.0%	median	1.29
25.0%	quartile	1.04
10.0%		0.43
2.5%		0.23
0.5%		0.17
0.0%	minimum	0.13

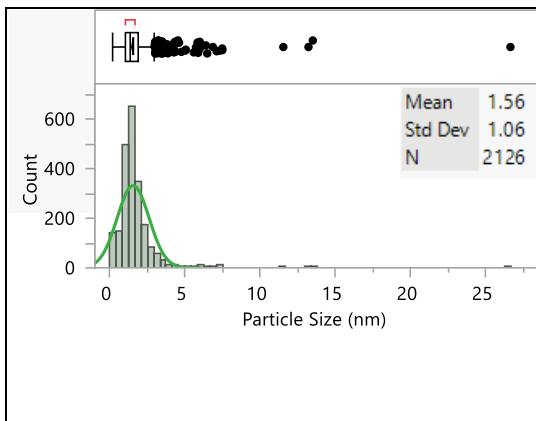


Quantiles

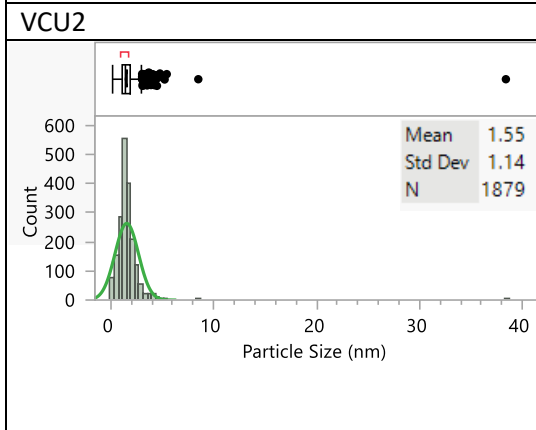
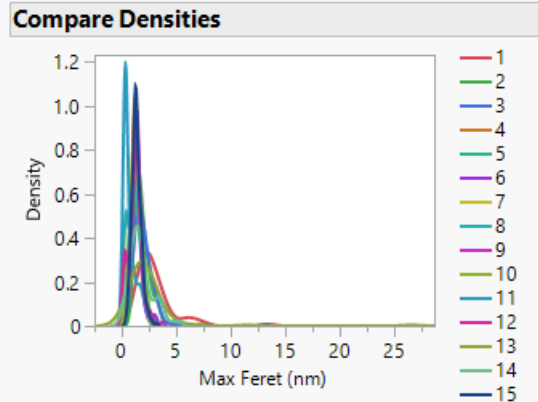
100.0%	maximum	8.9
99.5%		6.41
97.5%		5.15
90.0%		4.03
75.0%	quartile	3.28
50.0%	median	2.39
25.0%	quartile	1.5
10.0%		1.16
2.5%		0.83
0.5%		0.27
0.0%	minimum	0.21



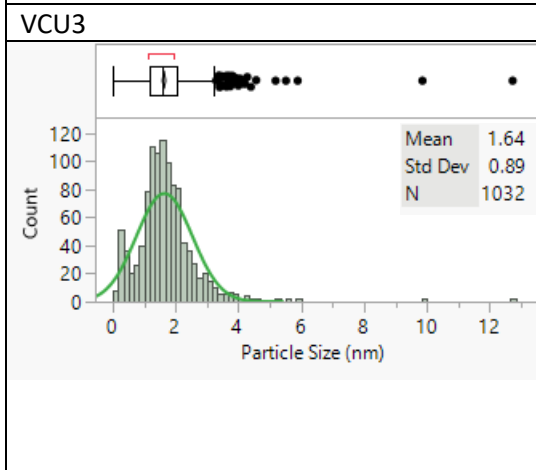
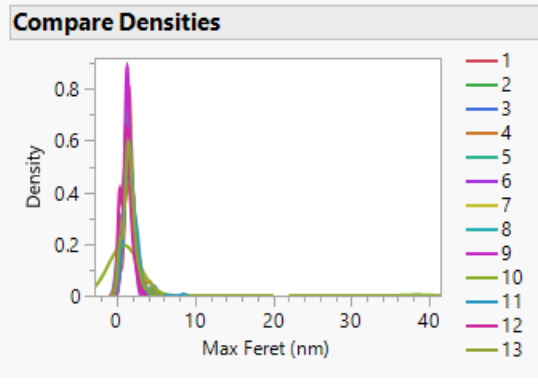
VCU1



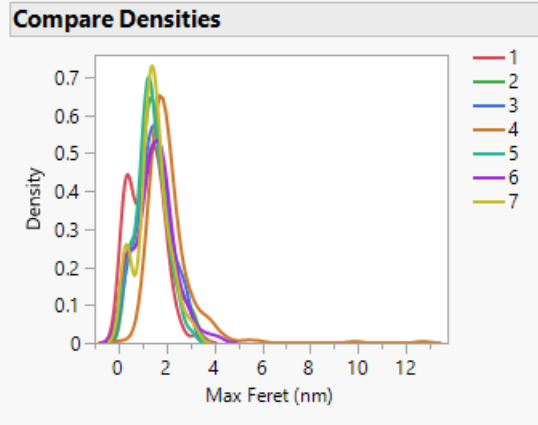
Quantiles		
100.0%	maximum	26.6
99.5%		6.42
97.5%		3.44
90.0%		2.46
75.0%	quartile	1.85
50.0%	median	1.42
25.0%	quartile	1.1
10.0%		0.68
2.5%		0.29
0.5%		0.23
0.0%	minimum	0.19



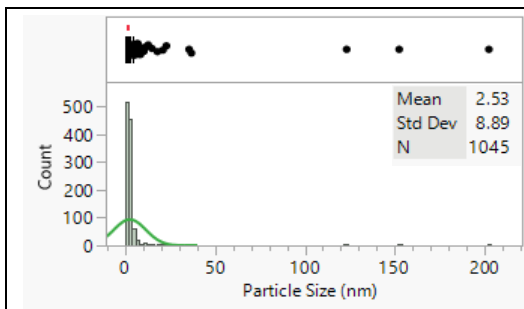
Quantiles		
100.0%	maximum	38.4
99.5%		4.46
97.5%		3.35
90.0%		2.46
75.0%	quartile	1.88
50.0%	median	1.44
25.0%	quartile	1.11
10.0%		0.59
2.5%		0.31
0.5%		0.22
0.0%	minimum	0.15



Quantiles		
100.0%	maximum	12.7
99.5%		5.08
97.5%		3.54
90.0%		2.56
75.0%	quartile	2.02
50.0%	median	1.58
25.0%	quartile	1.17
10.0%		0.62
2.5%		0.27
0.5%		0.04
0.0%	minimum	0



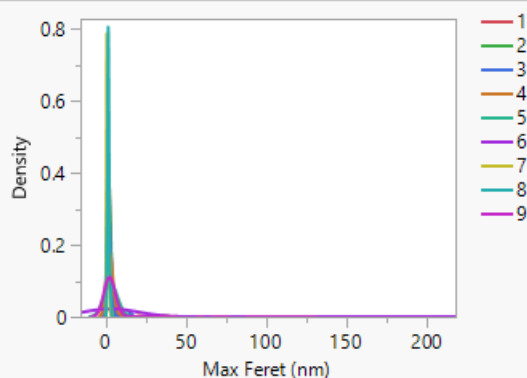
VCU4



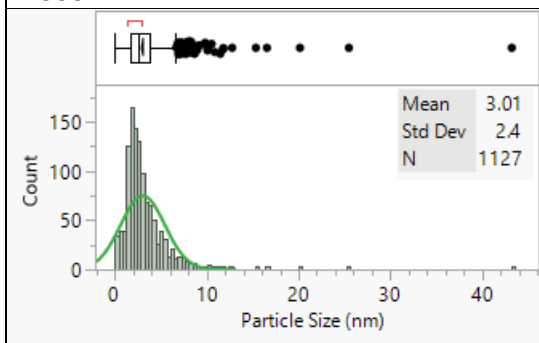
Quantiles

100.0%	maximum	202
99.5%		32.6
97.5%		5.89
90.0%		3.4
75.0%	quartile	2.41
50.0%	median	1.68
25.0%	quartile	1.19
10.0%		0.9
2.5%		0.31
0.5%		0.2
0.0%	minimum	0

Compare Densities



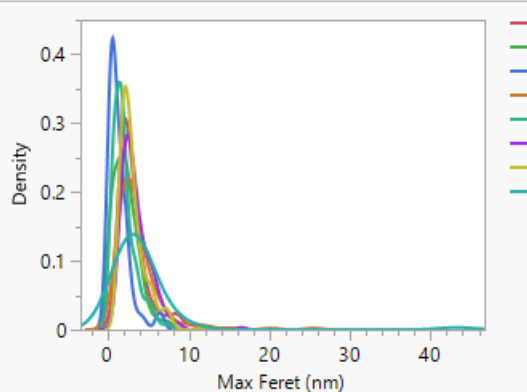
VCU5



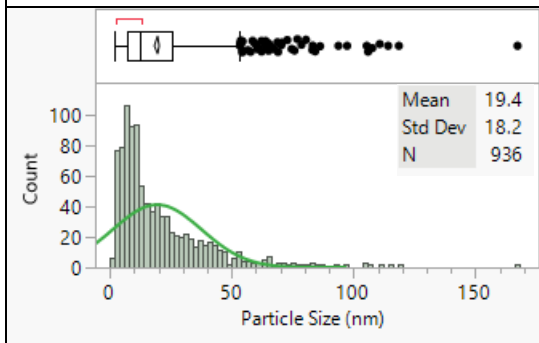
Quantiles

100.0%	maximum	43.2
99.5%		13.7
97.5%		8.03
90.0%		5.4
75.0%	quartile	3.68
50.0%	median	2.47
25.0%	quartile	1.75
10.0%		1.22
2.5%		0.35
0.5%		0.16
0.0%	minimum	0

Compare Densities



VCU6



Quantiles

100.0%	maximum	167
99.5%		109
97.5%		68.2
90.0%		41.9
75.0%	quartile	25.7
50.0%	median	12.6
25.0%	quartile	7.39
10.0%		4.35
2.5%		2.69
0.5%		1.7
0.0%	minimum	1.7

Compare Densities

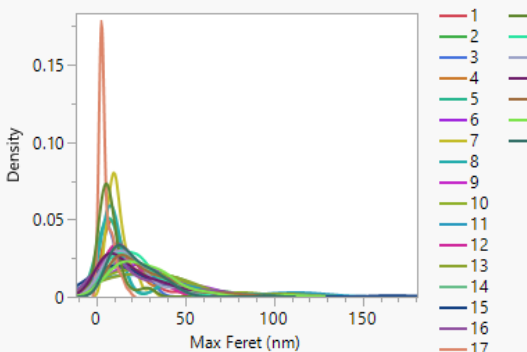


Table 15. Summary Statistics

Sample	Median	Mean	Std Dev	N
CEDI	4.41	4.69	1.89	835
4:1	1.29	1.38	0.82	1611
1:1	2.39	2.49	1.20	2191
VCU1	1.42	1.56	1.06	2126
VCU2	1.14	1.55	1.14	1879
VCU3	1.58	1.64	0.89	1032
VCU4	1.68	2.53	8.89	1045
VCU5	2.47	3.01	2.40	1127
VCU6	12.60	19.40	18.20	936

Normality Check (Shapiro-wilk or Anderson-Dearing)

Here, the normality of each sample is tested using two tests: The Shapiro-Wilk test, which tests normality specifically, and the Anderson-Dearing test, which is a more general test that can check multiple distributions, given that you have the critical values. The null hypothesis of each is that the distribution is normal.

Table 16. Normality tests. The Null hypothesis is that the particle size distributions reflect a normal distribution.

Sample	Shapiro-Wilk Test	Anderson-Darling Test
CEDI	<0.0001	<0.0001
4:1	<0.0001	<0.0001
1:1	--	<0.0001
VCU1	--	<0.0001
VCU2	<0.0001	<0.0001
VCU3	<0.0001	<0.0001
VCU4	<0.0001	<0.0001
VCU5	<0.0001	<0.0001
VCU6	<0.0001	<0.0001

As can be seen by the p-values for each test of each sample, we can reject that any of the tested samples contain a normally distributed particle size distributions.

Homoscedasticity Check (Levine and Brown-Forsyth)

Kruskal-Wallis Test

Since both the Shapiro-Wilk and Anderson-Darling tests above show that the samples have non-normal distributions, we perform a non-parametric multiple comparisons using the Wilcoxon Signed Rank test on each pair of samples. The null hypothesis for such a test is that the means of each pair are equal.

As there are 9 samples, meaning $\frac{9!}{2!(9-2)!} = 36$ pairwise combinations, for simplicity we report that only 1 pair, VCU1 and VCU2 fails to reject the Null at a p-value of 0.3581. A condensed version of the results is the Connecting Letters report, where each sample is assigned one or more letters. Any two samples sharing the same letter have statistically similar means.

Figure 51. Connecting Letters report for all samples studied with STEM

Connecting Letters Report	
Level	
1:1	A
4:1	B
CED1	C
VCU1	D
VCU2	D
VCU3	E
VCU4	F
VCU5	G
VCU6	H

Levels not connected by same letter are significantly different.

Again, as stated above, only VCU1 and VCU2 have similar means.